People's Democratic Republic of Algeria

Ministry of Higher Education and Scientific Research

University of BATNA 2 – Mostefa Ben Boulaïd

Faculty of Technology

Departement of Electrical Engineering

THESIS

Laboratory: LSP–IE, BATNA 2000

A thesis submitted for the fulfillment of the degree of:

DOCTORATE OF SCIENCE IN ELECTRICAL ENGINEERING

Field: Electrical Control

Under the Theme:

A Contribution to Energy Saving in Electrical Control Systems

by:

AMIEUR OUALID

Examining Committee :

M. BENAGGOUNE Said	Prof.	University of Batna 2	President
M. ZIDANI Fatiha	Prof.	University of Batna 2	Supervisor
M. CHAIBA Azzedine.	Prof.	University of Khenchela	Examiner
M. BEDDIAF Yassine	MCA	University of Khenchela	Examiner
M. GOLEA Amar	Prof.	University of Biskra	Examiner
M. NAIT SAID Nasreddine	Prof.	University of Batna 2	Examiner

Acknowledgements

Acknowledgements

My first and ultimate gratitude goes to the Almighty ALLAH for blessing me with faith, health, and strength.

I would like to express my sincere appreciation to my advisor, Prof. ZIDANI Fatiha, for her guidance, intellectual support, and encouragement throughout my graduate studies and research. It is an honor and privilege to work with her and learn from her expertise.

I would also like to thank my Ph.D. committee members, Prof. BENAGGOUNE Said, Prof. GOLEA Amar, Prof. NAIT SAID Nasreddine, Prof. CHAIBA Azzedine, and Dr. BEDDIAF Yassine for their contributions to my success.

My deepest gratitude also goes to my parents, my siblings, my brothers, my sisters, and my uncles for the support, motivation, and encouragement I have received since day one.

I would like to thank my wife for being supportive and patient with me when I am frustrated and for coping with my busy work schedule. I ask ALLAH to bless and protect my two young twins, Anas and Farah.

I will not forget to express my appreciation to all the teachers in the Electrical Engineering Department at BATNA2 University.

My appreciation goes also to all those who helped me in one way or another to realize this work.

Table of Contents

Contents

Acknowledgements i

Table of Contents iii

List of Figures and Tables vi

List of Abbreviations x

Introduction 1

1 The State of the Art 6
- 1.1 Introduction . . . 7
- 1.2 Future Prospects of Microgrids in Algeria . . . 7
- 1.3 Renewable Energy Sources . . . 10
  - 1.3.1 Solar Photovoltaic System . . . 10
  - 1.3.2 Wind Turbine Generator . . . 12
  - 1.3.3 Integration of Renewable Energy Sources . . . 13
- 1.4 Interfacing Renewable Energy Sources with Microgrid . . . 15
  - 1.4.1 DC Microgrid . . . 16
  - 1.4.2 AC Microgrid . . . 16
  - 1.4.3 Hybrid Microgrid . . . 17
- 1.5 Energy Management in Microgrid . . . 19
  - 1.5.1 System Under Study . . . 20
- 1.6 Overview on Control of Microgrid . . . 22
  - 1.6.1 State Feedback Control . . . 23
  - 1.6.2 Standard H_∞ Control . . . 23
  - 1.6.3 Sliding Mode Control (SMC) . . . 23
  - 1.6.4 Fractional PID Control . . . 24
  - 1.6.5 Fuzzy Logic Control . . . 24
- 1.7 Conclusion . . . 25

2 Modeling of the Hybrid Renewable Energy System 26
- 2.1 Introduction . . . 27
- 2.2 Modeling of the Distributed Renewable Energy Generation System . . . 27
- 2.3 Model of Photovoltaic System . . . 29
  - 2.3.1 Modeling of Photovoltaic Array . . . 30

2.3.2 DC/DC Boost converter stage . . . 34
2.3.3 Searching MPPT algorithm . . . 37
2.4 Modeling of the DG-Connected Inverter . . . 39
2.4.1 Space Vector PWM Technique . . . 39
2.4.2 Active Power Filter System Modeling . . . 43
2.5 Conclusion . . . 46

3 Power Quality Improvement in Microgrid Based on Robust Voltage Controller 47
3.1 Introduction . . . 48
3.2 Power Quality Problem . . . 48
3.3 Control of Three-Phase Inverter System . . . 51
3.3.1 Design of Sliding Mode Current Controller . . . 51
3.3.2 Design of RSP Voltage Controller . . . 52
3.3.3 Control System using Structured Singular Value . . . 54
3.4 Proposed Robust Performance Control Technique . . . 56
3.4.1 Fractional PID Control Design . . . 56
3.4.2 Weighted-Mixed Sensitivity Problem Including FIWs . . . 57
3.4.3 Weighted-Mixed Sensitivity Problem Including AFWs . . . 60
3.5 Control Development and Simulation Results Discussions . . . 62
3.5.1 Frequency-domain analysis . . . 65
3.5.2 Time-domain analysis . . . 67
3.6 Conclusion . . . 71

4 Power Management in Microgrid Based on Fractional Fuzzy Controller 72
4.1 Introduction . . . 73
4.1.1 Power Management Problem . . . 73
4.2 Description and Modeling of the System . . . 76
4.2.1 Model of photovoltaic system . . . 78
4.2.2 Model of wind generator . . . 78
4.2.3 Model of battery energy storage system . . . 78
4.3 Design of the Fuzzy Logic Controller System . . . 79
4.4 Social Spider Optimization Algorithm . . . 82
4.5 Objective Function of Control . . . 85
4.6 Simulation Results and Discussion . . . 86
4.7 Conclusion . . . 93

Conclusions and Further Work 94

A Basic Concepts of Fractional Order Calculus 98
A.1 Fractional Order Calculus . . . 98
A.2 Numerical discrete approximation of fractional operators . . . 99

B Datasheet BP MSX120 101

Summary 116

List of Figures and Tables

List of Figures

1.1 Electricity Generation by Source (TWh), Algeria 1990–2018 . . . 8
1.2 Electricity Generation (GWh), Algeria 2018 . . . 9
1.3 Energy management system. . . . 15
1.4 DC microgrid. . . . 16
1.5 AC microgrid. . . . 17
1.6 Hybrid microgrid. . . . 18
1.7 Proposed hybrid microgrid control topology. . . . 20

2.1 Structure of dual stage PV system . . . 28
2.2 Schematic of PV system with boost converter . . . 29
2.3 One diode model of the solar cell . . . 30
2.4 V-I and V-P curves of PV panel. . . . 33
2.5 V-I and V-P curves of PV array. . . . 34
2.6 Block diagram of PV system with MPPT algorithm . . . 35
2.7 Flow chart of P&O MPPT algorithm . . . 38
2.8 Power converter system. . . . 39
2.9 Three-phase voltage source PWM inverter. . . . 40
2.10 Three-phase voltage source PWM inverter. . . . 42

3.1 Block diagram of inverter controller . . . 51
3.2 Block diagram of RSP controller . . . 52
3.3 Uncertain closed-loop model. . . . 54
3.4 Structure of the proposed FOPID voltage controller . . . 57
3.5 Tracking dynamic of the voltage given by the robustified fractional controller. . . . 66
3.6 Tracking dynamic of the voltage given by the robustified fractional controller. . . . 67
3.7 The output current given by the robustified fractional controller. . . . 68
3.8 Comparison of RMS and THD values of the load voltages. . . . 68
3.9 Comparison results for real load powers. . . . 69
3.10 Transient response of voltage and current under load change from 500% (t=0s) 100% (t=0.1s) to 0% (t=0.2). . . . 69
3.11 RMS and THD values of the load voltages under load change from 500% (t=0s) 100% (t=0.1s) to 0% (t=0.2). . . . 70

4.1 Hybrid PV/WIND/BATTERY power system. . . . 76
4.2 Block diagram of FOFPD+I controller . . . 80
4.3 Structure of the fuzzy inference system. . . . 81

4.4 FOFPD fuzzy controller with two inputs: (a) membership functions for error input; (b) membership functions for integral error input; (c) membership functions for output; (d) control surface. 82
4.5 Proposed SSO parameters calibration process 85
4.6 Hourly power generation capacities. 87
4.7 Step response plot of HRES applying the calibrated parameters 88
4.8 HRES power generation 89
4.9 PV power generation 90
4.10 WIND power generation 90
4.11 BATTERY power generation 91
4.12 HRES power generation with disturbance 92

List of Tables

2.1 BP MSX120 datasheet at STC. 31
2.2 Characteristics of 12 kW PV array. 32
2.3 PV module/array parameters values at STC 33
2.4 PWM Output voltage 41

3.1 Parameters of DC/AC inverter. 62

4.1 Hybrid Power System Parameters. 79
4.2 Rule base of E,DE inputs and the FLC controller outputs. 81
4.3 Calibrated parameters of FOFPD control. 88

List of Abbreviations

List of Abbreviations

AC Alternating Current

AFW Adjustable Fractional Weight

APF Active Power Filter

$BESS$ Battery Energy Storage System

CCM Continuous Conduction Mode

CSP Concentrated Solar Power

DC Direct Current

DCM Discontinuous Conduction Mode

DER Distributed Energy Resource

DG Distributed Generator

$DSMC$ Discrete Sliding Mode Control

EMS Energy Management System

FC Fuel Cell

FIW Fixed Integr Weight

FLC Fuzzy Logic Control

FO Fractional Order

$FOFPD+I$ Fractional Order Fuzzy $PD^{\alpha}+I$

$FOFPID$ Fractional Order Fuzzy PID

$FOPID$ Fractional Order Proportional-Integral-Derivative

GA Genetic Algorithm

GW Gigawatt

GWh Gigawatt-hour

$HAWT$ Horizontal Axis Wind Turbine

$HRES$ Hybrid Renewable Energy Source

IEA International Energy Agency

$IEEE$ Institute of Electrical and Electronics Engineers

$IGBT$ Insulated Gate Bipolar Transistor

$ITAE$ Integral Time Absolute Error

LMI Linear Matricial Inequality

MG Microgrid

$MIMO$ Multiple-Input Multiple-Output (MIMO)

$MOSFET$ Metal Oxide Semiconductor Field Effect Transistor

$MPPT$ Maximum Power Point Tracker

MT Micro-Turbine

NP Nominal Performance

$NSPWM$ Naturally Sampled Sine PWM

$PD^{\alpha} + I$ Proportional, Fractional Derivative and Integral

PFC Power Flow Controller

PMC Power Management Control

PSO Particle Swarm Optimization

PV Solar Photovoltaic

PWM Pulse Width Modulation

RMS Root Mean Square

RP Robust Performance

RS Robust Stability

RSP Robust Servomechanism Problem

SMC Sliding Mode Control

SSO Social Spider Optimisation

STC Standard Test Conditions

$SVPWM$ Space Vector PWM

THD Total Harmonic Distortion

TWh Terawatt-hour

UPS Uninterruptible Power Supplies

$USPWM$ Uniformly Sampled Sine PWM

$VAWT$ Vertical Axis Wind Turbine

WTG Wind Turbine Generator

P&O Perturb and Observe

Introduction

Introduction

During the 1960s through the early 1970s, the cost of electrical power was kept nearly constant around the world. The energy matrix was based on thermoelectric power plants that used coal or fuel as primary sources. With the rising oil prices in the early 1970s, the cost of energy increased at an average rate of 11–12% [1]. Later, in recent decades, low oil prices and the lack of large oil finds meant that the present reserves of Algeria for oil and natural gas could only cover consumption at this rate for the next 50 and 70 years in the case of oil and natural gas respectively [2].

The previous warning signs have forced the Algerian government to choose between pursuing a strong renewable energy agenda or consuming its oil and gas export profits. Amid dramatic upheavals in global energy, Algeria declared the transfer of its energy model to renewable energy for the first time in over two decades and announced a comprehensive energy transition strategy as part of its 2020 Five-Year Development Plan. The energy transition plan consists of three structural elements: a new government ministry, regulatory reform, and the formation of a new "Algerian Renewable Energy Company". Among the actions taken as part of the energy transition roadmap by the new Ministry of Energy Transition and Renewable Energies [3]:

- Development of self-consumption of renewable energy in individual solar panels with standalone or grid-connected systems.
- Individual or centralized solar farms will be used to electrify remote areas with standalone systems.

Microgrid energy systems are evolving as localized frameworks that combine various generating and storage components to allow electricity users to adjust their installed assets to meet local needs. This category includes Hybrid Renewable Energy power generation Sources ($HRES$) like

Solar Photovoltaic (PV) systems and Wind Turbine Generators (WTG), as well as future low or zero emission power generation technologies such as Micro-turbines (MT) and Fuel Cells (FCs) . These energy sources can be used in conjunction with Battery Energy Storage Systems ($BESS$) to overcome the intermittent nature of $HRES$ sources and increase system dependability and long-term energy sustainability. Such systems can be used as standalone microgrids to electrify remote locations that aren't linked to the grid or in island mode. Then, determining the correct unit size of available $HRES$ supplies is necessary to ensure enough generating capacity. Whereas, if this condition is not met, the islanded microgrid will suffer from some outages.

To overcome this limitation, a more focused attention on energy efficiency has arisen, with extensive studies conducted for this aim. Furthermore, to achieve optimal energy efficiency, microgrid systems require an appropriate Energy Management System (EMS) .

The proposal is focused on several control technologies of the actual EMS system configuration. Indeed, the need to adopt an EMS control strategy is based on several steps and tools, such as;

- The operating power system's architecture;
- The control architecture is based on the proper control technique selection, which makes the system robust and efficient;
- Using optimization tools to create a complete design and sizing of an electrical system;
- The integration of hybrid power generation systems is an intriguing asset for better EMS control, especially renewable energy sources.

It therefore seems essential to adopt an adequate control strategy that allows effective EMS. In the same context, we further extend the EMS in scheduling a microgrid's operation by developing advanced control tools for both achieving the power quality issues in the microgrid inverters by effectively mitigating the Total Harmonic Distortion (THD) values and optimal power management issues to ensure demand-response operation in the overall microgrid system. The thesis' core purposes are the previous two key EMS goals, and four chapters are discussed in the thesis outline to examine their impact on energy savings. The rest of this PhD thesis is organized as follows;

Chapter 1: This introduction chapter will take a descriptive approach to the investigation, presenting a current state-of-the-art description of the research topic. The resource evaluation for two chosen renewable energy sources (solar and wind) as primary microgrid supply components is presented in section one. In addition, an examination of the many elements and problems of integrating these resources into the microgrid is presented. Through evaluations of the existing literature, section two focuses on the various configurations integrating $HRES$ with Microgrid. The third section will look at energy management in the chosen hybrid microgrid, with a focus on power quality and management issues.

The chapter 2 introduces modeling of the selected microgrid with distributed $HRES$ components, with a focus on PV power system-based generation feeding the DC bus. The first section goes over the mathematical model of the PV cell/array, the boost converter, and the Maximum Power Point Tracker $MPPT$ algorithm in detail. An analysis of PV system models simulated in MATLAB and Simulink with the goal of selecting an accurate model for building PV-based generation. The DC/AC interlinking three-phase Pulse Width Modulation PWM inverter is presented in the second section, where the (PWM) technique is presented and discussed, followed by the entire state space model of the power filter system.

Chapter 3 provides a robustified voltage controller for the DC/AC inverter based on auto-calibration of adjustable fractional weights to improve power quality. The first section uses literature reviews to address the issue of power quality. The second section covers the design of the current loop's sliding mode control and the outer loop's voltage controller. The proposed robust voltage control technique is described in the next section, which includes a full explanation of different forms of fractional weights. The chapter comes to a close with frequency and time domain simulations, as well as a review of the control results that have been generated.

Finally, a robust Power Management Control (PMC) method for microgrid systems based on a closed-loop fractional fuzzy controller is presented in the fourth chapter. the problematic of PMC is presented in the first section with literature review. The second section contains a full description and modeling of the system components, with the third section being the design of the fractional fuzzy logic controller. The selected Social Spider Optimisation Algorithm (SSO) for the optimisation parameters of the system is described in section four. The remaining two parts cover

the objective function and the discussion of simulation results.

This work will be concluded with a general conclusion, including a synthesis of the work carried out, and some notes for future work will be noted.

Chapter 1

The State of the Art

1.1 Introduction

Recent environmental regulations have promoted the research of new energy sources due to the rate of continued growth in global demand for electricity. Many industries and households have oriented their focus on the use of renewable energy structures. However, in comparison to demand, the rate of production from these sources remains modest. Under these circumstances, the production of power plants based on renewable sources continues to expand, with various topologies for generating electricity having been given in the literature, including the microgrid that is the subject of this study. In order to study the microgrid components and structures, this chapter will present definitions and terms that will be frequently referred to as microgrid topologies in the rest of this thesis. Thus, we'll start the chapter with a presentation of PV and wind as the primary renewable energy sources, as well as the energy storage system. The integration of renewable energy sources, as well as the restrictions and operating modes, energy conditioning, and interface, are explored in the second section. The challenges that the energy management system encounters are then outlined after the choice of distributed generation systems.

1.2 Future Prospects of Microgrids in Algeria

Algeria's climate is characterized by several microclimates owing to its location on both sides of a tropical zone. The climate is hot, sunny, and dry in the sahara, where the thermal amplitude between day and night frequently exceeds 35 or 40 $^{\circ}C$. The coastal zone and Algerian Sahara are characterized by extremely high wind speeds [4]. This means that both wind and solar energy are extensively applicable all over the country.

The expansion of energy provided by renewable sources is Algeria's national priority. So, solar and wind energy have grown as more serious and efficient alternatives for increasing the overall power system's supply security and dependence on oil and gas as principal energy sources.

Since the 1970s, the government's initiative program has pushed for the utilization of renewable energy sources. In 2015, Algeria updated its Renewable Energy and Energy Efficiency Development Plan for 2030. The program's modified version plans to build 4,5 GW for of new plants by

2020, with a total capacity of 22 GW by 2030 [3]. However, until 2018, fossil fuels dominated the energy mix (Figure 1.1) [5], with natural gas accounting for 63.8%, oil 35.4%, and coal 0.6%, and renewable energies accounting for 0.1% (IEA, 2020a). Solar energy is currently positioned in the first position, but now wind power production is also being strengthened (Figure 1.2) [5]. However, it appears that what has been achieved so far in implementing renewable energy programs is very modest.

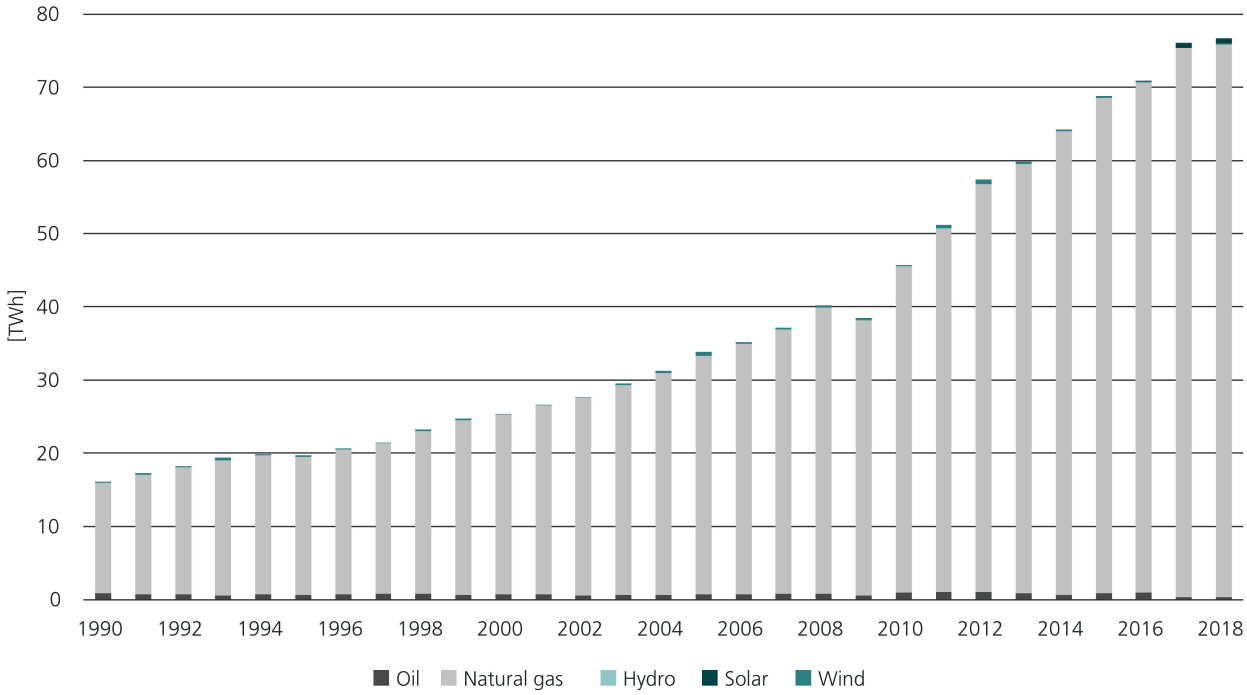

Figure 1.1: Electricity Generation by Source (TWh), Algeria 1990–2018

.

In the past two years, the government has taken some significant measures to expedite the energy transition program's execution. Beginning with the establishment of a Ministry of Energy Transition and Renewable Energies to promote renewable energies and ensure the energy transition program's implementation. Furthermore, separating energy from the Ministry of Mines allows the second ministry to concentrate on conventional energy's principal activities. This will be followed by the establishment of the National High School for Renewable Energies, Environment, and Sustainable Development in June 2020, which will be responsible for ensuring high training, academic research, and technological advancement in the fields and divisions of renewable energy [6].

Among the measures taken as part of the energy transition roadmap is electrifying remote ar-

eas with standalone systems, which are not suitable economically and geographically to extend the conventional networks' power supplies to the remote areas [3]. For this reason, the creation of microgrids for consumption will be an interesting solution to satisfy the growing rate of electricity demand in remote and rural areas. The microgrid is part of the electrical system and is very dynamic. It is also able to contribute to increasing energy conversion efficiency, transmission and distribution.

Hence, the intermittent nature of renewable energy sources limits the development of sustainable microgrids. These limitations must be taken into account in the design and control of microgrids [7]. The importance of considering system operation and economic frameworks that are geared toward the nature of intermittent $HRES$ is growing [8]. On the other hand, there are concepts for microgrids that have been adapted from control methods used in other systems.

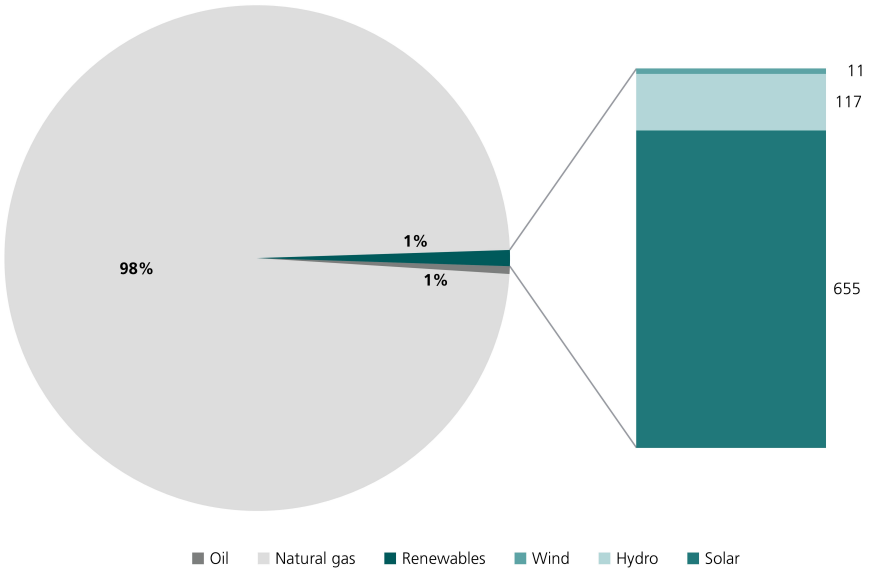

Figure 1.2: Electricity Generation (GWh), Algeria 2018

.

As a result, an assessment of Algeria's establishment of microgrids in remote areas shows that the government has recognized this as an important part of the energy transition. The plans in the regulatory framework also show that Algeria has put energy efficiency measures into practice at the political level. However, the target has not yet been achieved, which means that Algeria is in the first phase of its energy transition.

1.3 Renewable Energy Sources

With the growth of power generation systems, environmentally friendly renewable energy sources (such as photovoltaic devices and wind electric generators), clean and efficient fossil-fuel technologies (such as micro-gas turbines) and hydrogen electric devices (fuel cells) as scheduled energy sources, there is an interest in clean and environmentally friendly practices. Furthermore, gas-fired micro-turbines with outputs ranging from 25 to 100 KW may be mass-produced at a low cost by employing airbearing and recuperation to achieve respectable efficiency. In addition, fuel cells have the potential to completely change power generation due to their zero-emission, high efficiency, and dependability [9]. Hydrogen can be obtained directly from natural gas or regenerated from liquid fuels such as alcohol or gasoline.

Renewable energy is electricity generated from naturally intermittent resources such as wind, sunlight, tides, waves, and geothermal heat [10]. Recently, renewable energy has received a lot of attention from researchers and governments because of its environmental benefits and resource continuity. In this thesis, two intermittent energy sources, namely wind and the sun, will be assessed. Because of increased fuel prices and the desire to reduce carbon emissions, solar and wind power generation system applications are becoming more common [11, 12]. Within the current electricity systems, Solar Photovoltaic (PV) and Wind Turbine Generator (WTG) have the fastest growth rates of all renewable energy producing systems. Based on the variations of atmospheric conditions, there is a widely acknowledged design strategy for the two source power systems. In the next two subsections, two well-known preliminary design methodologies were explored.

1.3.1 Solar Photovoltaic System

The sun's light energy is regarded as one of the most abundant and readily available energy sources. It is a significant renewable energy source. The sun's heat can also be captured as thermal energy and used for solar-powered heating systems. The solar power conversion process is classified as active or passive solar depending on the type of energy capture and delivery. The active solar technique makes use of Solar Photovoltaic (PV) systems, Concentrated Solar Power (CSP), and solar

heating systems, whilst the passive solar technique makes use of materials with thermal properties and light dispersion properties.In practice, CSP power system is the heat generated by the reflection of sunlight using mirrors and lenses [13]. The PV power system, which is discussed in this work, is a conversion of photons to electric current. The energy held in photons from the sun is absorbed by electrons in semiconductor materials, and electricity is created in the form of a DC current. Typically, a single PV cell can typically provide 1 to 2 $Watts$ of power, and it is linked in series and parallel with other PV cells to create a PV module. Similarly, a group of PV modules can be linked together to create a PV array.

Consequently, the power output of a PV module depends on the number of cells in the module, the type of cells and the total surface area of the cells. Manufacturers rate all modules based on their peak power under specified test circumstances. The goal of determining the maximum power tracking of each cell, on the other hand, is to determine the maximum power tracking of the entire PV array. However, each PV array is linked to others to form a PV module that is connected to the grid via an inverter. The PV module output power can be expressed as [14],

$$P_{PV} = \eta S \phi \{1 - 0.005(T_a + 25)\} \tag{1.1}$$

where $\eta(\%)$ is the percentage of PV conversion efficiency, S (m^2) is the area of the PV panels.The power mainly depends on solar insolation and ambient temperature which are represented by ϕ (k_w/m^2) and T_a ($^\circ C$) respectively. Due to its advantages, solar energy has become the most promising alternative source for conventional power generation systems. Of these advantages, it is faster in design and installation time, with noiseless operation and less maintenance due to its stable structure, and, of course, global availability. However, the uses of a photovoltaic energy production system are limited due to its high initial cost and low energy conversion efficiency. Fortunately, as new technology makes them acceptable and attractive to renewable systems, this initial cost will be lowered.

1.3.2 Wind Turbine Generator

The wind is a free, clean, and inexhaustible energy source [15]. Winds arise from the uneven heating of the atmosphere by the sun, the irregularities of the Earth's surface, and the Earth's rotation. The land terrain and buildings modify the patterns and speed of wind flow through them. When harvesting the wind flow by wind turbines, electricity can be generated. The terms "wind energy" or "wind power" describe the process by which the wind is used to generate mechanical power or electricity. Wind turbines convert the kinetic energy stored in the wind to electricity, which is known as wind power. Wind power generation is now widely regarded as a viable alternative to traditional power generation technologies [16].

A Wind Turbine Generator (WTG) is a complex electromechanical system formed by blades that are connected to the rotor's shaft. The blades capture the wind energy and transform it into rotational mechanical energy in the shaft. It is linked to the electrical generator to generate electricity. The amount of power generated depends on the speed of the upstream wind, turbine size, and swept area. The air density and the cube of wind velocity are closely related to the energy yield of a wind turbine. The WTG mathematical model of the output power output is given by [16, 14] by the following expression,

$$P_{WTG} = \frac{1}{2}\rho A_r C_p V_w^3 \tag{1.2}$$

where $A_r(m^2)$ and C_p are the swept surface of a turbine's blades and the coefficient of power, respectively, and $\rho\,(KG/m^3)$ indicate air density, which is typically constant for a given installation site. Wind speed is symbolised by V_w.

Horizontal Axis Wind Turbines ($HAWT$) and Vertical Axis Wind Turbines ($VAWT$) are the two main types of wind turbines. The $HAWT$'s blades rotate on an axis parallel to the ground, as the name implies. $VAWT$ refers to when the blades are positioned so that their rotating axis is perpendicular to the ground. When compared to the $VAWT$, the $HAWT$ is capable of producing more electricity. The reason for this is that the $HAWT$ has a larger swept area than the $VAWT$. As a result, the $HAWT$ is commonly used in commercial $WTGs$. $VAWT$, on the other hand, is employed for low-power applications [17].

A resourceful tool must be present in order to quickly correct for power and load fluctuations in order to maintain a constant balance between generation and demand. Thus, the utilization of Battery Energy Storage System ($BESS$) units can be easily integrated by knowing the number of batteries and the total power that release or absorb power. A $BESS$ system contains electrochemical cells for energy storage that can convert chemical energy into electricity. In the given proposed structure, if the sum of power generation by solar arrays and wind turbines is greater than the load demand, the excessive energy is stored in the battery. On the contrary, if the load demand is greater than the produced energy from renewable units, the deficiency in load demand is compensated by battery discharge. In charge/discharge mode, the amount of stored/dumped energy in the battery is defined as follows :

Even though renewable energy has the potential to replace traditional energy sources in the future, there is still some uncertainty about its cost and efficiency. Governments, associations, and researchers have all put a lot of effort into overcoming these barriers. In fact, the type of the source or variations in atmospheric conditions, such as solar irradiance and wind speed, have a significant impact on renewable energy conversion efficiency, particularly solar and wind.

1.3.3 Integration of Renewable Energy Sources

In recent years, as the world has grown more cognizant of global warming, a market for integrating renewable and green energy sources has emerged. Distributed generation is developing as a new technology in deregulated power markets. In this context, the microgrid concept provides value to Distributed Energy Resources (DER) by aggregating them into autonomous grids. In addition, as interest in large-scale integration grows, the concept of a microgrid has been proposed, which combines power generation, storage, distribution, and consumption into a single network that uses advanced regulating algorithms to link the supply of abundant renewable resources to the demand of local consumers.

Microgrids that can run as isolated islands in critical operational circumstances are now conceivable thanks to the smart grid. The restructuring facility integrates various technologies in the areas of protection, control, and real-time pricing. Participants wishing to improve the dependabil-

ity, sustainability, and capabilities of customer choices in energy systems can now use the smart grid [18]. The central stone of modern energy model disputes is distributed or decentralized power generation, as seen by smart electricity networks and electrical microgrids. These are typically made up of a group of Distributed Generators (DGs) that can operate in isolated islands to supply a group of electrical loads, or they can be connected to the common electricity network to support part of the network's electrical energy needs by injecting surplus, or all of the energy produced. These microgrid applications may also eliminate the need for large-scale high-voltage line additions to transmit renewable energy across densely populated areas around the world. However, I believe that changes in the electric power business will actually transform the way we supply electricity from microgrids.

The applications of solar photovoltaic, which typically follow the daily demand profile for power generation, on-site or local wind energy, and storage devices for microgrid installations, might provide a cost-effective and long-term solution for supplying microgrid loads.

In real time, the energy from the microgrid is combined by multiple renewable energy generators and a range of energy storage technologies. Similarly, it can integrate a wide range of industrial utilities and commercial loads. Figure 1.3 presents a case of the typical microgrid system. The system contains two renewable energy sources: Solar Photovoltaic (PV), Wind Turbine Generator (WTG) and Battery Energy Storage System ($BESS$). The term Hybrid Renewable Energy System ($HRES$) is used to describe the combination of two or more intermittent sources. This case study gives an idea for energy management of a $HRES$ by using locally available renewable energy resources. The design of the higher-level control algorithm that calculates the proper power level to be generated and its split across the power sources is referred to as an Energy Management System (EMS) or Power Flow Controller (PFC) [19].

As a result, a wide range of scholars are interested in integrating intermittent renewable energy sources into microgrids. From the standpoint of reliable operation and control, the increasing interest poses significant challenges. To handle these challenges, several methods have been offered to overcome these difficulties based on designs, controls, and optimization techniques. In this discipline, they provide the fundamentals of power electronics, control and sensor technology, computer technology, and communication systems. Furthermore, researchers in this scenario confront a sig-

nificant challenge in improving power quality and management while ensuring energy management [20, 21, 22].

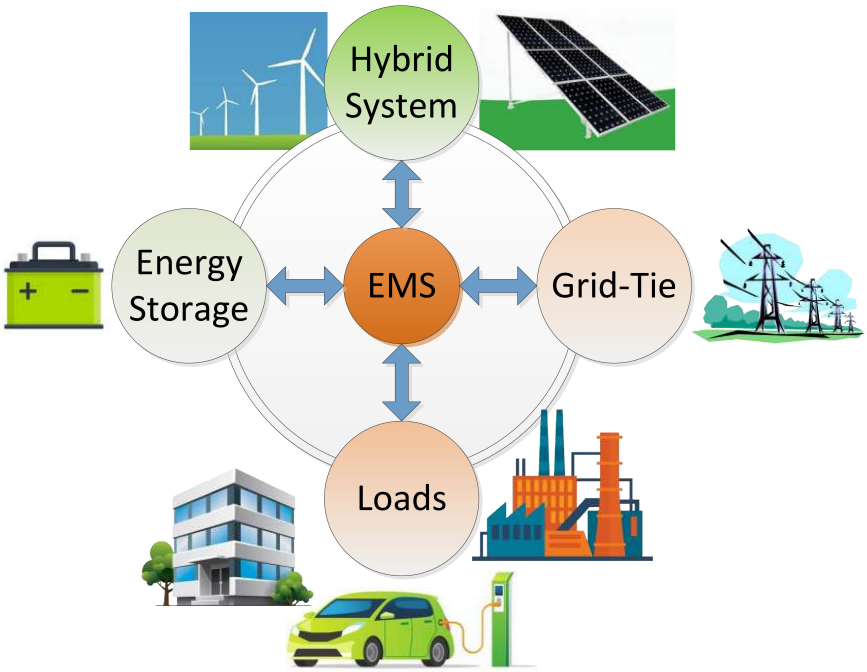

Figure 1.3: Energy management system.

1.4 Interfacing Renewable Energy Sources with Microgrid

The main goal of this project is to introduce EMS into the control of $HRES$ power systems. Topological design is required in microgrid planning to assure certain features of EMS, such as energy-saving and power quality, from various components of the $HRES$. Topology is a critical problem in the proposed control since it depicts the dynamic process of underlying systems. The challenge entails selecting the microgrid nodes where $HRES$ generators should be placed for maximum efficiency, as well as optimizing the microgrid. We need to choose the topology of $HRES$ systems with dynamic process conveyables to develop control methods and accomplish the control objectives. In reality, many recommendations in the literature are focused on bus configurations. Thus, the microgrid can be categorized into three topologies: DC microgrid, AC microgrid, and hybrid (AC/DC) microgrid [23, 24]. The three subgroups are presented with detailed descriptions as follows:

1.4.1 DC Microgrid

It's a typical structure with a single DC bus (Figure 1.4) that connects all sources and DC loads via their respective converters. Through DC/AC converters, the DC bus is connected to the AC loads [25, 26]. Several publications in the selection adapted this type of configuration. They defend their decision by claiming that the DC design is more efficient, less expensive, occupies less space, has a lower lifetime cost and is more reliable. Furthermore, because only voltage stability is addressed, employing a DC setup helps to avoid the frequency violation problem. However, this setup has a number of drawbacks. In reality, the battery with bidirectional inverter is responsible for delivering the power in a DC-bus system. The capacity of resources exceeds the capacity of the battery at the generated peak energy, resulting in a loss of generated energy and restricting the system's performance [26].

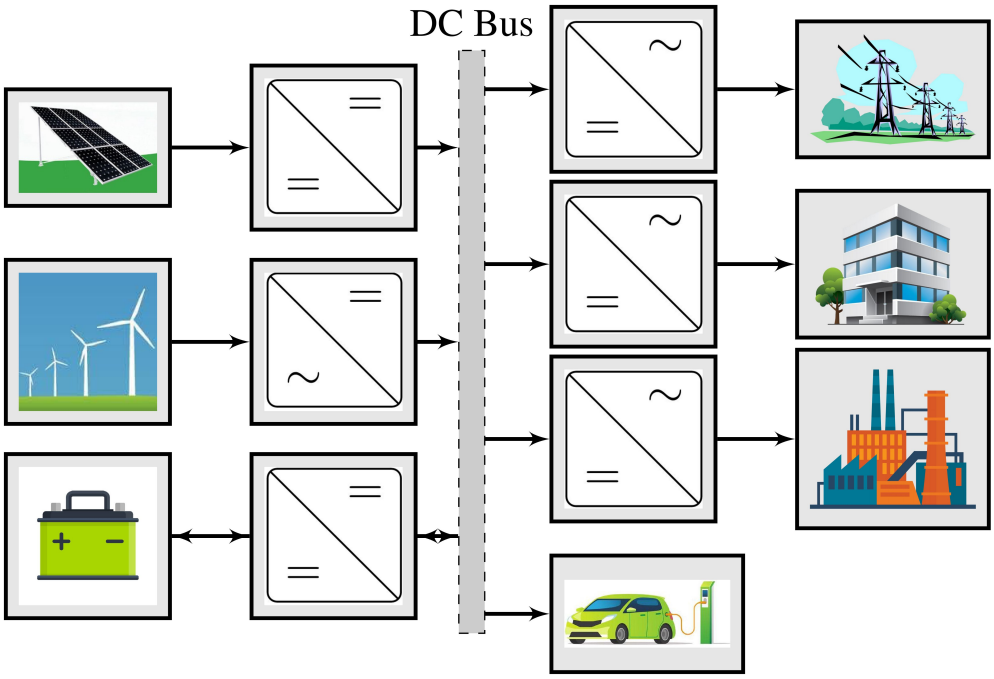

Figure 1.4: DC microgrid.

1.4.2 AC Microgrid

Consists of a centralized AC bus that can manage a high number of AC loads and sources As illustrated in Figure 1.5. It offers an AC medium for regulating the interactions of various components

[26]. The DC components are linked to the AC bus through DC/AC converters. For example, PV panels are linked to the AC bus via an AC inverter and the batteries are connected via a bidirectional converter or a paralleled inverter and rectifier in such systems. The centralized AC arrangements operate at a greater operating voltage, resulting in lower wire cable losses [27]. Moreover, unlike DC arrangements, $HRES$ may give direct power to consumers. By minimizing the number of charge/discharge cycles the battery's projected lifetime is increased and the DER is better used. Nonetheless, this design necessitates additional safety precautions (e.g., frequency stabilization) which makes the installation cost slightly higher than that of the DC configuration. Compared to the latter, the fewest papers have adopted the AC configuration.

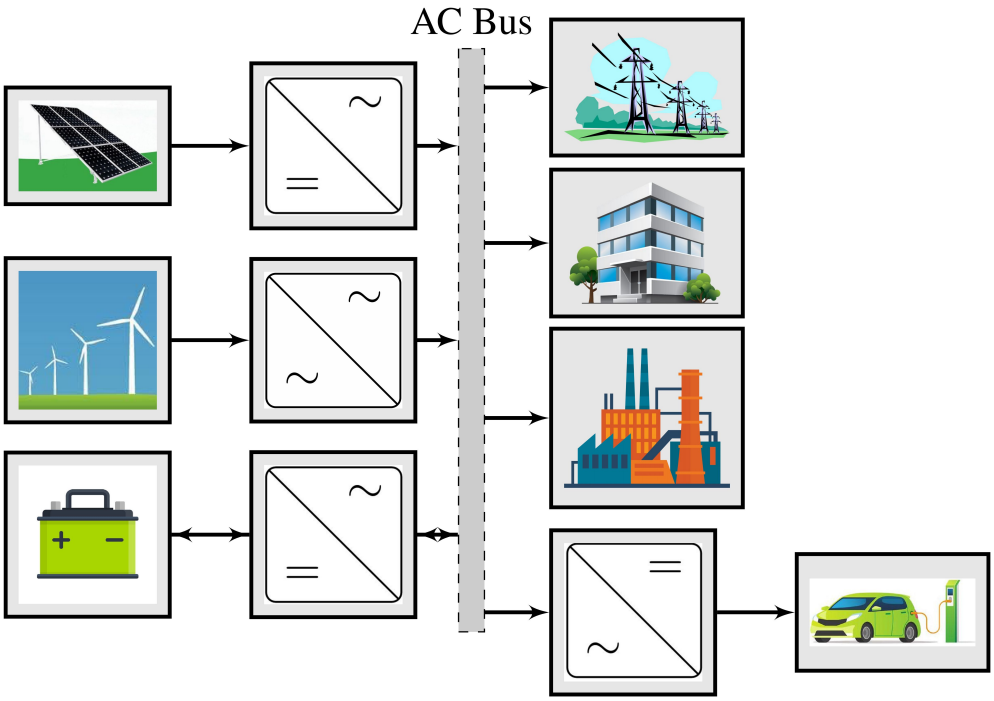

Figure 1.5: AC microgrid.

1.4.3 Hybrid Microgrid

The last and the newest configuration is a hybrid DC/AC coupling bus configuration. As illustrated in Figure 1.6, this bus configuration consists of two main buses: a DC bus connecting the sources and an AC bus connecting the loads. Using a bidirectional inverter, the two buses are linked together. Because it is feasible with many sorts of loads and sources, this arrangement has the ad-

vantage of benefiting from both prior setups . However, every component is linked to either the DC or the AC bus, depending on its technical purpose it needs minimal conversion requirements and fewer power converters, resulting in lower system costs. Yet, such a design necessitates more cooperation between DC and AC buses in terms of control approach. In reality, bus voltage (and frequency) activities that are synchronized must be considered [20].

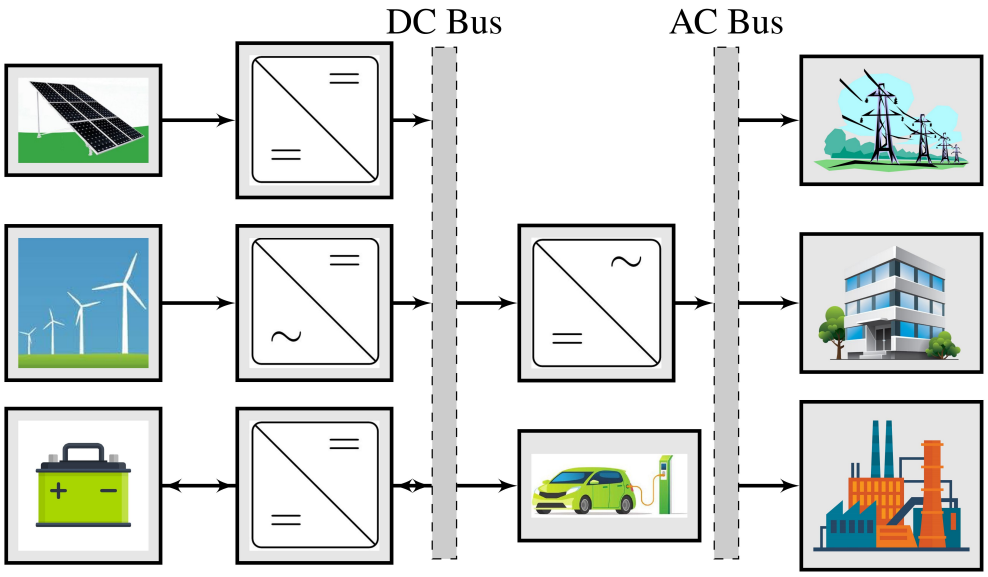

Figure 1.6: Hybrid microgrid.

While determining the kind of microgrid, the loads and sources must be considered [28]. Compared to conventional power systems, AC microgrids have been built first, and a number of studies have been conducted, notably on the question of power sharing of parallel-connected sources [29]. Since there are many renewable energy sources that generate DC power or need a DC link for grid connection, and as a result of increasing modern DC loads, DC microgrids have recently emerged for their benefits in terms of efficiency, cost, and systems that can eliminate the DC-AC or AC-DC power conversion stages and their associated energy losses [30, 28]. However, since the majority of the power grids are presently AC, AC microgrids are still dominant, and purely DC microgrids are not expected to emerge exclusively on power grids. Consequently, DC microgrids are prone to being developed in AC types even though they are subordinate. To the best of our knowledge, the idea of a combination of both configurations gives an enhanced structure that incorporates the primary advantages of both AC and DC designs [31]. In most cases, a hybrid microgrid is used

to eliminate the need for many AC/DC converters [31, 32]. However, with fewer converters, the hybrid microgrid's costs and losses are lower [33].

As a result, this configuration requires additional research and effort to be integrated into the main grid. Primarily, the thesis will focus on this topology, with future trends showing identification, modeling, design, and control structures.

1.5 Energy Management in Microgrid

Energy management is essentially a multiobjective optimization problem [34]. The EMS is primarily concerned with lowering operational costs [35]. However, unlike conventional electricity power systems, it is complex to design a reliable and robust EMS schemes. Therefore, considering the many control tasks involved in the operation of a microgrid, a hierarchical approach has been used for building microgrid control systems. The hierarchical control structure's goal is to better manage the installation more precisely by providing more robustness to the microgrid. As shown in Figure 1.7, EMS in microgrids with hierarchical control structures may be split into three control layers: primary, secondary, and tertiary. The primary control layer, also known as the local control layer, is responsible for tracking local voltage, frequency, and current references and power sharing control. The secondary control layer, also known as EMS, is responsible for the microgrid's reliable and cost-effective operation by supervisory controllers for frequency, voltage, re-dispatching the generation, adjusting $BESS$ charging and discharging, curtailing surplus renewable power, or shifting/shedding controllable loads. Besides, the secondary control is also used to compensate the deviation in frequency and voltage caused by the primary control [36, 37]. Indeed, it provides the greatest degree of hierarchical control of isolated microgrids with access to all the required information in the microgrid [38]. The tertiary control layer is the highest level in the control hierarchy of grid-connected microgrids. Energy management at the tertiary-level can be achieved by involving the optimization of power import/export transactions between the microgrid and the utility grid, as well as between the microgrid and other nearby microgrids. The tertiary controller and the EMS can be combined to create a control architecture with only two levels. The review of the most popular EMSs discloses the third control layer [39]. Furthermore, a large

amount of control research has been carried out on secondary control layer as a solution to EMS schemes.

1.5.1 System Under Study

The focus is to build a dynamic simulation model of a $HRES$ distributed generation system and apply a control approach to this model with better active power quality and minimum delivered energy cost [40]. At present, the topology of a typical hybrid microgrid is shown in the Figure 1.7. In the proposed architecture, a three-stage topology in grid-connected mode is designed to overcome the challenges posed by energy-saving strategies. Other designs are also possible using many methods for energy generation, transmission, and distribution. The architecture is essentially the same as in Figure 1.6 of the hybrid microgrid. We use the term "bus" because these points of interconnection are copper bars that connect elements of the hybrid microgrid [41].

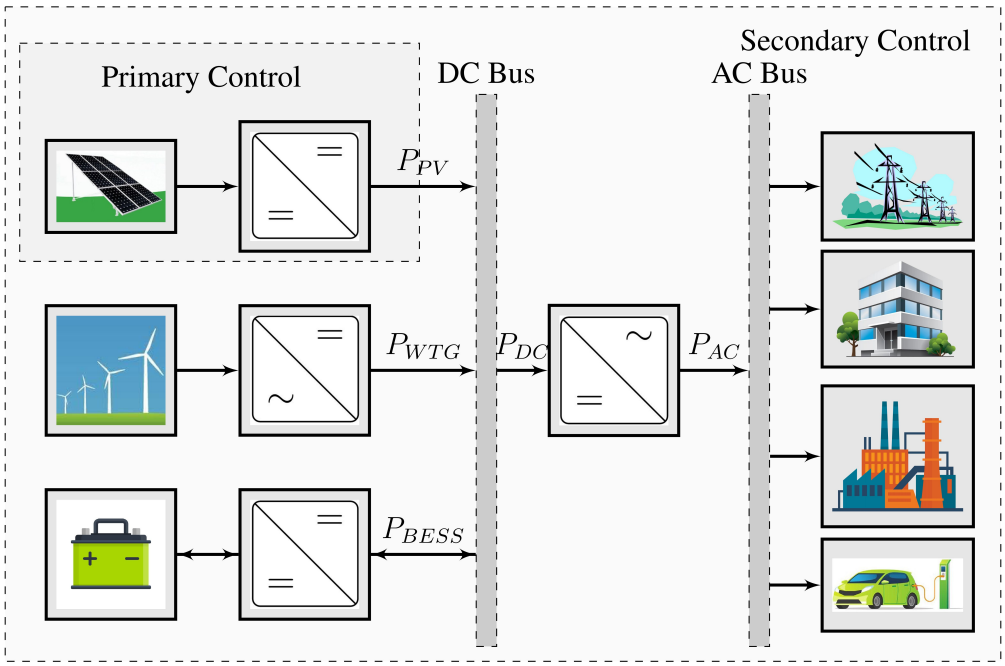

Figure 1.7: Proposed hybrid microgrid control topology.

Various DG units, such as PV, WTG, and $BESS$, are included in the first stage, and their outputs are connected to a common DC bus. A three-phase converter is used to convert the DC bus power to an AC bus in the second step. The utility grid and loads are included in the third stage. In this architecture, the section of the system connected to the local utility has a synchronized power

system frequency, and the AC bus has an inverter frequency. In fact, transmitting a large amount of power from sources to lines at low voltages would result in a significant loss of power. In this scenario, we must increase the voltage while decreasing the current. This problem was solved using power transformers [29]. For example, in the topology of an AC microgrid, any $HRES$ unit needs a transformer to step up the voltage from the DC/AC converter to the AC bus, unlike the case of a hybrid microgrid. The drawback is that the transformers are bulky, heavy, and costly components.

In the first stage, three subsystems have been built to allocate energy from DGs to the DC bus. The first subsystem is a PV-based generation system that uses an equation-based one-diode PV cell model. Using a boost converter, the PV panels' output is increased to the appropriate level. The Maximum Power Point (MPP) is tracked using the Perturb and Observe (P&O) method. The second subsystem is made up of a WTG that is chosen for modeling. The AC output voltage from wind turbines is converted to DC, and the DC voltage is then boosted to the necessary level using an $MPPT$-controlled boost converter. In the last subsystem, the energy storage device $BESS$ has four states: charging, discharging, standby state under unsaturated conditions, and the microgrid system's excess energy is fed back into the public grid.

The AC and DC buses are connected by a three-phase inverter that generates three-phase alternating voltage and current at a fixed frequency of 50 or 60 cycles per second at low standard voltages ranging from 208 to 600 V for three-phase. Furthermore, the inverter must have active power filter capabilities to compensate for the effect of harmonically corrupted load current/voltage by pumping compensatory current into the power system via real-time control. The objective of these controls is to have the line current/voltage be as sinusoidal as feasible. The attached tiny capacitors are added to the load side to offer further harmonics filtering and load voltage stability. Here, the distribution transformer is linked to the inverter's output side. Interconnected mode is also utilized to enhance and improve the power grid's resilience for steady operation and cost reduction. In this topology, the output voltage and frequency are directly dependent on the DC bus voltage, inverter control, and load changes.

In grid-connected mode, the inverter gets its reference voltage and frequency from the grid. Hence, it is a challenging task to maintain these variables constant while managing the EMS scheme. The inverter's control implementation must be centered on the power quality problem.

This may be accomplished by proposing a DG-inverter-based control approach ready to satisfy EMS purposes. In short, in order to keep the system stable, the dynamic response of the proper controller for the DG inverter must be well-defined. Furthermore, the employment of Pulse Width Modulation (PWM) technology as part of the inverter controls allows the control of load frequency and voltage. Finally, to remove undesirable harmonics, stabilizing compensator control of the AC bus voltage is needed. Such a study will help researchers better understand the DG-connected inverter's control potential and its role in energy saving. To further understand and clarify the control methodology, it's helpful to look at earlier research that used different EMS methods to improve the power quality in the presence of unwanted harmonics.

Controlling the balance between consumption and supply is a substantial problem for distributed generation (DGs) systems, especially for $HRES$ systems, due to the high imbalance in the generation energy sources, uncertainty of weather and demand circumstances. Here again, we need to develop a Power Management Controller (PMC) strategy to mitigate the power oscillations and maintain stability [42]. Therefore, it's a necessity to update traditional control strategies to maximize the power conversion from $HRES$ components by improving the system's dynamics response and verifying the EMS purposes. The development of this control system technology is vital to ensure a sustainable hybrid microgrid with a significant renewable energy supply contribution. The same problem needs to be investigated with a comprehensive overview of $HRES$ with an emphasis on performance for a wide range of power system operating conditions.

Thus, the EMS system has two categories of controllers that operate in parallel and are used for energy-saving purposes in the hybrid microgrid power system. A literature review in-depth attention to existing solutions and specific problems will be given within the scope of research as mentioned above.

1.6 Overview on Control of Microgrid

The role of voltage control of the interlinking DC/AC inverte in islanded microgrid mode is to provide better quality power to the local loads using a variety of control techniques, including state feedback control, robust control, sliding mode control, and fractional PID control. On the other

hand, the hybride fractional fuzzy logic controller will be employed for power management. For the reader's convenience, we will quickly describe some of the basic ideas and notions of these controls that will be needed in this work.

1.6.1 State Feedback Control

The inverter voltage was controlled using standard linear control theory. One method relies on an analog control algorithm based on a transfer function model and a canonical lead-lag compensator. A state-space-model-based state feedback control approach is an extension of this strategy. To obtain optimal performance, this technique adds a linear quadratic index to classic linear state feedback control.

1.6.2 Standard H_∞ Control

A robust H_∞ control for uncertain linear systems utilizing a basic state-space approach may be formulated for controller handling [43]. In some circumstances, the H_∞ based on loop-shaping for robust controller design approach does not function well under nonlinear load, severely limiting its use in voltage control of an inverter with fluctuating loads and system uncertainty. The addition of the structured singular value (μ) notion allows one to assess the system's stability under the worst-case perturbation scenario. In the voltage control, both H_∞ loop-shaping and μ-analysis approaches are used without parametric uncertainty, which weakens the system [44].

Thus, the H_∞ design approach can be used to improve the robust stability of an inverter control in the presence of model uncertainty and load disturbance using advanced control approaches.

1.6.3 Sliding Mode Control (SMC)

SMC has been used in a wide range of applications, including robotics, power control, aerospace, and process control. The SMC's most notable feature is its sensitivity to parameter changes and external disturbances. Many scholars have recently been interested in discrete-time SMC research [45]. The chattering problem is, however, one of its significant drawbacks in practical usage. Several strategies for eliminating this phenomenon in SMC have been proposed [46]. Because of its

order reduction characteristics and low sensitivity to disturbances and plant parameter variations, SMC is an effective instrument for regulating the current of inverter with discrete control of complex high-order dynamic plant operating under uncertainties. In this technique, the control variable in each sampling period is calculated based on the plant model and feedback quantities.

1.6.4 Fractional PID Control

Fractional PID is an extension of regular integral calculus (PID) to non-integer case. In comparison, fractional controller is adequate and natural to fully characterize many physical phenomena [47]. In general, the extra degrees of freedom from the use of fractional-order integrator and differentiator could further enhance the control performance compared with that of traditional integer-order controller. Noticing, the implementation $FOPID$ controller needs to approximate its fractional part of powers by the usual integer transfer functions with a similar behavior. The method is based on approximating of laplacien non-integer exponential in a specified frequency range [48]. The transfer function and approximation manner are well presented in the appendix A.

This is a classical method of voltage control of an inverter based on proportional-integral (PI) regulation to track sinusoidally varying inputs. Since a PID controller only guarantees zero steady-state error under DC reference input, this control technique cannot be convincing in control performance. This method has been extended by using fractional control to compensat the classical model. So that the control design has to be able to handle arbitrary input, which is possible yield to a good control performance for microgrid applications.

1.6.5 Fuzzy Logic Control

Fuzzy logic control is a system that evaluates analog control input in terms of logical variables and maps them to fuzzy sets, which are continuous values between 0 and 1. There are three primary components to a fuzzy controller procedure. The first of them is fuzzification, which processes and fuzzifies inputs using defined membership functions. The second element, the rule-based inference system, uses these fuzzified inputs. To create a fuzzy response, this system employs previously stated linguistic rules. In the final step, called defuzzification, the fuzzy response is defuzzified. As

a result of this procedure, a real number will be produced.

Easy implementation, flexibility, tolerance of imprecise input, nonlinear functions may be modelled for arbitrary complicated control, the ability to mix with traditional control systems, and the fact that it is based on natural communication [46]. These are all reasons to choose a fuzzy logic controller in the power management system.

1.7 Conclusion

The themes developed during this chapter have made it possible to situate the context of the thesis work. Indeed, a first step was devoted to the future prospects of microgrids in Algeria as a solution to the energy transition. The second step was devoted to the study of microgrid $HRES$ components. It has been highlighted that these sources of generation provide better solutions in response to the increase in energy needs, socio-economic requirements, and environmental concerns. A third step was, moreover, devoted to the description of topologies for interfacing these sources. In this direction, a hybrid microgrid was selected as the best solution, taking into account many considerations. Also, several layers of control are envisaged. Finally, in the scope of the research on control techniques in microgrid systems, we have given a brief overview of some of them that will be used later.

Chapter 2

Modeling of the Hybrid Renewable Energy System

2.1 Introduction

In this chapter, the distributed renewable energy generation system in the hybrid microgrid will be addressed. However, special attention will be given to the PV system. In the first section, a detailed model has to be developed and validated based on the specification parameters of the PV panel. The requirements dictate the type selection and sizing of the DC/DC boost converter, which integrates the PV array into the DC bus. Further, discussing the calculation of the parameters of each PV system component, such as the one-diode PV panel, PV array, and boost converter, will also be discussed in this part. The DC/AC converter is then introduced in the following section, which includes a detailed presentation of the PWM technique and a full steady-state model of the power filter.

2.2 Modeling of the Distributed Renewable Energy Generation System

Considering the above surveys, an energy management structure is recommended for this work. The under-study $HRES$ system is a crossbreed of PV arrays, wind turbine and battery, as shown in Figure 1.7. The power from renewable sources is transferred to the DC bus system through power inverters. The common DC bus system is utilised in order to integrate the distributed generation along with the energy storage system. Moreover, PV arrays are connected to a DC bus via a DC/DC converter, which can be utilized to enable best energy management control of grid-connected PV system. In this system, to control the power and voltage on the boost output, Maximum Power Point Tracking ($MPPT$) methodology can be used for voltage amplification and to maintain a constant PV voltage in the event of partial shading. The Wind Turbine Generator (WTG) is linked to a DC bus system through an AC/DC converter. To get the required DC link voltage at a desired value, the rectifier is needed. In addition, the Battery Energy Storage System ($BESS$) consists of a battery bank and a bidirectional DC/DC converter for the power transition. This chain is used to compensate the system load power deficiencies and improve the system reliability. The $BESS$

system will store energy in case of production excess and will be an energy source in order to provide a continuous load supply. The DGs systems are then connected to DC/AC inverter to supply installed loads (buildings, industrial customers, electric vehicles,...) and electricity network. Its transition from a DC bus to an AC bus system is achieved through a 3-phases voltage converter with an associated power filter and a Δ-Y transformer.

In order to develop a correct component-based model of the hybrid microgrid system, it is therefore necessary to model the conversion of energy component by component in order to investigate the performance of the overall system. The primary goal of this section is to examine the solar system's interface with the load via power electronics inverters. Accordingly, a full component-based model of a PV system includes a boost inverter connected to a three-phase DC/AC inverter.

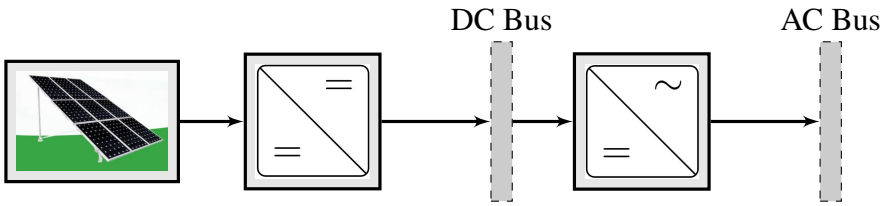

Figure 2.1: Structure of dual stage PV system

Figure 2.1 shows the block chain of the PV system where the DC/AC inverter and boost are linked to the DC bus and AC bus, respectively. The inverters are linked by input and output voltage controls where the boost inverter keeps the output voltage constant by maximising the boost output DC power before the DC bus. The three-phase inverter with PWM technique and the additional function of a power filter are used to interconnect the PV system model to the load. Typically, a grid-connected inverter will have an influence on the generators' (PV, wind turbine) power output and has to be considered during the analysis and modelling of the PV performance. Similarly, wind energy and battery systems can be interfaced with the DC bus using the same methodology as in the study on the modelling and designing of the PV system.

In the next step, methodology of the study is focused on the modelling and designing of the PV system components.

2.3 Model of Photovoltaic System

As explained in the previous chapter, there are numerous ways to connect the solar panel. In the configuration shown in Figure 2.1, the boost inverter is used to interface the PV array with the DC bus. In this technical section, the photovoltaic chain will be focused on the boost converter with a maximum power point controller, which is utilized to track the PV's MPP. The overall subsystem structure is depicted in Figure 2.2.

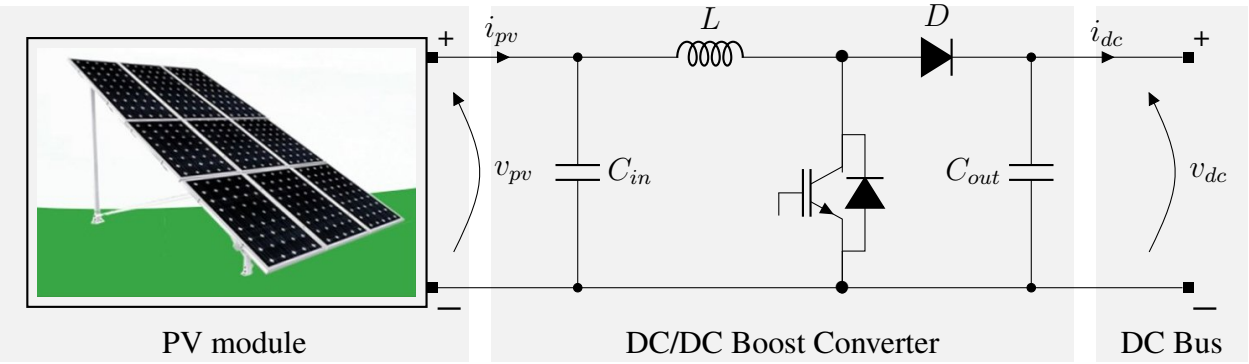

Figure 2.2: Schematic of PV system with boost converter

This topology allows us to examine the effectiveness of the maximum power point control mechanism as well as the PV's ability to achieve maximum power at different temperatures and irradiance. On the other hand, the structure depicted in Figure 2.1 is composed of the DC/DC and DC/AC inverters to connect the PV array to the AC bus.

It should be mentioned that a PV module is made up of a series or parallel connection of cells. To create a PV array, PV modules are joined in series and in parallel. As a result, the values of different parameters characteristic of the PV cells are obtained while using the basic description of the equivalent circuit of the PV cells to build the mathematical model of the PV array. The solar module's manufacturer provides the additional characteristics required to simulate the solar cells. The datasheet that offers the electrical properties is computed under standard test conditions when the temperature is 25 $^{\circ}C$ and the irradiance is 1000 W/m^2 [49].

2.3.1 Modeling of Photovoltaic Array

A photovoltaic cell (PV cell) is a semiconductor p-n junction that converts sunlight to electrical power. To model a PV cell, we must first assess the impact of various factors on the solar panels, as well as take into account the parameters listed in the datasheet by the manufacturers. An electrical equivalent of a one-diode, resistance series R_s and resistance parallel R_p, is generally used to represent a PV cell.

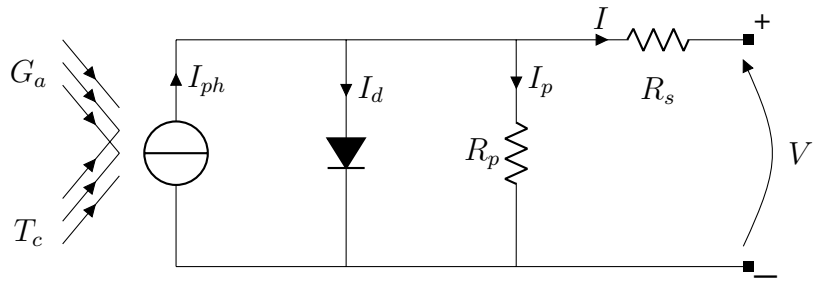

Figure 2.3: One diode model of the solar cell

Figure 2.3 depicts the PV cell's one-diode equivalent model, where $G_a(W/m^2)$ is the irradiance from the sunlight, $T_c(K)$ is the cell temperature, I_{ph} is the photon current produced by the solar cell, I_d is the diode current given by Shockley equation, I_p is the current leak in parallel resistor and I, V are the output current and voltage of the PV cell, respectively.

By applying Kirchhoff's law, the output current of the PV cell will be obtained by the equation,

$$I = I_{ph} - I_d - I_p \tag{2.1}$$

According to the equation 2.1, the output current of a PV module containing N_s cells in series will be [50, 51]:

$$I = I_{ph} - I_0 \left[exp\left(\frac{V + R_s I}{V_t a}\right) - 1 \right] - \frac{V + R_s I}{R_p} \tag{2.2}$$

where I_0 is the leakage current of the diode or reverse saturation of the PV module. The thermal voltage of the module is defined by $V_t = N_s kT/q$ (V) where k is the Boltzmann constant $[\ 1.3806503 * 10^{-23} J/K]$, $T(K)$ is the temperature of the p-n junction, q is the electron charge

$[\ 1.60217646 * 10^{-19}C]$ and a is the diode ideality constant ($a = 1$ for an ideal diode). In 2.2, R_s and R_p are the equivalent series and parallel resistances of the PV module, and their equivalent values for a PV array are $R_s\frac{N_s}{N_p}$ and $R_p\frac{N_s}{N_p}$ respectively, where N_p denotes the number of parallel connections between PV cells. In addition to the series and parallel resistances, the photovoltaic and saturation currents of the array may be determined by the expressions: $I_{ph} = I_{ph,cell}N_p$, $I_0 = I_{0,cell}N_p$, where N_p denotes the number of parallel connections between PV cells.

The fundamental equation 2.2 represents the nonlinear $I - V$ characteristic of a practical PV array. The parameters of this equation are difficult to establish. However, this model has the greatest fit with experimental data. The number of parameters varies based on the model used and the searchers' assumptions. The single-diode model is ideal for power electronics designers who want to simulate photovoltaic systems with power converters in a simple and practical way.

Photovoltaic array manufacturers provide only a few experimental data about electrical and thermal characteristics instead of the I-V equation. For example, according to the specs listed in the datasheet of BP-MSX-120 PV aray (see Appendix B) [52], it has 72 solar cells (silicon nitride multicrystalline) in series and provides 120 W of nominal maximum power. The voltage at the maximum power point is 33.7 V, and the current supplied is 3.56 A [53]. Table 2.1 lists the typical electrical characteristics of the BP-MSX-120 module, which are necessary for modeling the PV array.

Table 2.1: BP MSX120 datasheet at STC.

Parameters	Values
Short circuit current I_{sc}	3.87 A
Open circuit voltage V_{oc}	42.1 V
Current at maximum power point I_{MPP}	3.56 A
Voltage at maximum power point V_{MPP}	33.7 V
Number of cells in series N_s	72
Temperature coefficient of I_{sc}	(0.065±0.015)% $°C$
Temperature coefficient of V_{oc}	-(80±10) $mV/°C$
Maximum power P_{max}	120 W

The included PV module datasheets is usually presented in terms of nominal or standard test conditions for temperature and solar irradiation (STC). Unfortunately, some of the parameters needed to adjust photovoltaic array models, such as the light-generated or photovoltaic current I_{ph}, the series and parallel resistances (R_s, R_p), the diode ideality constant "a" and the diode reverse saturation current I_0. For an analytical solution to these five parameters, I-V curves for various irradiance and temperature settings are provided by several manufacturers. These curves make tuning and checking the required mathematical equation much easier. Essentially, this is all the information available from the PV array datasheets. In the proposed PV power system, a PV array of 100 BP-MSX-120 modules has 10 parallel connections of 10 module strings connected in series. Each module has a nominal power of 120 W, resulting in a maximum power output of 12 KW and an output voltage of 337 V. The parameters of a 12 KW PV panel are listed in Table 2.2.

Table 2.2: Characteristics of 12 kW PV array.

Parameters	Values
Number of modules in a string series N_{ss}	10
Number of modules in a string parallel N_{pp}	10
Output voltage rating	337 V
Output current rating	35.6 A
Maximum power output	12 KW

The specification parameters of the BP-MSX-120 module and the 12 KW PV array are given in Table 2.3.

Table 2.3: PV module/array parameters values at STC

Parameters	Module	Array
I_{ph} (A)	3.8713	38.71
I_0 (μA)	0.323	3.23
a	1.3977	1.3977
R_s (Ω)	0.473	0.18
R_p (Ω)	1367	520

Simulink was used to simulate the PV array, which was based on the model from [51]. The first setup is used to determine the PV array's (I-V) curve characteristics and display the maximum power point. The data from the manufacturers was then compared to the depicted curves. The model's output characteristic curves must match the PV panel's characteristics.

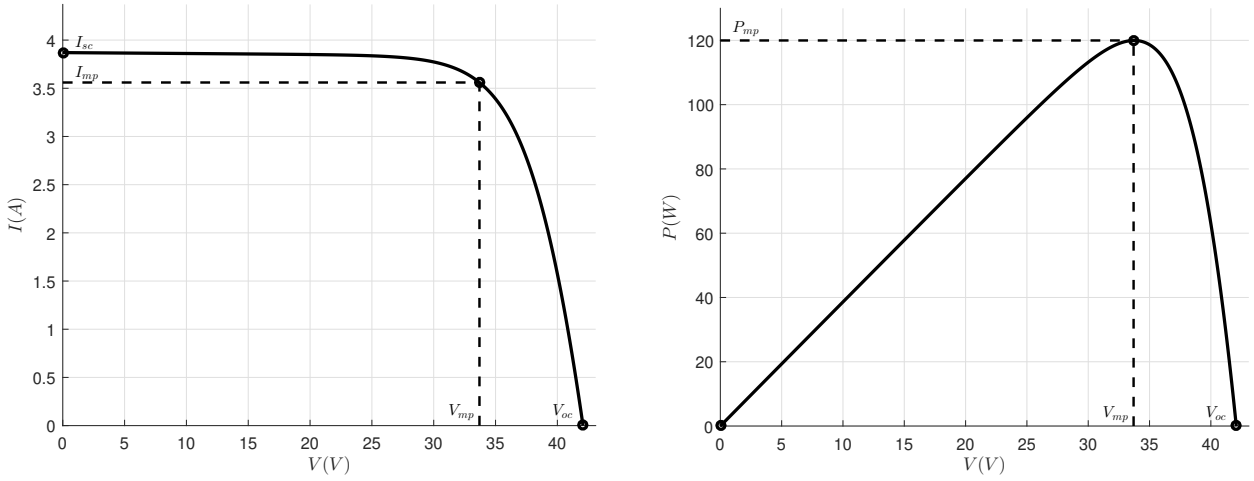

(a) $V - I$ *curve* (b) $V - P$ *curve*

Figure 2.4: V-I and V-P curves of PV panel.

The (I-V) characteristics of the BP-MSX-120 PV module are shown in Figure 2.4a. It should be noted that the nonlinear curve highlights three points: short circuit (0, I_{sc}), maximum power point (V_{mp}, I_{mp}), and open circuit open-circuit (V_{oc}, 0). The values of the parameters I_{sc} = 3.87 A and V_{oc} = 33.7 V are identical to the manufacturer's values in Table 2.1.

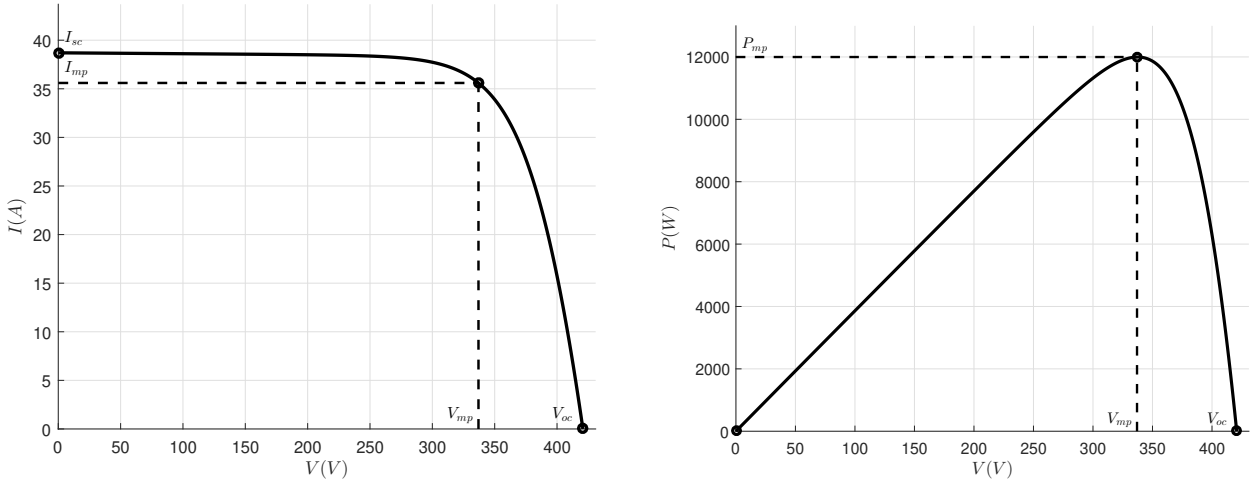

(a) $V - I$ *curve* (b) $V - P$ *curve*

Figure 2.5: V-I and V-P curves of PV array.

Thus, there exists a unique operating point on the (V-I) curve known as the Maximum Power Point (MPP) on the array characteristics. As a result, special techniques are required to keep the PV array operating at the MPP using calculation models and search algorithms [54].

2.3.2 DC/DC Boost converter stage

In the hybrid microgrid system, the DC-DC converters are required to step up or down the DC bus voltage. The microgrid architecture presents different types of renewable energy sources that can operate either in DC by their operation or by including a DC bus. In our case, the boost converter is placed between the PV source and the DC bus in the PV power system. The DC/DC stage's main purpose is to step up the PV's low DC voltage input into a higher DC voltage output. Also, the boost converter is commonly used to locate the PV array's ultimate point of power. Figure 2.6 depicts the boost converter circuit's topology.

The boost converter can operate in two modes: Continuous Conduction Mode (CCM) and Discontinuous Conduction Mode (DCM). The mode of conduction is determined by the energy storage capacity as well as the switching time frame. The duty cycle affects the output voltage, which is regulated by the maximum power controller. The Maximum Power Point Tracker ($MPPT$) adjusts the PV voltage at the maximum power point using a DC/DC converter. As depicted in the figure, the DC input voltage V_{pv} is in series with an inductor L, which works as a current source.

The switch is connected in parallel with the current source, which cycles on and off, supplying energy from the inductor and source to raise the average output voltage. C_{pv} is the power decoupling capacitor that is connected in parallel with the PV array. To compensate for variations in the PV's output voltage, a DC link capacitor C_{out} is added between the PV and the inverter. Furthermore, the C_{out} capacitor is big enough to maintain a constant output voltage, and the inductor delivers energy while the switch is open, boosting the voltage across the load.

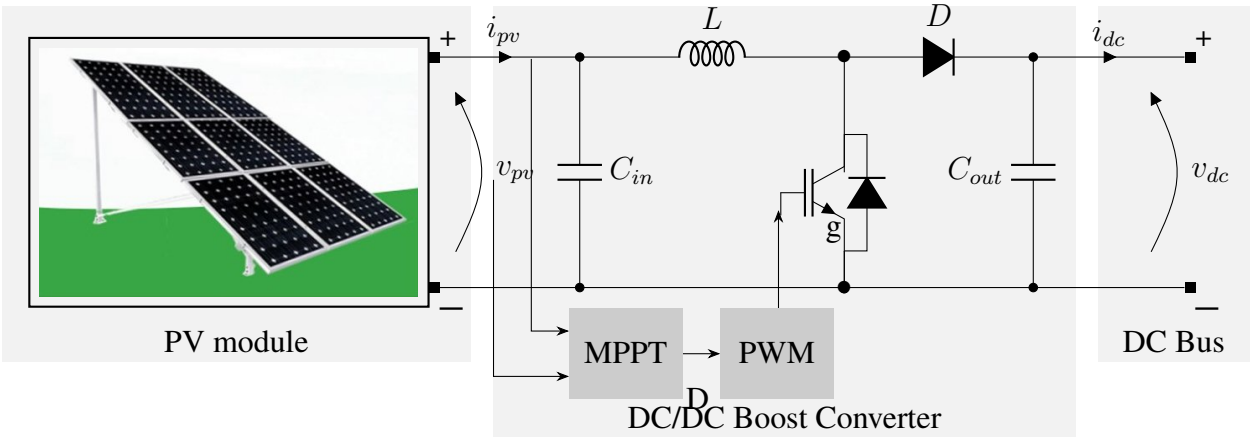

Figure 2.6: Block diagram of PV system with MPPT algorithm

The voltage ratio for a boost converter is calculated using the assumption that the time integral of the inductor voltage is zero during the switching time. The voltage ratio refers to the ratio of the switch's switching period to its off time. Then, as a function of duty cycle, the relationship between the output voltage and the input voltage is;

$$\frac{V_{dc}}{V_{pv}} = \frac{T_s}{T_{off}} = \frac{1}{1-D} \tag{2.3}$$

where,

T_s: total switching period,

T_{off}: switching off of the IGBT,

D: duty cycle.

As indicated in 2.3, the output voltage of the converter is always higher than its input voltage.

Assuming that we want to realize a boost converter under a nominal input voltage of $V_{pv} = V_{mp} = 337V$ to have a nominal output voltage of $V_{dc} = 540V$. The duty cycle is obtained from 2.3 as:

$$D = 1 - \frac{V_{pv}}{V_{dc}} = 0.3759 \tag{2.4}$$

The maximum inductor current at maximum input power is used to determine the inductor. The value of the boost converter's inductance is given by;

$$L \geqslant \frac{V_{dc}D(1-D)}{f_s|\Delta I_{Lripple}|} \tag{2.5}$$

V_{dc}: maximum of the dc component of the output voltage,

D: duty cycle of the switch at maximum converter input power,

f_s: switching frequency,

$\Delta I_{Lripple}$: ripple current of the inductor.

Considering an ideal converter without losses, the output power tends to be the same as the input power. The output current can be expressed as;

$$I_{dc} = \frac{P_{pv}}{V_{dc}} = \frac{12000}{540} = 22.22A \tag{2.6}$$

The volume of the inductor and their current ripples can be decreased by increasing the switching frequency. Assuming a peak ripple current through the inductor of 10% at a 10 KHz switching frequency, we find;

$$L \geqslant \frac{540 * 0.3759(1-0.3759)}{10^4 * 35.6 * 0.1} = 1.8\mu H \tag{2.7}$$

The input capacitor C_{pv} of the boost converter is determined as;

$$C_{pv} \geqslant \frac{I_{om}D_m^2}{0.02(1-D_m)f_s V_{pv_{mpp}}} \tag{2.8}$$

I_{om}: output current at maximum output power,

$V_{pv_{mpp}}$: PV output voltage at maximum power point.

Finally, the parallel capacitor's value is determined by the minimum ripple voltage ΔV_{dc}. It is represented as follows;

$$C_{dc} \geqslant \frac{V_{dc} D}{f_s \Delta V_{dc} R_{load}} \tag{2.9}$$

The PV array's output voltage is affected by temperature and insolation changes. C_{dc} plays a significant role in the lowering of voltage ripple and enables energy storage for a limited period of time and rapid voltage changes.

2.3.3 Searching MPPT algorithm

A number of researchers have worked on $HRES$ power systems in terms of enhancing the $MPPT$ tracking algorithm, optimal PV-wind or combination of $HRES$ source placement, EMS systems, and optimization strategies for $HRES$ system size. The MPP functioning of a PV generating station is used to determine the final design of a PV system.

Figure 2.3 presents the implementation of the overall system, which consists of a PV panel, boost converter, $MPPT$ controller, and gate drive when the system is connected to a DC bus. Accordingly, various $MPPT$ algorithms have been published in the literature depending on the application, with differences in various parameters such as algorithm complexity, necessary sensors, convergence speed, and the need for periodic controller tuning [55]. The most well-known $MPPT$ algorithms are Perturb & Observe (P&O) [56], Hill Climbing [57], and Incremental Conductance (IncCond) [58]. Both algorithms, P&O and Hill Climbing, use the same fundamental strategy. In the Hill Climbing method, the duty ratio is the perturbation, whereas the voltage is the perturbation for the P&O algorithm. Basically, adjusting the duty cycle leads to a change in the current, which causes the voltage array to also be perturbed. Because of its simplicity and general nature, the P&O algorithm is perhaps the most commonly used $MPPT$ method today. To further comprehend the $MPPT$ algorithm's performance with PV systems, we'll briefly review the principle through the P&O method. In the conventional P&O method, the voltage and current are measured, and the $MPPT$ controller determines the voltage reference. In addition, the output voltage presents the reference given by (V_{ref}). The difference between V_{ref} and measured V_{pv} voltage presents the input

of the PI regulator. For each step, the $MPPT$ controller reads the voltage and current of the PV generator output to determine the PWM signals for the boost converter.

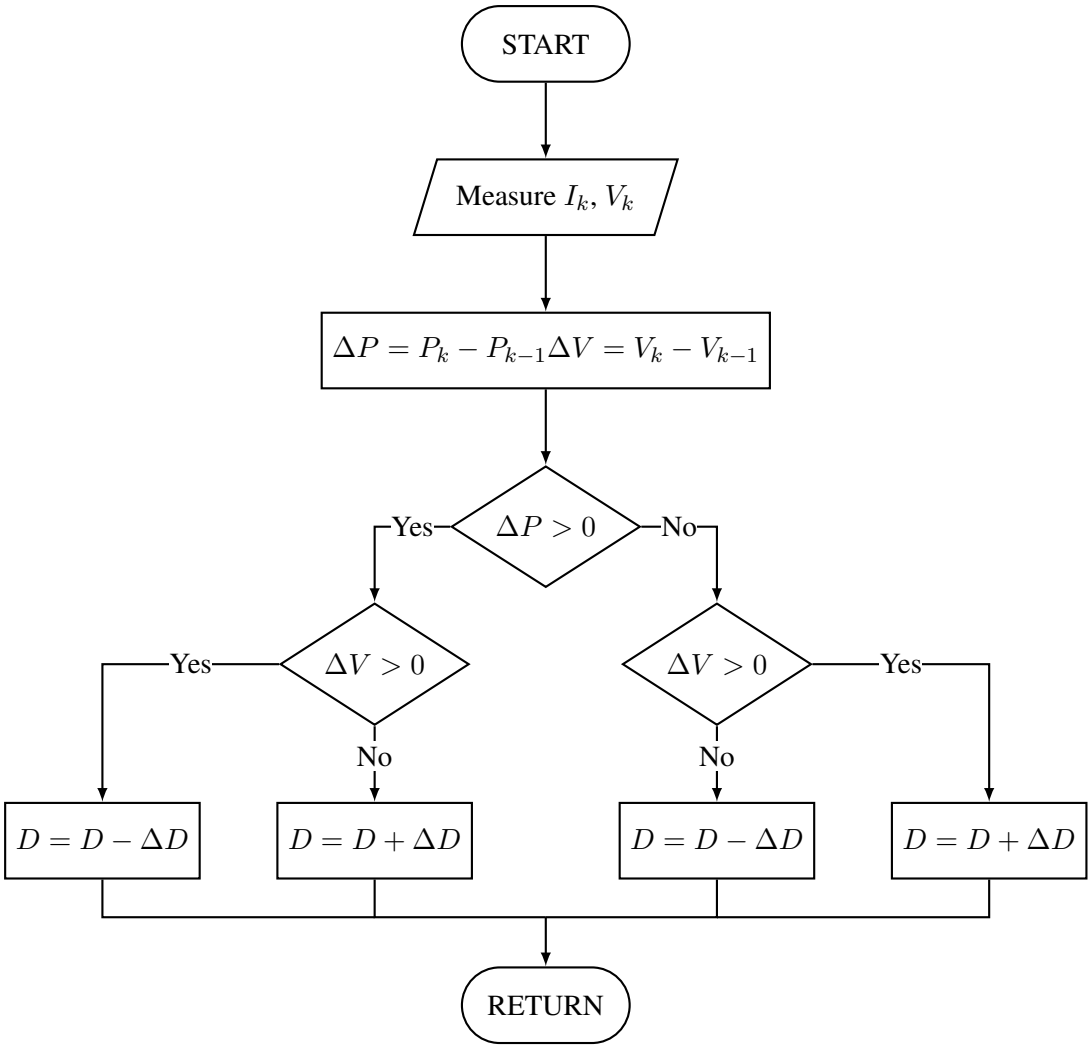

Figure 2.7: Flow chart of P&O MPPT algorithm

The P&O method's operating concept is represented in Figure 2.7. When operating on the left side of the MPP, it can be seen that incrementing (decrementing) the PV voltage increases (decreases) the PV's power. On the right of MPP, incrementing (decrementing) the voltage reduces (raises) the power. With this strategy, the system oscillates around the MPP point. Under fast variations in irradiation, the process decrements or increments might fail in this case. If the irradiance suddenly increases, the operating point of the PV array system diverges away from MPP [59]. To address these issues, improved P&O $MPPT$ methods are used, including reduced perturbation step size, variable step size, three point weight comparison methods, and optimized

sampling rate.

2.4 Modeling of the DG-Connected Inverter

The power circuit layout of the recommended three-phase PWM voltage source inverter is shown in Figure 2.8. For hybrid microgrid interface applications, this is the most common inverter architecture. The DG-connected inverter system consists of a three-phases voltage converter with $L-C$ filter and a Δ-Y transformer. Small capacitors C_{load} at the load side to provide further harmonics filtering and stabilization of the load voltages. The line-to-neutral load voltages are denoted as $\vec{V}_{load}$ and load currents $\vec{I}_{load}$, the line-to-line inverter filter capacitor voltages are denoted as $\vec{V}_f$ and the inverter currents are denoted as $\vec{I}_f$. The DG bus voltage through the individual inverter is assumed to be an ideal DC voltage source. The leakage inductance L_t, series resistance R_t and currents $\vec{I}_{snd}$ are the secondary winding parameters [60, 61].The control technique developed in this work is based on the technique proposed by Marwali [62].

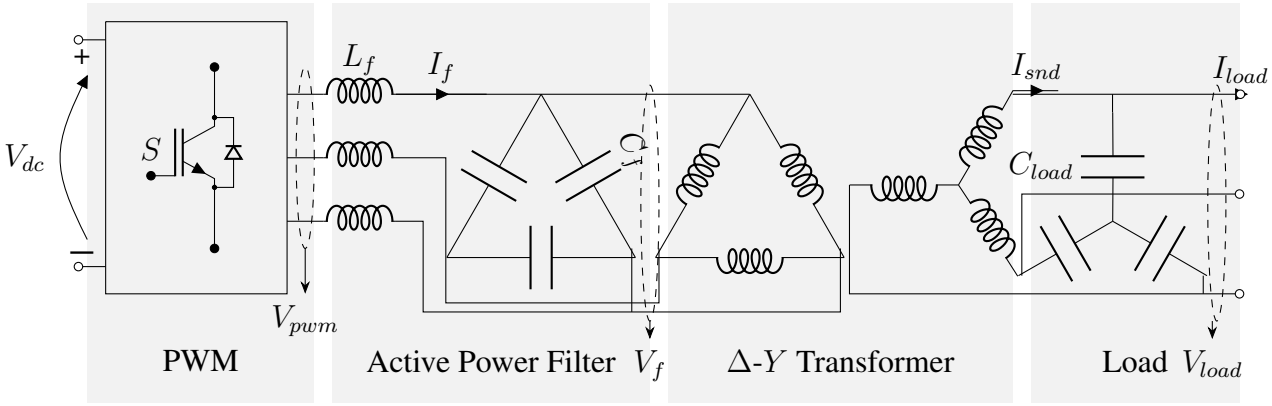

Figure 2.8: Power converter system.

2.4.1 Space Vector PWM Technique

Different types of three-phase inverters are used to interface the $HRES$ system in the hybrid microgrid in the presence of AC and DC buses. In The three-phase inverters, the pulse width modulation (PWM) technique is the most commonly employed method for in power electronics for modulating high-power voltage or current waveforms using low-power signals. The three-phase PWM

voltage source inverter is designed for interfacing solar power system and its DC bus output voltage discuted in the previous subsection.

Figure 2.9 shows a schematic illustration of a typical three-phase voltage-source inverter system. Six semiconductor switches, such as $IGBTs$ and $MOSFETs$, are utilized in the switching devices, along with anti-parallel diodes for protection. In a small dead band between two switching devices on one leg, two power switches are employed. Each phase output voltage is connected to the midpoint of each inverter leg. The output voltage is shaped by the switches S_1 to S_6, which are controlled by the switching settings. As a consequence, the output voltage may be calculated using the ON and OFF states of the upper inverter switches S_1, S_3, and S_5. As a result of the combined switching of these three switches, eight possible output voltage vector states are accessible depending on the switching states. Notice that the ON and OFF states of the lower power switches are opposite to the upper ones.

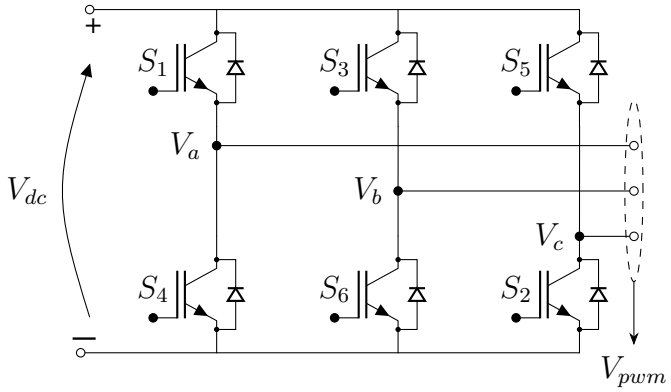

Figure 2.9: Three-phase voltage source PWM inverter.

The node voltage oscillates between the upper and lower DC bus voltages by turning on the upper and lower switches alternately. The output voltages of each leg are V_{an}, V_{bn}, and V_{cn}, with "n" referring to the negative DC bus voltage determined from the DC bus voltage, V_{dc}, and the switch positions.

Table 2.4 shows the eight inverter output voltage vectors ($V0$ to $V7$), as well as phase and line-to-line voltages in terms of normalized DC bus voltage V_{dc}.

Table 2.4: PWM Output voltage

Voltage vectors	Switching states			Line to neutral voltage			Line to line voltage		
	a	b	c	V_{an}	V_{bn}	V_{cn}	V_{ab}	V_{bc}	V_{ca}
V1	1	0	0	$\frac{2}{3}$	$-\frac{1}{3}$	$-\frac{1}{3}$	1	0	-1
V2	1	1	0	$\frac{1}{3}$	$\frac{1}{3}$	$-\frac{2}{3}$	0	1	-1
V3	0	1	0	$-\frac{1}{3}$	$\frac{2}{3}$	$-\frac{1}{3}$	-1	1	0
V4	0	1	1	$-\frac{2}{3}$	$\frac{1}{3}$	$\frac{1}{3}$	-1	0	1
V5	0	0	1	$-\frac{1}{3}$	$-\frac{1}{3}$	$\frac{2}{3}$	0	-1	1
V6	1	0	1	$\frac{1}{3}$	$-\frac{2}{3}$	$\frac{1}{3}$	1	-1	0
V7	1	1	1	1	1	1	1	1	1
V8	0	0	0	0	0	0	0	0	0

As indicated in the table, for a three-phase PWM voltage source inverter, only six fixed nonzero voltage vectors and two zero vectors can be obtained. A voltage vector can be generated by various possible combinations of these eight fixed vectors. According to that, PWM's three-phase switching sequences are another control option for achieving the best switching waveform based on the modified PWM technique.

A number of PWM techniques have been developed and are used in power inverter controls to generate sinusoidal waveforms. However, only three of them have become standards and have most often been applied in practice: Naturally Sampled Sine PWM ($NSPWM$), Uniformly Sampled Sine PWM ($USPWM$), and Space Vector PWM ($SVPWM$). Among them, $SVPWM$ algorithms offer great flexibility to optimize switching waveforms and are well suited for digital implementation.

The typical $SVPWM$ methodology maps the eight switching patterns into six 60°-apart space vectors within the same plane and two 0-axis vectors orthogonal to the plane, and a reference vector on the plane is used as a modulation signal and determines the time average of such switching patterns in each PWM cycle, similar to the original PWM technique. As a result, the $SVPWM$

approach is a process for generating a reference-signal-modulated pulse sequence by modulating the temporal width of a pulse train in response to a reference signal. The sinusoidal reference voltage is modeled as a fixed-amplitude vector rotating at a specific frequency.

Every space vector is transformed from the Cartesian coordinate frame to the dq synchronous reference frame to facilitate the design and digital implementation of the $SVPWM$ technique. The aim of the $SVPWM$ approach is to create the average output voltage of the inverter in a little time which is the same as the reference voltage vector V_{ref} in the same period using the eight switching patterns.

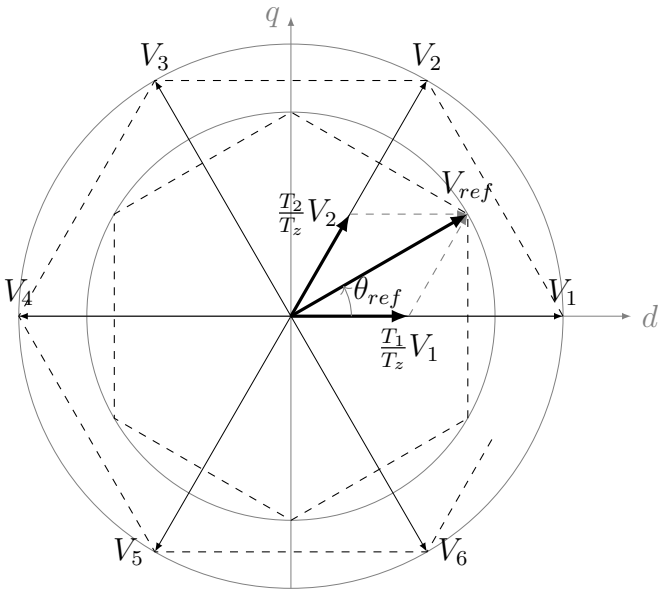

Figure 2.10: Three-phase voltage source PWM inverter.

Figure 2.10 geometrically depicts the basis vectors for PWM, where successive non-zero vectors in the plane form six 60° sectors representing one full sinusoidal cycle. A sinusoidal reference signal can be represented as a vector in the same frame that rotates from sector to sector at a constant speed. In each sector, V_{ref} can be obtained by time-averaging the two boundary basis vectors and the two zero vectors with appropriate weights.

However, the requisite PWM switching frequency for satisfactory performance should be higher than the reference frequency. In Figure 2.10, T_1 (T_2) is the duration of Vector V_1 (V_2) in one-half T_z of the PWM cycle, obtained from the values of V_{ref} and θ_{ref}. Zero states are among

the remaining time ($T_0 = T_z - T_1 - T_2$). Based on the $dq - axis$ reference frame theory, the three phase voltages transformed into two-dimensional perpendicular frame by the following expression: $\vec{V}_{dq} = K_s \vec{V}_{abc}$ where the transformation matrix K_s is defined as;

$$K_s = \frac{2}{3} \begin{bmatrix} 1 & -\frac{1}{2} & -\frac{1}{2} \\ 0 & -\frac{\sqrt{3}}{2} & \frac{\sqrt{3}}{2} \\ \frac{1}{2} & \frac{1}{2} & \frac{1}{2} \end{bmatrix} \tag{2.10}$$

Therefore, $SVPWM$ can be implemented by determining voltages (V_d, V_q, V_{ref}), angle θ_{ref} as follow;

$$\begin{bmatrix} V_d \\ V_q \end{bmatrix} = \frac{2}{3} \begin{bmatrix} 1 & -\frac{1}{2} & -\frac{1}{2} \\ 0 & -\frac{\sqrt{3}}{2} & \frac{\sqrt{3}}{2} \end{bmatrix} \begin{bmatrix} V_{an} \\ V_{bn} \\ V_{cn} \end{bmatrix} \tag{2.11}$$

$$|\overline{\mathrm{V}}_{ref}| = \sqrt{V_d^2 + V_q^2} \tag{2.12}$$

$$\theta_{ref} = \tan^{-1}(\frac{V_q}{V_d}) = 2\pi f t \tag{2.13}$$

where f = fundamental frequency.

Time duration of T_1, T_2 and T_0 are then calculated using the sector number, angle, and sampling time. The region determination block obtains the region in which the vector falls according to the fundamental frequency and then the switching time of each sector (S_1 to S_6). Finally, the calculated parameters and variables of the standard $SVPWM$ algorithm are then used in the design of the three-phase inverter.

2.4.2 Active Power Filter System Modeling

The output of the Active Power Filter (APF) circuit's dynamic equations can be written as follows;

$$\begin{cases} 3C_f \frac{d\vec{V}_f}{dt} = \vec{I}_f - Tr_i \vec{I}_{snd} \\ L_f \frac{d\vec{I}_f}{dt} = \vec{V}_{pwm} - \vec{V}_f \\ C_{load} \frac{d\vec{V}_{load}}{dt} = \vec{I}_{snd} - \vec{I}_{load} \\ L_t \frac{d\vec{I}_{snd}}{dt} = -R_t \vec{I}_{snd} + Tr_v \vec{V}_f - \vec{V}_{load} \end{cases} \tag{2.14}$$

where $\vec{V}_{pwm}$ is the inverter line-to-line voltage vector fed to the L – C filter, $\vec{I}_f$ is the inverter current vector, $\vec{V}_f$ is the line-to-line voltage vector on the Δ side of the transformer, $\vec{V}_{load}$ and $\vec{I}_{load}$ are the voltage and the current vector of the Y side of the transformer, respectively. The current and voltage transformations of the transformer are represented by matrices Tr_i and Tr_v. Therefore, if Tr represents the turns ratio of the transformer, these matrices are generated by:

$$Tr_i = Tr \begin{bmatrix} 1 & -2 & 1 \\ 1 & 1 & -2 \\ -2 & 1 & 1 \end{bmatrix}, Tr_v = Tr \begin{bmatrix} 0 & 0 & -1 \\ -1 & 0 & 0 \\ 0 & -1 & 0 \end{bmatrix} \tag{2.15}$$

Convert the dynamic nonlinear equations of the system to the $dq - axis$ stationary frame of reference using the following transformation: $\vec{V}(\vec{I})_{dq} = K_s \vec{V}(\vec{I})$ for voltages (currents) vectors. The three-phase inverter system's circuit dynamic equations in the $dq - axis$ reference frame can therefore be recast as follows;

$$\begin{cases} 3C_f \frac{d\vec{V}_{f_{dq}}}{dt} = \vec{I}_{f_{dq}} - Tr_{i_{dq}} \vec{I}_{snd_{dq}} \\ L_f \frac{d\vec{I}_{f_{dq}}}{dt} = \vec{V}_{pwm_{dq}} - \vec{V}_{f_{dq}} \\ C_{load} \frac{d\vec{V}_{load_{dq}}}{dt} = \vec{I}_{snd_{dq}} - \vec{I}_{load_{dq}} \\ L_t \frac{d\vec{I}_{snd_{dq}}}{dt} = -R_t \vec{I}_{snd_{dq}} + Tr_{v_{dq}} \vec{V}_{f_{dq}} - \vec{V}_{load_{dq}} \end{cases} \tag{2.16}$$

where $Tr_{i_{dq}}$ and $Tr_{v_{dq}}$ denote the new current and voltage transformation matrices, respectively; they are defined as;

$$Tr_{i_{dq}} = \left[K_s Tr_i K_s^{-1} \right] = Tr \frac{3}{2} \begin{bmatrix} 1 & \sqrt{3} & 0 \\ -\sqrt{3} & 1 & 0 \end{bmatrix} \tag{2.17}$$

$$Tr_{v_{dq}} = \left[K_s Tr_v K_s^{-1}\right] = Tr\frac{3}{2}\begin{bmatrix} 1 & -\sqrt{3} \\ \sqrt{3} & 1 \\ 0 & 0 \end{bmatrix} \tag{2.18}$$

It's worth noting that the dq transformation utilized here is a conventional three-phase power application. The retrofit will convert the system's three-phase variables into an orthogonal coordinate system. The use of an orthogonal coordinate system allows the identification of state variables and the creation of state space equations for control purposes. For example, the secondary-side currents of transformer $I_{snd_{dq}}$ can be assumed as disturbances. Therefore, in the $dq - axis$ reference frame, the continuous time-domain state-space model of a three-phase grid-connected system equipped with an L-C filter can be developed and is given by;

$$\dot{\vec{x}}(t) = A\vec{x}(t) + B\vec{u}(t) + E\vec{d}(t) \tag{2.19}$$

where

$$A = \begin{bmatrix} 0_{2\times2} & (3C_f)^{-1}.I_{2\times2} \\ -(L_f)^{-1}.I_{2\times2} & 0_{2\times2} \end{bmatrix}, B = \begin{bmatrix} 0_{2\times2} \\ (L_f)^{-1}.I_{2\times2} \end{bmatrix}, C = \begin{bmatrix} -(3C_f)^{-1}.T_{ri_{dq}} \\ 0_{2\times3} \end{bmatrix}.$$

The states are $\dot{\vec{x}} = \begin{bmatrix} \vec{V}_{f_{qd}} & \vec{I}_{f_{qd}} \end{bmatrix}^T$, the control inputs $\vec{u} = \vec{V}_{pwm_{qd}}$, and disturbance $\vec{d} = \vec{I}_{snd_{qd}}$.

The system can be converted to a discrete time system with constant sampling time T_s to yield,

$$\dot{\vec{x}}(k+1) = A^*\vec{x}(k) + B^*\vec{u}(k) + E^*\vec{d}(k) \tag{2.20}$$

where

$$A^* = e^{A*T_s}, B^* = \int_0^{T_s} e^{A*T_s} B\, d\tau, C^* = \int_0^{T_s} e^{A*T_s} E\, d\tau.$$

2.5 Conclusion

The main objective of this chapter is to model and analyse the hybrid microgrid power system components. For the study, the first part, focusing on PV systems with dual stages, was selected. A single diode-based PV cell model based on quivalent circuit parameters was investigated, and a comparative analysis of the characteristics of the model with the manufacturer's data sheet characteristics was conducted after implementing the model in Simulink. The simulated I-V and P-V characteristics of the PV cell model are similar to those obtained from the manufacturer's data sheet. The model parameters are used in the second stage with the boost converter, where the $MPPT$ controller is used to track the power with respect to the desired output DC bus voltage. The $MPPT$ control was implanted with a 12 KW PV array model in Simulink. The results show that it is able to track the MPP with the $MPPT$ controller to achieve the desired DC bus voltage and supply the required power to the load.

The application focuses on the modeling and analysis of interconnected three-phase PWM inverters in the second part. To control the inverter's AC bus voltage, a standard voltage space vector PWM algorithm is presented. The Active Power Filter System's model state space is then investigated. It should be noted that the other important components of the hybrid microgrid power system (WTG and $BESS$) can be included to complete the system sizing.

The harmonics component elimination ability in the three-phase inverter working in over-modulation is welcome in all applications, especially in a hybrid microgrid systems where the objective of control design is to achieve low THD output voltage, fast transient response and asymptotic tracking of the reference output voltage under different loading conditions along with the minimization of the effect of the harmonic components. This crucial component in the energy saving will be examined in more depth in the next chapter.

Chapter 3

Power Quality Improvement in Microgrid Based on Robust Voltage Controller

3.1 Introduction

In this chapter a H_∞ control technique addresses the voltage regulation in a distributed generation (DG) system connected to a three-phase power converter under harmonics disturbances. The control technique combines a Discrete Sliding Mode Control ($DSMC$) in the inner current control and a Robust Servomechanism Problem (RSP) in the outer voltage control. Besides, a Fractional Order Proportional-Integral-Derivative ($FOPID$) controller synthesized with an automatic calibration of Adjustable Fractional Weights ($AFWs$) is formulated in this work to control voltage instead of RSP. The parameters of $FOPID$ are optimized by solving a multiobjective optimization problem based on the auto-calibration of the weighted-mixed sensitivity problem for robustness requirements between Nominal Performance (NP), Robust Stability (RS), and trade-off between them in a large range of frequencies. For better Robust Performance (RP), the calibrated parameters of $FOPID$ with $AFWs$ are compared with Fixed Integr Weights ($FIWs$). The simulation results validated in matlab/simulation are presented and analysed.

3.2 Power Quality Problem

In recent years, hybrid microgrids have become a trend in the development of microgrids that have a high capacity to accept a high number of $HRES$ components, require fewer numbers of converters, and have better economic and reliability. Nevertheless, the hybrid microgrid is a complex system and includes many nonlinear components, which will cause harmonics pollution and affect power quality [63]. The effects of harmonics are to increase the losses, damage the sensitive loads connected to the same bus, and overheat the components of the DG-connected inverter (transformer, shunt capacitor, etc.) [64]. High-order harmonics are also characterized by a significant impact on energy saving and, consequently, on the main function of EMS. In this sense, the use of Active Power Filter (APF) at the PWM output is also recommended in order to attenuate high frequency harmonics and thus contribute to better power quality. The interlinking converter is made up of an DC/AC inverter connected to a transformer by an APF, which constitutes the overall system known as a DG-connected inverter [40, 20]. In the literature, different control strategies (basic

and advanced) for DG-connected inverters have been proposed, which have a high-quality voltage with low THD [65]. However, the control strategies adopted to solve the problem are governed by the international $IEEE-519$ IEEEstandards, which impose limits on global THD depending on voltage output values, a vital aspect of power quality [66].

The most basic and commonly used control structure for DG-connected inverter including two loops: current control loop and secondary voltage and frequency control loop [38]. For a fixed model of the system, the performance of the controller is very high. However, the RS control need to the exact model with parametric uncertainty to achieve the both performances of low THD and fast dynamic response [67].

The H_∞ control technique has been widely applied to the stability analysis of the system of DG-connected inverters. Thus, the system performance can be greatly improved. Based on H_∞ control theory, RS problems in voltage control with consideration of uncertainty have been widely addressed in the literature, such as; Baghaee et al [68] presented a generalized H_∞ control. Hornik et al [69] introduced a H_∞ based on repetitive control to improve the tracking performance, low THD and protection from peak-current. Sedghi et al [70] proposed an H_∞ based control method to adjust the Microgrid MG under the uncertainties of the load changes. Grundling et al [71] a RS adaptive control for Uninterruptible Power Supplies (UPS) is developed. Sheela et al [72] applied H_∞ control to optimize voltage and frequency deviations after load changing. Lee et al [73] proposed RS analysis with H_∞ loop-shaping controller for UPS under perturbation. Mohamed [74] proposed an RS controller for a current source inverter based on H_∞ and μ-analysis techniques. Lam et al [75] developed a robust multi-variable H_∞ controller using Linear Matricial Inequality (LMI) technique and a μ-synthesis. Zhao et al [76] used the PSO technique to optimize the weighting function of the H_∞ controller. Pe et al [77] applies the H_∞ RS controller design method in the Matlab Robust Control Toolbox for high frequency resonant inverters but includes only load and external input voltage in the perturbation. Bevrani, et al [78] applies an LMI based μ-synthesis that shows more robustness compared to the conventional H_∞ control. Maniza, et al [67] proposed a linear matrix inequality approach to satisfy the Lyapunov stability criterion. Hamzeh, et al [79], extend the nonconvex optimization problem to the LMI conditions for voltage regulation, including the uncertainties of the system parameters. Raeispour, et al [36] and Gholami,

et al [80], a robust mixed H_2/H_∞ control strategies has been proposed based on multiobjective optimization. Marwali et al [62] it has developed an RSP controller based on an uncertain plant model. The outer loop RSC control system has been built to take into account the dynamics of the inner loop $DSMC$, ensuring the overall control system's RS. This technique, however, suffers from a high sensitivity to the load variations [81]. Even though the harmonics of the inverter output voltage have been significantly reduced, RS analysis is not shown [82]. In this context, the recorded control strategies cannot achieve the desired optimum trade-off between NP and RS when the model uncertainties are taken into account in the control parameters. Furthermore, based on core theories available in robust control techniques, a direct relationship between the singular values and sensitivities can be developed to provide information on the trade-off between NP and RS conditions, respectively [48, 83, 65]. Many academics have employed numerous alternative controller structures derived from fractional-order controllers in the same context [84, 85, 86].

These published works demonstrate the advantage of controllers synthesized by Adjustable Fractional Weights ($AFWs$) compared to those given by Fixed Integer Weights ($FIWs$) in terms of the strongly Robust Performance (RP) criterion.

To overcome this vulnerability, Sedraoui et al [87] use weighted-mixed sensitivity problem by proposing adjustable fractional weights. In general, the complementary sensitivity plot is obtained when the maximal singular values vanish as much as possible at high frequencies and approach unity at low frequencies. Amieur et al [86] proposed more analysis using a PSO optimization algorithm to guaranty optimal adjustable fractional weights. Accordingly, the RS voltage H_∞ controllers are generated utilizing both classical and structured H_∞ synthesis to solve a weighted-mixed sensitivity issue. So that, the voltage control of the DG-connected inverter can be formulated as solving the weighted-mixed sensitivity problem [65].

To the best of our knowledge, this research will use the typical $FOPID$ in the voltage control loop using H_∞ structures, which is inspired by the robustness of the fractional $FOPID$, a promising approach for solving the weighted-mixed sensitivity problem and ensure a good trade-off between NP and RS for the nominal and uncertainty plants, in which the adjustable weight is calibrated for getting the desired form of load voltage.

3.3 Control of Three-Phase Inverter System

To design a more accurate and robust control strategy, it is necessary to consider the detailed dynamic description of the ineterliking converter presented in chapter one. So, the block diagram of the proposed DC/AC converter control system in this work is shown in Figure 3.1.

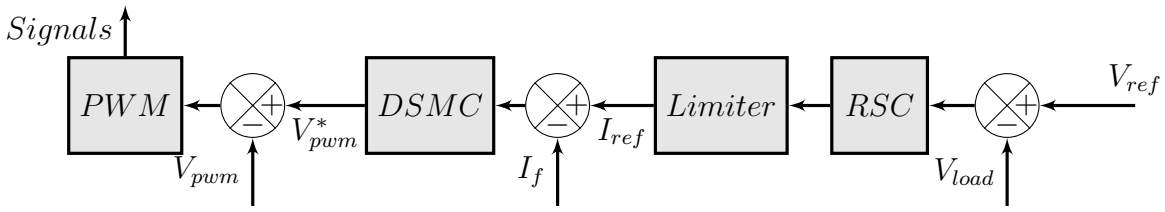

Figure 3.1: Block diagram of inverter controller

3.3.1 Design of Sliding Mode Current Controller

As shown in Figure 3.1, a dual-loop control structure is used, where the inner loop is for current control ($DSMC$) and the outer loop for voltage control based on RSP controller. The RSP is based on the solution of the servomechanism problem [60] where they combined between internal model principle [61] and the optimal control theory. The RSP is designed taking the dynamics of the $DSMC$ into account. The state space form of the dynamic equations is,

$$y(t) = Cx(t) \tag{3.1}$$

For designing the $DSMC$ controller the surface is chosen as $s(k) = Cx(k) - I_{ref_{qd}}(k)$, where $Cx(k) = I_{f_{qd}}(k)$, so that when sliding mode occurs, $s(k) = 0$ or $I_{f_{qd}}(k) = I_{ref_{qd}}(k)$. The control is given as,

$$V_{pwm_{qd}}(k) = (CB^*)^{-1}(I_{ref_{qd}} - CA^*x(k)) - CA^*d \tag{3.2}$$

The current command $I_{ref_{qd}}$ limited in magnitude. The errors between the inverter current com-

mands and the actual inverter commands,

$$e_{I_{qd}} = I_{ref_{qd}} - I_{f_{qd}} \tag{3.3}$$

The $DSMC$ will force these errors to zero by computing the necessary voltage commands given by 3.2.

3.3.2 Design of RSP Voltage Controller

To design the RSP voltage controller we need to consider a combination of the true plant in 3.1 and the $DSMC$ 3.3 as the "equivalent plant". Consider the block diagram in Figure 3.2, which depicts the closed-loop system of the RSP voltage control loop.

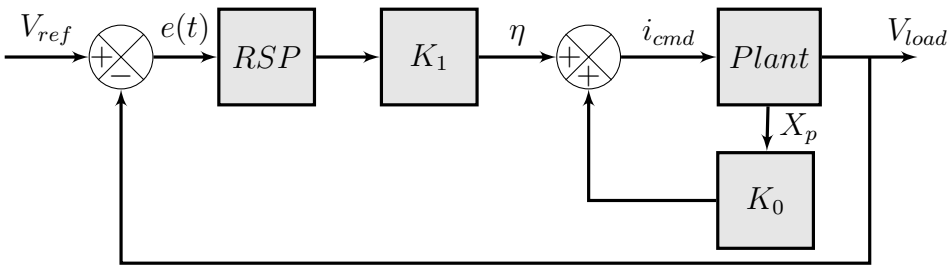

Figure 3.2: Block diagram of RSP controller

The controller is given by states feedback,

$$i_{cmd}(k) = K_0 x_p(k) + K_1 \eta(k) \tag{3.4}$$

where the states x_p the augmented true plant for $DSMC$;

$$\vec{x}_p(k+1) = A_p \vec{x}_p(k) + B_p \vec{i}_{cmd} \tag{3.5}$$

where

$A_p = A^* - B^*(CB^*)^{-1}(B^*C_1^* + E^*C_2^*)$; $\quad B_p = B^*(CB^*)^{-1}$;

$C_1^* = \begin{bmatrix} 1 & 0 & 0 & 0 & 0 \\ 0 & 1 & 0 & 0 & 0 \end{bmatrix}$; $\quad C_2^* = \begin{bmatrix} 0 & 0 & 0 & 1 & 0 \end{bmatrix}$.

The $RSP's$ theory is based on a solution to the robust servomechanism issue, which for linear systems can combine the internal model concept with optimal control theory. The discrete form of the continuous servo compensator is;

$$\vec{\eta}(k+1) = A_c\vec{\eta}(k) + B_c\vec{e}(k) \tag{3.6}$$

where, for each $i = 1, 3, \ldots, n$;

$Ac = diag\left[Ac_1, Ac_2, ..., Ac_n\right]$, $Bc = \left[Bc_1, Bc_2, ..., Bc_n\right]^T$, $Ac_i = \begin{bmatrix} 0 & 1 \\ -\omega_i^2 & 0 \end{bmatrix}$,

$Bc_i = \begin{bmatrix} 0 & 1 \end{bmatrix}^T$.

The states η_i from vector $\vec{\eta} = \left[\vec{\eta}_1, \vec{\eta}_2, ..., \vec{\eta}_n\right]^T$ represents implementation of the continuous transfer function $\frac{1}{s^2+\omega_i^2}$, where $\omega_i = 2\pi f_i$ represents the fundamental frequency to track and the harmonic frequencies to be eliminated. The gains $K = [\, K_0, K_1]$ are found by minimizing a certain linear quadratic cost function $J_\varepsilon$for the augmented "equivalent plant" and a discrete form of the servo-compensator:

$$\begin{bmatrix} x_p(k+1) \\ \eta(k+1) \end{bmatrix} = \begin{bmatrix} A_d & 0 \\ -B_c^*C & -A_c^* \end{bmatrix} \begin{bmatrix} x_p(k) \\ \eta(k) \end{bmatrix} + \begin{bmatrix} B_d \\ -B_c^*D \end{bmatrix} u(k) \tag{3.7}$$

The following is the optimization criterion for minimizing the discrete linear quadratic performance index;

$$J_\varepsilon = \sum_{k=0}^{\infty} \left(W_P x^* T_p(k) + W_S \eta_1^T(k)\eta_1(k) + W_H \sum_h \eta_h^T(k)\eta_h(k) + \varepsilon u^T(k)u(k) \right);\ (\varepsilon \geq 0) \tag{3.8}$$

where the constants W_P, W_S, and W_H are weighting scalars for plant states x_p, fundamental servo compensator states η_1 and harmonics servo compensator states η_h, respectively. Furthermore, the influence of different adjustable weights on the system's dynamic performance may be investigated in order to determine the optimum state.

3.3.3 Control System using Structured Singular Value

For the goal of stability analysis of the $MIMO$ linear system under structured perturbations, a structured singular value μ can be used. The problem is depicted in Figure 3.3, where M denotes a known stable $MIMO$ transfer function with W inputs and Z outputs and Δ a structured uncertainty matrix.

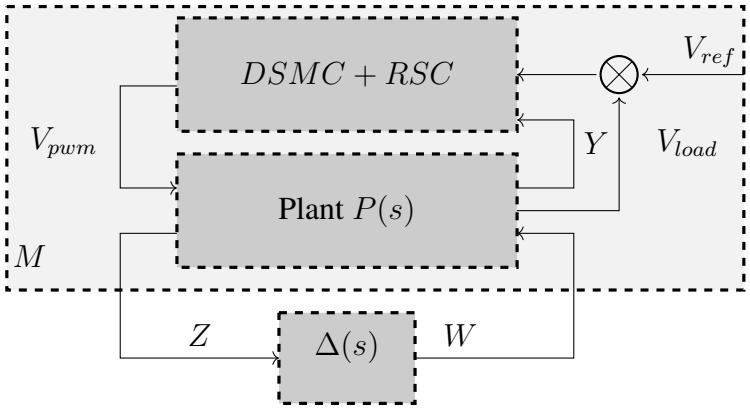

Figure 3.3: Uncertain closed-loop model.

The structured singular value of M with respect to the uncertainty set Δ is defined as,

$$\mu_{\Delta}(M) \triangleq \frac{1}{min\{\bar{\sigma}(\Delta_i) : \Delta_i \in (\Delta), det(I - M\Delta_i = 0)\}} \tag{3.9}$$

The generalized small-gain theorem provides RS results of the system using the structured singular value. It states that if nominal $M(s)$ is stable then the perturbed system $(I - M\Delta)^{-1}$ is stable for all stable Δ_i for which $\|\Delta_i\|_{\infty} \leq 1$ and only if $\mu_{\Delta}(M(j\omega)) < 1$ for all $\omega \in \mathbb{R}^{+}$.

The Linear fractional transformations (LFT) can be used to achieve the RS based on μ-framework analysis. For this to occur, we assume the following parameter changes in the structures of the system due to uncertainties and load variations: $P_{ind} = \{C_f, L_f, C_{load}, L_T, R_f, R_T, \lambda_{load}\}$. The above parameters can be represented as parametric output multiplicative uncertainties using lower $LFTs$ with the uncertain perturbation δ blocks separately can be precisely written as follows form;

$$P_{ind} = P_{ind_n}(1 + \tau_{P_{ind}}\delta_{P_{ind}}), |\delta_{P_{ind}}| < 1 \tag{3.10}$$

For each uncertain term, P_{ind_n} denotes the parameters' nominal value, $\tau_{P_{ind}}$ denotes the assigned tolerance, and $\delta_{P_{ind}}$ denotes the perturbation value. All perturbation sources are combined into a structured uncertainty diagonal matrix defined as $\Delta(s) = \{\delta_{C_f}, \delta_{L_f}, \delta_{C_{load}}, \delta_{L_T}, \delta_{R_f}, \delta_{R_T}, \delta_{\lambda_{load}}\}$.

By inspection, the nominal plant's state space model $P(s)$ is given as;

$$\begin{cases} \dot{X}(t) = AX_p(t) + B_pU(t) \\ Y(t) = C_pX(t) + D_pX(t) \end{cases} \tag{3.11}$$

where;

States: $X_p = \begin{bmatrix} V_f & I_f & V_{load} & I_{snd} & I_{load} \end{bmatrix}^T$;

Inputs: $U = \begin{bmatrix} V_{pwm} & W^T \end{bmatrix}^T$, where $W = \begin{bmatrix} w_{C_f}, w_{L_f}, w_{C_{load}}, w_{L_T}, w_{R_f}, w_{R_T}, w_{\lambda_{load}} \end{bmatrix}^T$;

Outputs: $Y = \begin{bmatrix} V_f & I_f & V_{load} & I_{load} & Z^T \end{bmatrix}^T$, where $Z = \begin{bmatrix} z_{C_f}, z_{L_f}, z_{C_{load}}, z_{L_T}, z_{R_f}, z_{R_T}, z_{\lambda_{load}} \end{bmatrix}^T$

$A_p = \begin{bmatrix} A_n \end{bmatrix}, B_p = \begin{bmatrix} B_n & B_{del} \end{bmatrix}, C_p = \begin{bmatrix} C_n \\ C_{del} \end{bmatrix}, D_p = \begin{bmatrix} D_n \\ D_{del} \end{bmatrix}$;

$$B_{del} = \begin{bmatrix} -\tau_{C_f} & 0 & 0 & 0 & 0 & 0 & 0 & 0 \\ 0 & -\tau_{L_f} & 0 & 0 & -\tau_{R_f}\frac{R_{fn}}{L_{fn}} & 0 & 0 & 0 \\ 0 & 0 & -\tau_{C_{load}} & 0 & 0 & 0 & -\tau_{\lambda_{load}}\frac{R_{load_n}}{C_{load_n}} & 0 \\ 0 & 0 & 0 & -\tau_{L_T} & -\tau_{R_T}\frac{R_{T_n}}{L_{T_n}} & 0 & 0 & 0 \\ 0 & 0 & 0 & 0 & 0 & 0 & 0 & \tau_{\lambda_{load}}M_{load_n} \end{bmatrix};$$

$$C_{del} = \begin{bmatrix} 0 & \frac{1}{C_{fn}} & 0 & -\frac{1}{C_{fn}} & 0 \\ -\frac{1}{L_{fn}} & -\frac{R_{fn}}{L_{fn}} & 0 & 0 & 0 \\ 0 & 0 & -\frac{R_{load_n}}{C_{load_n}} & \frac{1}{C_{load_n}} & -\frac{1}{C_{load_n}} \\ \frac{1}{L_{T_n}} & 0 & -\frac{1}{L_{T_n}} & -\frac{R_{T_n}}{L_{T_n}} & 0 \\ 0 & 1 & 0 & 0 & 0 \\ 0 & 0 & 0 & 1 & 0 \\ 0 & 0 & 1 & 0 & 0 \\ 0 & 0 & 1 & 0 & 0 \end{bmatrix};$$

$$D_{del} = \begin{bmatrix} 0 & -\tau_{C_f} & 0 & 0 & 0 & 0 & 0 & 0 & 0 \\ \frac{1}{L_{fn}} & 0 & -\tau_{L_f} & 0 & 0 & -\tau_{R_f}\frac{R_{fn}}{L_{fn}} & 0 & 0 & 0 \\ 0 & 0 & 0 & -\tau_{C_{load}} & 0 & 0 & -\tau_{\lambda_{load}}\frac{R_{load_n}}{C_{load_n}} & 0 & 0 \\ 0 & 0 & 0 & 0 & -\tau_{L_T} & -\tau_{R_T}\frac{R_{T_n}}{L_{T_n}} & 0 & 0 & 0 \\ 0 & 0 & 0 & 0 & 0 & 0 & 0 & 0 & 0 \\ 0 & 0 & 0 & 0 & 0 & 0 & 0 & 0 & 0 \\ 0 & 0 & 0 & 0 & 0 & 0 & 0 & 0 & 0 \\ 0 & 0 & 0 & 0 & 0 & 0 & 0 & 0 & 0 \end{bmatrix}.$$

The nominal open-loop plant (combination of $P(s)$ and $\Delta(s)$) and the closed controller loop make up the system M. $Matlab's\ sysic$ command has been utilized for this transformation. In order to speed up the response and improve the transient performance of the DG system, a local controller is developed by solving the H_∞ optimization problem. Therefore, to have a better voltage tracking, the gains associated with the outer-loop can be estimated by introducing adjustable fractional weights.

To investigate the performance in the presence of uncertainties, the μ-analysis and synthesis process is used to assess the robust performance of the H_∞ loop-shaping controller proposed in the next subsection.

3.4 Proposed Robust Performance Control Technique

The formulation of optimization problem can be posed under the general H_∞ control configuration. The robust control strategies have been proposed to determine the parameters of a robust controller. The optimal H_∞ control problem with this configuration consists a minimizing of iteration process the ratio γ between the energy of the vector Z and the energy of the vector W. The implementation of the iteration process with various well-known software packages such as [88, 89].

3.4.1 Fractional PID Control Design

Consider the block diagram in Figure 3.4, which depicts the proposed $FOPID$ controller in the RSP voltage control loop.

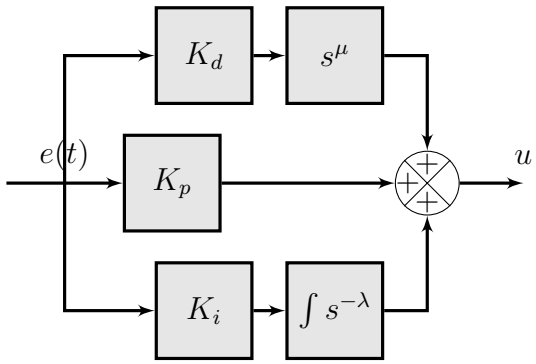

Figure 3.4: Structure of the proposed FOPID voltage controller

The transfer function model of the typical $FOPID$ controller in the continuous-time domain is given as;

$$K(s,x) = K_p + K_i s^{-\lambda} + K_d s^{\mu} \tag{3.12}$$

Yields the following design parameter vector $x = \Big[K_p, K_i, K_d, \lambda, \mu\Big]$ can be defined as a adjustable gains, referred to as proportional gain, integral gain, derivative gain, derivative and integral orders of s. In the design procedure, each component from the vector for the $FOPID$ controller is constrained by boundary or saturation limits included in the search space χ;

$$\chi = \begin{cases} K_{(p,i,d)_{min}} \leq K_{(p,i,d)} \leq K_{(p,i,d)_{max}} \\ \lambda_{min} \leq \lambda \leq \lambda_{max} \\ \mu_{min} \leq \mu \leq \mu_{max} \end{cases} \tag{3.13}$$

3.4.2 Weighted-Mixed Sensitivity Problem Including FIWs

The NP-RS trade-off must be reached with a good, secure margin. The current situation of the equation 3.9 appears to be key to a better understanding of the RS mean. Therefore, providing a good RS requires limiting the evolution of the maximum singular values of the complementary sensitivity function, i.e., $\bar{\sigma}(T_0(\omega, x))$ across the whole frequency range $\omega_{min} \leq \omega \leq \omega_{max}$. This is accomplished by finding a sufficient weighting function $W_{T_0}(s)$ such that equation 3.9's RS

condition is reformulated as follows:

$$\|W_{T_0}(s)T_0(s,x)\|_\infty \leq 1 \tag{3.14}$$

where the complementary sensitivity function $T_0(s,x)$, defined as;

$$T_0(s,x) = M\Delta[\,I + M\Delta]^{\,-1} \tag{3.15}$$

where present the transfer function between the reference control input V_{ref} and the output V_{load}.

Similarly, providing a good NP requires limiting the evolution of the maximum singular values of the direct sensitivity function, i.e., $\bar{\sigma}(S_0(\omega,x))$. This is accomplished by finding a sufficient weighting function $W_{S_0}(s)$ that always satisfies the following condition;

$$\|W_{S_0}(s)S_0(s,x)\|_\infty \leq 1 \tag{3.16}$$

Also, the direct sensitivity function $S_0(s,x)$, defined as;

$$S_0(s,x) = [\,I + M\Delta]^{\,-1} \tag{3.17}$$

where presents the transfer function between the control error e and the output V_{load}. also presents the transfer function between the disturbance input delta and the output.

The RS and NP conditions in the inequalities may be translated into upper bounds $W_{T_0}(s)$ and $W_{S_0}(s)$, yielding;

$$\begin{cases} \|S_0(s,x)\|_\infty \leq \|W_{S_0}(s)\|_\infty^{-1} \\ \|T_0(s,x)\|_\infty \leq \|W_{T_0}(s)\|_\infty^{-1} \end{cases} \tag{3.18}$$

In general, in order to secure the suitable RS, complimentary sensitivity transfer matrix $T(s,x)$ has been used. For acquiring the NP the direct sensitivity transfer matrix $S(s,x)$, has been used. This characteristic can be obtained by defining a performance weighting matrices to shape the sensitivity function. In the mixed sensitivity problem, both conditions are combined in order to

determine the robust performance (RP) condition [90, 87, 84, 83];

$$\|J_0(s,x)\|_\infty = \left\| \begin{matrix} W_{S_0}(s)S_0(s,x) \\ W_{T_0}(s)T_0(s,x) \end{matrix} \right\|_\infty \leq \gamma_0 \tag{3.19}$$

According to inequality 3.19, the requested control system should attenuate the very worst case of the limit showing up either from the plot of $\bar{\sigma}(W_{S_0}(s)S_0(s,x))$ or $\bar{\sigma}(W_{T_0}(s)T_0(s,x))$. Whatsoever frequencies, this must be lowered to less than the pre-specified attenuation level $\gamma_0 \leq 1$, i.e.;

$$\underbrace{\max\left\{\overbrace{\max_\omega \bar{\sigma}(W_{S_0}(j\omega)S_0(j\omega,x))}^{NP}, \overbrace{\max_\omega \bar{\sigma}(W_{T_0}(j\omega)T_0(j\omega,x))}^{RS}\right\} \leq 1}_{RP} \tag{3.20}$$

The optimal H_∞ control problem can be formulated as a H_∞ suboptimal control problem [91, 87, 83], which leads to the following min–max optimization problem, which satisfies the inequality 3.19;

$$\max_{x\in\chi} \left\| \begin{matrix} W_{S_0}(s)S_0(s,x) \\ W_{T_0}(s)T_0(s,x) \end{matrix} \right\|_\infty \Leftrightarrow \min_{x\in\chi} \left(\max_\omega \left(\bar{\sigma} \begin{bmatrix} W_{S_0}(j\omega)S_0(j\omega,x) \\ W_{T_0}(j\omega)T_0(j\omega,x) \end{bmatrix} \right) \right) \tag{3.21}$$

The conventional and structured H_∞ techniques available in $Matlab$, such as $HinfLMI$ and $Hinfstruct$, can be used to synthesize the robust voltage H_∞ controller and solve problem 3.21.

The terms $W_{S_0}(s)$ and $W_{T_0}(s)$ are the tracking performance and stability weighting matrices, respectively. The very general guidelines for weighting matrices choices were proposed in [91, 90, 92], although they are not strictly used in this study;

$$W_{S_0}(s,x) = \left(\frac{\frac{s}{\sqrt{M_{S_0}}} + \omega_{B_0^*}}{s + \omega_{B_0^*} A_{S_0}} \right) I_{n_0 \times n_0}, \qquad W_{T_0}(s,x) = \left(\frac{\frac{s}{\omega_{BT_0^*}} + \frac{1}{\sqrt{M_{T_0}}}}{\frac{A_{T_0} s}{\omega_{BT_0^*}} + 1} \right) I_{m_0 \times m_0} \tag{3.22}$$

Each weight vector can be parameterized in terms of the parameter vector $x_0 = \left[M_{S_0}, A_{S_0}, \omega_{B_0^*}, M_{T_0}, A_{T_0}, \omega_{BT_0^*}\right]$.

It really should be noted that in the mixed-sensitivity scenario, choosing suitable $FIWs$ in the design of a $FOPID$ voltage regulator can be complicated, particularly as the number of prescribed frequency specifications increases. To overcome this problem, the use of $AFWs$ instead of $FIWs$

is required to improve the RS-NP trade-off.

3.4.3 Weighted-Mixed Sensitivity Problem Including AFWs

Although there are simple rules for selecting the weighting functions used in controller synthesis, these can be used to compare existing (classical) designs. But, compared with conventional $FIWs$ and their NP and RS margins, the $AFWs$ with a systematic selection present a good trade-off. The idea allows for formulating an auto-calibration of $FIWs$' parameters, which is proposed as a new weighted mixed sensitivity problem [87]. In weighted-mixed sensitivity problem design, the initial selection of $AFWs$ to fulfill the RS-NP trade-off is critical in shaping the performance and robustness characteristics of systems built. Generally, the required stability weight's transfer functions take the forms [91, 44, 65]:

$$W_S(s,x) = \left(\frac{\frac{s^n}{\sqrt{M_S}} + \omega_B^*}{s^n + \omega_B^* A_S} \right) I_{n\times n}, \qquad W_T(s,x) = \left(\frac{\frac{s^m}{\omega_{BT}^*} + \frac{1}{\sqrt{M_T}}}{\frac{A_T s^m}{\omega_{BT}^*} + 1} \right) I_{m\times m} \tag{3.23}$$

Which are given by transfer functions as a general class of n^{th} and m^{th}-order nonlinear systems; where M_S and M_T are high frequency gains, A_S and A_T are low frequency gains and ω_B^* and ω_{BT}^* determine crossover frequency. Next, n and m denote the order of a function should be kept as low as possible [91]. In this case, $W_S(s,x)$ is the performance weighting function that is specified for the disturbance elimination to restrict the magnitude of the sensitivity function and $W_T(s,x)$ the robustness weighting function is identified for the uncertainty in the plant to limit the magnitude of the complementary sensitivity function. This approach, known as loop shaping, is frequently used for choosing the weight functions for controller synthesis. From inequalities 3.24, the appropriate $W_S(s,x)$ and $W_T(s,x)$ of $AFWs$ can be expressed in terms of the new parameters using the weight parameter vector $x_1 = \left[M_S, A_S, n, \omega_B^*, M_T, A_T, m, \omega_{BT}^* \right]$.

We now concentrate on selecting these parameters according to some guidelines available in the literature corresponding to adequate $AFWs$. With special attention to the effects of detailed

implementation guidance, these rules-based elements can be summarized as follows;

$$\chi_m = \begin{cases} \delta_{M_S} M_{S_0} \leq M_S \leq M_{S_0} & M_{S_0} \in [\,1.5, 2]\,, \;\; \delta_{M_S} \in]\,0, 1[\\ \delta_{M_T} M_{T_0} \leq M_T \leq M_{T_0} & M_{T_0} \in [\,1.5, 2]\,, \;\; \delta_{M_T} \in]\,0, 1[\\ \omega_{B_0^*} \leq \omega_B^* \leq \delta_{B_0^*} \omega_{B_0^*} & \delta_{B_0^*} \in]\,1, 2[\\ \delta_{BT_0^*} \omega_{BT_0^*} \leq \omega_{BT}^* \leq \omega_{BT_0^*} & \delta_{BT_0^*} \in]\,0, 1[\\ n_0 \leq n \leq \delta_n n_0, & \delta_n \in]\,1, 2[\\ m_0 \leq m \leq \delta_m m_0, & \delta_n \in]\,1, 2[\\ \delta_{A_S} A_{S_0} \leq A_S \leq A_{S_0}, & \delta_{A_S} \in]\,0, 1[\\ \delta_{A_T} A_{T_0} \leq A_T \leq A_{T_0}, & \delta_{A_T} \in]\,0, 1[\end{cases} \tag{3.24}$$

Indeed, minimize the values of M_S and M_T as much as possible to restrict the singular values of the required direct and complementary sensitivities. To improve disturbance attenuation, the basic guideline is to transfer the bandwidth ω_B^* to the high-frequency region as much as possible. Inversely, ω_{BT}^* should be transferred to the low frequency region as much as possible to improve sensor noise rejection. However, raising ω_B^* beyond what is required generates an unacceptable overshoot. Inversely, reducing ω_{BT}^* results in bad tracking performance. Also, raising the fractional-order m as much as possible increases the NP margin. However, raising m with respect to n is required to avoid the high-frequency effect, which violates the RS requirement. Finally, the parameters A_S and A_T must be selected as close to zero as possible, where setting $A_S = A_T = 0$ is the best scenario [91, 93, 83, 94]. So far, there is no direct technique to set values for these parameters, only to keep determining them in a specific field. In most cases, using an optimisation method to determine the values for the system is the only available method.

To evaluate the RP design procedure, the previous free design parameters are represented by two vectors that can be augmented into one design vector x_g which parametrizes the overall control process;

$$x_g = [\overbrace{K_p, K_i, K_d, \lambda, \mu}^{x}, \overbrace{M_S, A_S, n, \omega_B^*, M_T, A_T, m, \omega_{BT}^*}^{x_1}] \tag{3.25}$$

To guarantee robust performance, the new design vector x_g should provide a robust $FOPID$ voltage controller as well as optimal $AFWs$. However, the problem is formulated based on $fminimax$ function in Matlab's optimization toolbox, with equation 3.21 defining the fitness function and the search spaces defined by χ in 3.13 and χ_m in 3.24. Indeed, $fminimax$ is adopted to search for the optimal design vector x_{best} that represents the optimal solution.

3.5 Control Development and Simulation Results Discussions

The proposed robustification approach is simulated using two steps. The first is constructed using typical integer weights, and their RS, NP, and RP robustness margins are then improved by automatic calibration of adjustable fractional weights. The first step of simulation permits defining frequency space and different rules for formulation of fractional weighted-mixed sensitivity problem. Subsequently, for improving the RP margins, an optimization algorithm is used to enhance the NP-RS trade-off. Performance of the proposed steps is evaluated using simulation in $MATLAB/Simulink$ environment.

Table 3.1: Parameters of DC/AC inverter.

Parameters	Values
DG voltage V_{dc}	540V
AC Output voltage V_{load}	208V(LL), 120V(LN)
Filter capacitance C_f	540μF
Filter inductance L_f	300 μH
Transformer inductance L_T	48 μH
Transformer resistance R_T	0.02 Ohm
Transformer ratio	245 :208 V
System frequency f	50 Hz
Load side capacitors C_{load}	90 μF

The DC input voltage was set to $540V$ to reach the typical RMS three-phase AC load voltage of 120 V. The system fundamental frequency of the output voltage is $f = 50Hz$, and the frequency

of the PWM switching signal is $fs = \frac{1}{T_s}$ which is set to be $5.4KHz$, as is the discrete-time control frequency. These and the other selected parameters are presented in table 3.1.

For the robust voltage H_∞ controller, the system provided through classical H_∞ based-$LMIs$ function MATLAB software. The $fminimax$ search space of $FOPID$ controller optimal parameters is chosen as,

$$\begin{cases} 0.001 \leq K_{p,i,d} \leq 10 \\ 0.001 \leq \lambda \leq 0.99 \\ 0.001 \leq \mu \leq 0.99 \end{cases} \tag{3.26}$$

To make the design much simpler and the stability evaluation easier, the $FIWs$ transfer functions for stabilising the compensator are selected based on the work [95] with some adjustment relative;

$$W_{S_0}(s, x_0) = \frac{1}{\sqrt{10}}\left(\frac{s+1}{s+10^{-7}}\right), \qquad W_{T_0}(s, x_0) = 10^7\left(\frac{s+\sqrt{10}10^4}{s+10^13}\right) \tag{3.27}$$

where the initial parameters of vector x_0 are: $M_{S_0} = 10$, $\omega_{B_0^*} = 1$, $A_{S_0} = 10^{-7}$, $n_0 = 1$ for transfer function of the NP weight and $M_{T_0} = 10$, $\omega_{BT_0^*} = 10^5$, $A_{T_0} = 10^{-8}$, $m_0 = 1$ for transfer function of the RS weight. Thus, for the closed-loop system performance specifications, we select the search space of $FIWs$ parameters as follows;

$$\chi_m = \begin{cases} 0.9M_{S_0} \leq M_S \leq M_{S_0} & M_{S_0} \in [\,1.5, 2]\,, \;\; \delta_{M_S} \in]\,0, 1[\\ 0.9M_{T_0} \leq M_T \leq M_{T_0} & M_{T_0} \in [\,1.5, 2]\,, \;\; \delta_{M_T} \in]\,0, 1[\\ \omega_{B_0^*} \leq \omega_B^* \leq 1.5\omega_{B_0^*} & \delta_{B_0^*} \in]\,1, 2[\\ 0.5\omega_{BT_0^*} \leq \omega_{BT}^* \leq \omega_{BT_0^*} & \delta_{BT_0^*} \in]\,0, 1[\\ n_0 \leq n \leq 2n_0, & \delta_n \in]\,1, 2[\\ m_0 \leq m \leq 2m_0, & \delta_n \in]\,1, 2[\\ 0.01A_{S_0} \leq A_S \leq A_{S_0}, & \delta_{A_S} \in]\,0, 1[\\ 0.01A_{T_0} \leq A_T \leq A_{T_0}, & \delta_{A_T} \in]\,0, 1[\end{cases} \tag{3.28}$$

To get one of the optimal solutions that is the best trade-off between the conflicting max-min ob-

jective functions, the $MATLAB^{®}$ $fminimax$ function is required. The optimal locations obtained by this algorithm depend on the initial population, where the setting of a good initial population could produce the best fitness.

Firstly, the design of the $FOPID$ controller is tuned using the fminimax solver without considering the $FIWs$ constraints. Due to the $MATLAB$ deterministic structure of the $fminimax$ solver, the optimization process is repeated 23 times with different initial populations. The optimal solution of the $fminimax$ optimization problem is depicted in the vector;

$$x_0^{best} = [1.8569, 3.1942, 2.9501, 0.5412, 0.5313] \tag{3.29}$$

Secondly, the parameters for each desired FIW weight are specified according to the recommendations provided above, as shown by inequalities 3.28. Therefore, using the $fminimax$ solver, to select these weights automatically is linked to determining the ideal parameters of the robust $FOPID$ voltage controller, where the resulting $FOPID$ transfer function is given as;

$$K(s, x_1^{best}) = 0.001 + \frac{9.0219}{s^{0.98982}} + 0.0011 s^{0.4989} \tag{3.30}$$

where

$$\begin{cases} 0.01 \leq K_p = 0.001 \leq 10 \\ 0.01 \leq K_i = 9.0219 \leq 10 \\ 0.01 \leq K_d = 0.0011 \leq 10 \\ 0.001 \leq \lambda = 0.98982 \leq 0.99 \\ 0.001 \leq \mu = 0.4989 \leq 0.99 \end{cases}$$

Furthermore, the given optimal solution allows determining the performance and sensitivity weighting functions respectively as follow;

$$W_s(s, x_1^{best}) = \left(\frac{\frac{s}{\sqrt{10}} + 1}{s + 1 * 10^{(-7)}} \right), W_T(s, x_1^{best}) = \left(\frac{\frac{s}{10^5} + \frac{1}{\sqrt{10}}}{\frac{10^{(-8)} s}{10^5} + 1} \right) \tag{3.31}$$

where $x_g^{best} = [\, 0.001, 9.0219, 0.0011, 0.98982, 0.4989, 10, 10^{(-7)}, 1, 10, 10^{(-8)}, 10^5]$.

This phase allows us to get the most out of the effect of $FIWs$ limitations on the optimal $FOPID$ controller and $fminimax$ function solution. Finally, the $AFWs$ design problem is formulated in terms of stabilizing the $FOPID$ controller with the fractional-order set of following weights;

$$W_s(s, x_1^{best}) = \left(\frac{\frac{s^{1.8}}{\sqrt{1.120}}+1}{s^{1.8}+1*10^{(-7)}} \right), W_T(s, x_1^{best}) = \left(\frac{\frac{s^{1.0001}}{10^{(-8)}}+\frac{1}{\sqrt{1.25}}}{\frac{10^5 s^{1.0001}}{10^{(-8)}}+1} \right) \tag{3.32}$$

where $x_g^{best} = [\,0.001, 9.0219, 0.0011, 0.98982, 0.4989, 1.20, 10^{(-7)}, 1.8, 1, 1.25, 10^{(-8)}, 1, 10^5]\,.$

As a result, the ideal parameters of the robust $FOPID$ voltage controller must match the NP-RS trade-off as closely as possible while maintaining a good secure margin. This all previous components of the resulting solutions confirms the well-chosen $fminimax$ optimization procedure with no relaxation of lower and upper bounds.

3.5.1 Frequency-domain analysis

In this work, the commonly used threshold for the maximum singular value was determined using the log-log plot of the complementary sensitivity functions. The maximal singular values plots of the complementary sensitivity functions at high and low frequencies of the closed-loop system are depicted in Figure 3.5.

Four loglog scale plotted cases with their inverse function plots present a comparison controller of an H_∞ μ-sythetesis, $FOPID$ without $FIWs$ constraints, $FOPID$ with calibrated $FIWs$ parameters, and $FOPID$ with calibrated $AFWs$. The inverse functions of the initial $FIWs$, calibrated $FIWs$, and calibrated $AFWs$ are plotted in dashed lines. The frequency plots produced by the inverse of initial and optimal performance weights are compared to those produced by the inverse of initial and optimal performance weights.

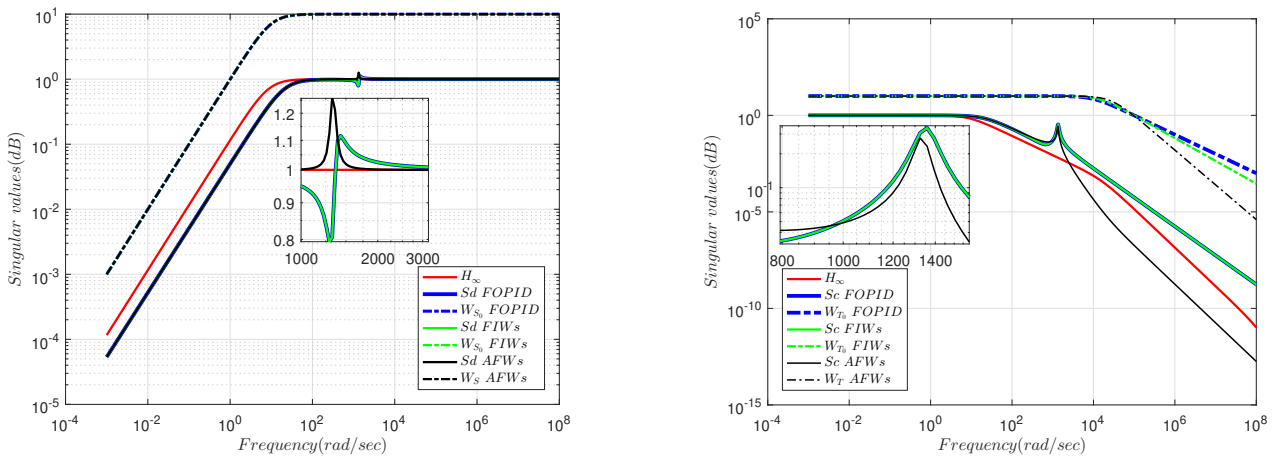

(a) $NP\ margin$ (b) $RS\ margin$

Figure 3.5: Tracking dynamic of the voltage given by the robustified fractional controller.

Figure 3.5a show that in the low frequency range ($\omega = 10^{-4} rad/s$), the better NP margin is obtained when the maximum singular values of the direct sensitivity matrix are small as possible. Also, results shows that all singular values are bounded by $W_{S_0}^{-1}(s)$. Then, the offered robust control can satisfy the NP conditions. In addition, the control scheme offers a better RS margin in the high frequency range ($\omega = 10^{8} rad/s$) as shown in Figure 3.5b, where the complementary sensitivity matrix's of the maximal singular values has the steepest slope compared to slope of the initial conditions. Also, results shows that all singular values are bounded by $W_{T_0}^{-1}(s)$. As shown in the figures, the $FOPID$ controls operate better when the calibrated parameters are violated, with their effect visible in the zoom zones. The closed-loop control's bandwidth can be used to evaluate its responsiveness; at low frequencies, the gain of the three initial, calibrated $FIWs$ and calibrated $AFWs$ falls similarly better than the gain of the H_∞ control. On the other hand, there is a better fall in the high frequency of $AFWs$ compared to the calibrated $FIWs$. All the results demonstrate that the proposed $FOPID$ controller with the AFW structure can successfully provide greater robustness qualities and achieve the $NP-RS$ trade-off. To substantiate the aforementioned results, the temporal domain simulation of the closed-loop system will be presented in the following step.

3.5.2 Time-domain analysis

The desired source voltage always contains harmonics. For the three-phases PWM inverter system wish desired to eliminate third, fifth, and seventh harmonics. Figure 3.6 shows both load and rebustified voltages. As illustrated, the voltage signals converge to their nominal values. The figure shows that the voltage waveforms are only marginally affected by the load disturbance and revert to a steady state in a relatively short time. So that, the better tracking properties are ensured by the adjustable fractional weights controller, which is characterized by the fast attenuation dynamic of the harmonic voltage disturbances as shown in Figure 3.8.

Therefore, Figure 3.7 show the obtained output current responses of the closed-loop system given by the RSP and robust adjustable fractional weights controllers. It can be observed that all controllers are coverging together properly.

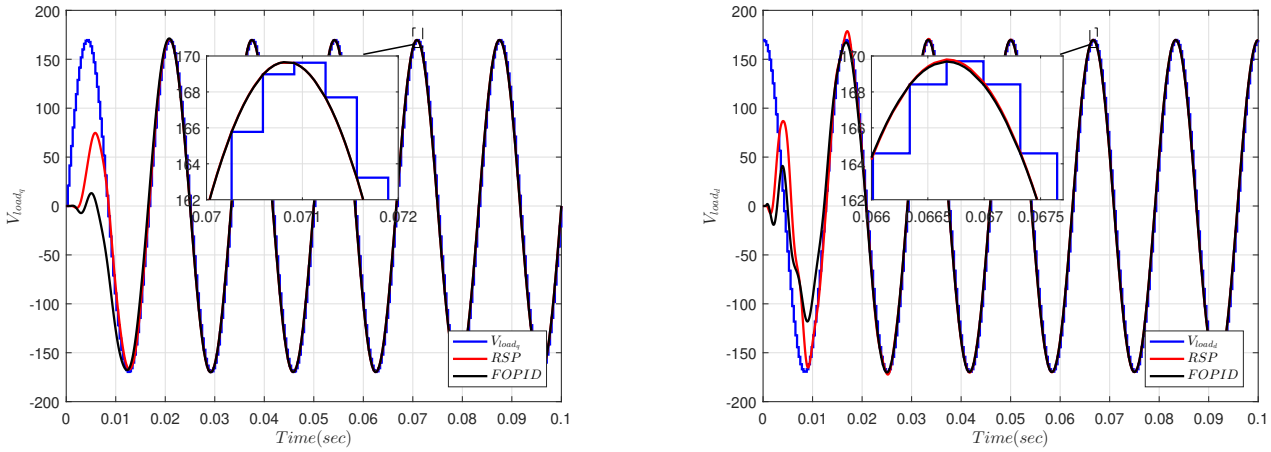

(a) $q-axis$ (b) $d-axis$

Figure 3.6: Tracking dynamic of the voltage given by the robustified fractional controller.

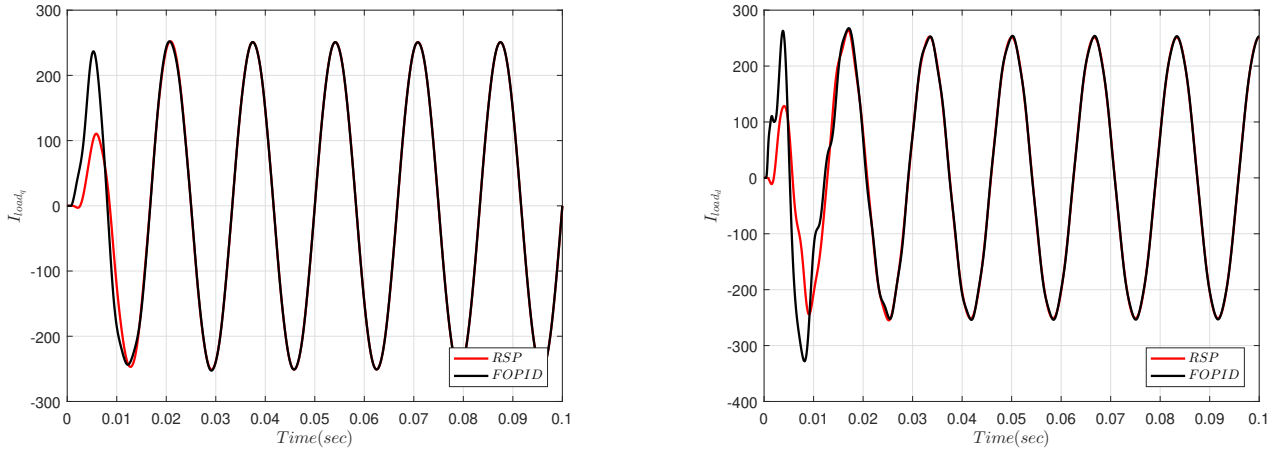

(a) $q-axis$ (b) $d-axis$

Figure 3.7: The output current given by the robustified fractional controller.

The above-mentioned requirements are satisfied by the calibrated parameters of $AFWs$, where the controller seems to be more sensitive to process perturbations. Steady state RMS output voltages and $THDs$ have been presented in Figure 3.8. The proposed method achieves approximately zero steady state error and a THD of less than 0.5%. It can be observed that the RMS reveal about $2V$ deviations on each transient state.

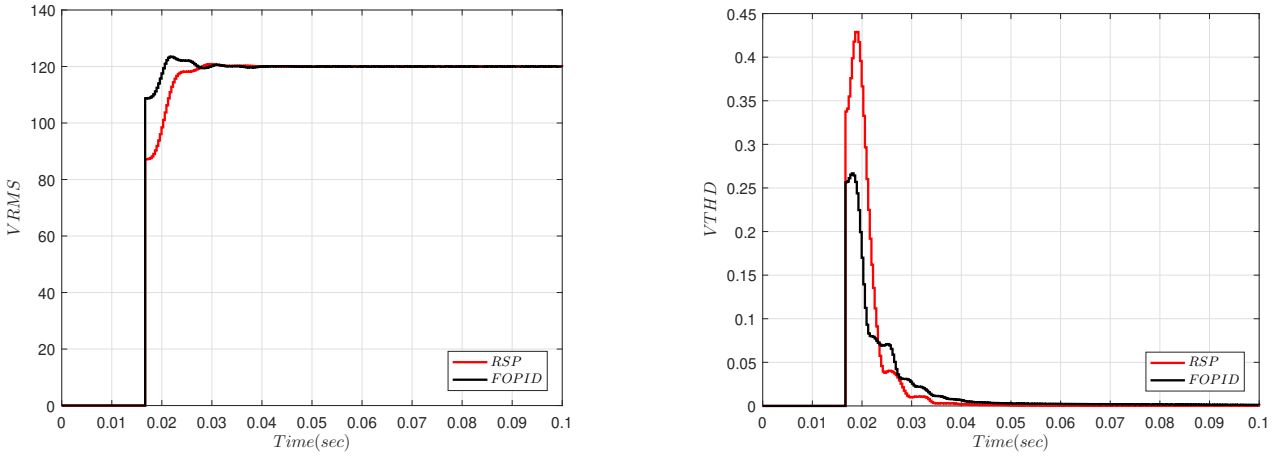

(a) $VRMS$ (b) $VTHD$

Figure 3.8: Comparison of RMS and THD values of the load voltages.

The transient response of the control has been demonstrated and the harmonic distortion of DG voltage can be significantly suppressed under the adjustable fractional weights control mode which made the active power-sharing has acceptable accuracy and improves power quality of the DG unit as depicted in Figure 3.9. Ultimately, we can conclude that the proposed controller performs

successfully to provide the both robust voltage control and active power sharing of three-phases PWM inverter.

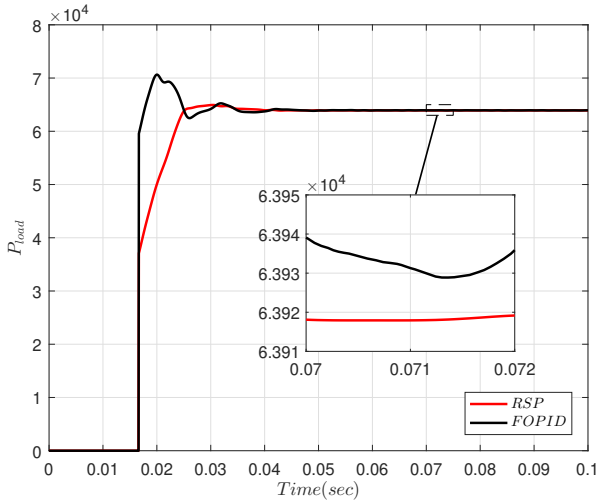

Figure 3.9: Comparison results for real load powers.

Finally, the robustified $FOPID$ case is simulated in the time domain with new $AFWs$ under various load scenarios, including both no load and overload. In this analysis, nonlinear load is not taken into account. In this simulation, three cases were done for loads; while the first case was simulated under 500% of the resistive nominal load, the second was simulated under full load or steady state, and the third was done without load.

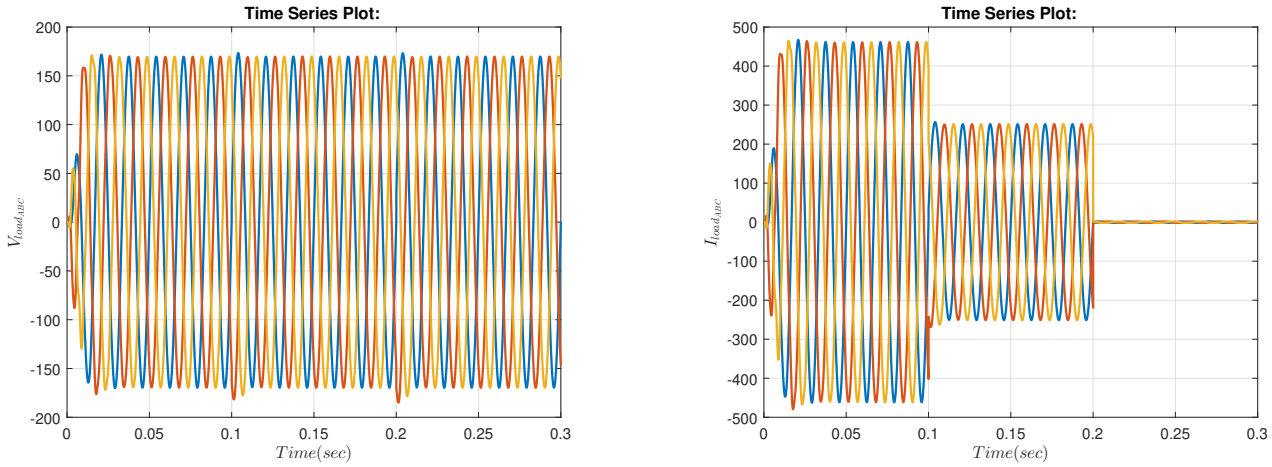

(a) $V_{load_{ABC}}$ (b) $I_{load_{ABC}}$

Figure 3.10: Transient response of voltage and current under load change from 500% (t=0s) 100% (t=0.1s) to 0% (t=0.2).

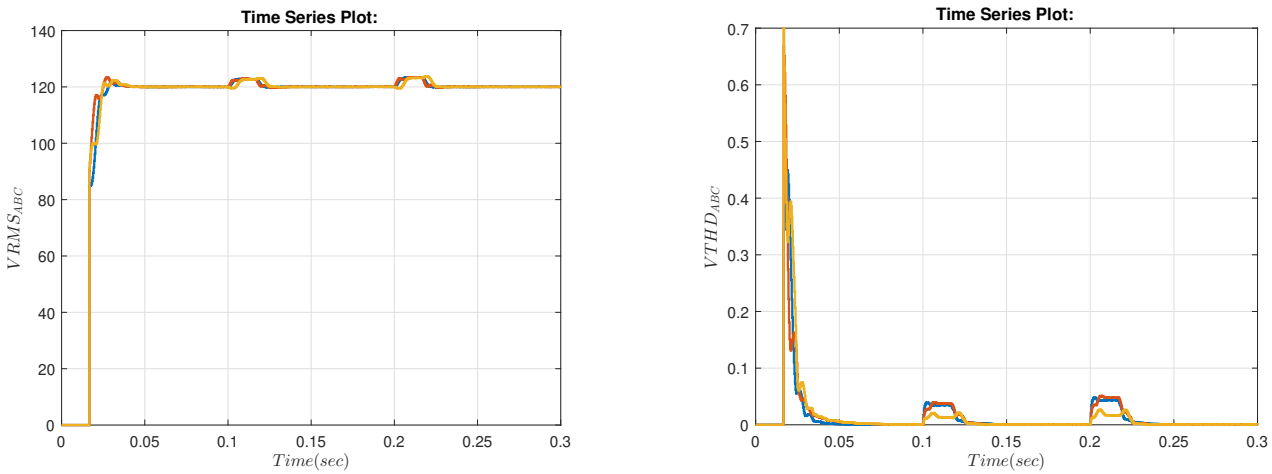

(a) $VRMS$ (b) $VTHD$

Figure 3.11: RMS and THD values of the load voltages under load change from 500% (t=0s) 100% (t=0.1s) to 0% (t=0.2).

Figure 3.10 shows the transient response of voltage and current to a load change from 500% at t = 0s to 100% at t = 0.1s to no load at t = 0.2s. Figure 3.11 depicts the RMS and THD values of the three phases load voltages under the same previous conditions.

The figures show that the discrete-time voltage waveforms are only slightly affected by the load variation and are restored to steady state in a very short period of time; that is, the waveform dents last for only a few msec, and the RMS values reveal roughly 3% deviations on each transient, which lasts for about 0.025 sec. The analysis of the transient response under sudden changes in the load condition can also be verified by looking at the load current plot where the currents change with this sudden load changes. In each case, the inverter can deliver the full load with a maximum percentage voltage that is always less than 5%. As a result, $FOPID$ controllers provide a satisfactory quick transient response with low THD, and better power quality.

3.6 Conclusion

In this chapter, a robust voltage control scheme for a three-phase PWM inverter was proposed to handle the uncertainties and mitigate the impact of a voltage disturbance. This study was started by designing the theoretical concepts of a discrete sliding mode controller for inner current control, including the mathematical model of the inverter. As a comparison controller, an H_∞ μ-sythetesis controller based on the Robust Servomechanism Problem procedure was designed in the second step for the outer loop load voltage regulation. In addition, this study was followed by designing the proposed robust H_∞ voltage controller employing the innovative structure of the $FOPID$ controller with $AFWs$ approaches. The controller parameters are formulated as a weighted-mixed sensitivity problem optimized through Matlab's $fminimax$ constrained function. The frequency-domain responses of the robustness settings NP and RS, as well as the trade-off between them, were confirmed in this study, with the RP obtained from $AFWs$ outperforming randomly chosen $FIWs$ and the H_∞ controller. Moreover, the performance of the calibrated parameters of the $FOPID$ controller was evaluated under harmonic voltage disturbances based on temporal-domain simulations in the MATLAB/Simulink environment and comparison with the conventional Servomechanism control technique. Finally, as perceived by the results, the load voltage maintained its stability when faced with disturbances. Compared with the case of a conventional Servomechanism control configuration, significant THD reduction of the inverter output voltage is achieved by introducing calibrated $AFWs$ into the $FPOID$ controller.

Chapter 4

Power Management in Microgrid Based on Fractional Fuzzy Controller

4.1 Introduction

Controlling the balance between consumption and supply is a substantial problem for hybrid microgrid systems, especially for hybrid renewable energy systems ($HRES$), due to the high inbalance in the generation energy sources, uncertainty of weather and demand circumstances. However, a comprehensive overview of $HRES$ with an emphasis on performance for a wide range of power system operating conditions is needed. Due to the increasing necessity to update traditional control strategies, sophisticated PMC algorithms have been developed to maximize the power conversion from $HRES$ components. Therefore, when PMC input parameters are highly variable and unstable, a fuzzy logic controller can be used to analyze the dynamics of the $HRES$ system and verify the PMC purposes. In this chapter, an improved PMC for renewable hybrid PV/Wind system with battery storage based on a closed-loop fractional fuzzy controller is presented. Under this design, the parameters of a Proportional, Fractional Derivative and Integral ($PD^{\alpha} + I$) controller are considered as decision variables of the fuzzy logic controller. To calibrate the $PD^{\alpha} + I$ parameters, a suggested optimization algorithm called Social Spider Optimization (SSO) is used. Concurrently, the work was validated under Matlab/Simulink and the results were compared with conventional Particle Swarm Optimization (PSO) and Genetic Algorithm (GA) methods. It has the ability to improve the $HRES$ system's dynamic response, validate PMC purposes and increase the overall system's efficiency.

4.1.1 Power Management Problem

In the last decades, great attention has been focused on the $HRES$ and due to the several advantages of hybrid PV/Wind systems. The continuous energy, whatever the variations of the load and of the weather conditions, allows satisfying the load side and the possibility to keep the batteries charged. The use of intelligent manners requires the ability to solve PMC problems involving various architecture applications focused on intelligent PMC [96]. The aim is to develop more efficient, controllable and priceless smart grids to achieve better reliability between demand side and supply [97]. To provide acceptable power balance, it is necessary to maintain an adequate

controller at predetermined conditions and/or load variations [98]. In the $HRES$ systems, the proper PMC has been designed to maintain generation–consumption equilibrium as well as ensuring uncertainties and transient stability is unavoidable [99]. In general, all the $PMCs$ studies are always based on power balance. In the literature, there are many studies and control techniques have been proposed related to PMC with basic and advanced control strategies [100, 101]. For conventional $PMCs$, applyed techniques including H_∞ [102], Ziegler–Nichols [103], linear programming [104, 105], microcontroller with $FPGA$ [106], secondary control approach [107], Reformed Electric System Cascade Analysis ($RESCA$) [108], have been investigated to this end. Therefore, significant efforts were made in applying several optimisation algorithms to support power stability against system uncertainties, e.g., Particle Swarm Algorithmic (PSO) [109, 110], Genetic Algorithmic Technique (GA) [111], Bat Algorithm (BA) [112], Crow Search Algorithm (CSA) [113, 114], Cuckoo Search (CS) [115], Mine Blast Algorithm (MBA) [116], Social Spider Optimisation (SSO) [117], Butterfly Optimization Algorithm (BOA) [118], was reported to provide a better solutions. These typical techniques have a number of problems, including premature convergence, long execution times and getting trapped in local maxima/minima. To overcome these shortcomings, a particular algorithm is insufficient to solve all issues, prompting researchers to create new fields that combine evolutionary algorithms and intelligent controllers.

The Fuzzy Logic Control (FLC) is a flexible tool that can be applied to enhance the PMC performance in the $HRES$ systems, especially with unpredictable variables or uncertainties. For this purpose, several publications have been published to improve $PMCs$. In Ref. [119] the author presented a supervisory PMC based FLC to optimize the energy demanded. The PMC is designed to employ predictive real-time and long-term data programming based on FLC [120]. A $HRES$ controlled by FLC was proposed and designed to obtain the value SOC of the battery [121]. To perform PMC concepts based on FLC, many algorithms have been developed. The same goal was attained in [122] where a fuzzy expert with a genetic algorithm (GA) was proposed to control the power output of the battery. Other works used FLC in the PMC along with PSO for further reaching in terms of electricity savings, such as [123] and [124]. In the same goal, to ensure the efficient scheduling of $HRES$ with high adaptability considerations in [125]. The multi-objective optimization of FLC is investigated in [126].

Recently, Fractional Order (FO) is getting concentration from researchers to improve some control design in industrial applications [127, 128, 129, 130, 131, 132, 133]. Usually, the standard PID controller has three parameters: K_p ,K_i and K_d but the utilization of FO derivative (α) and integral (β) parameters can improve the performance of PID regulators. The appropriate set of parameters ($\alpha, \beta, K_p, K_i, K_d$) has a significant impact on the $FOPID$ controller's quality [84], it has better dynamic performances than conventional PID controller.

In this regard, many studies are devoted to investigating the utilization of a FO control system in dynamic price regulation for the balance of energy demand and generation in a smart grid energy market [97]. The gap between demand and generation has narrowed in [97] compared to the PI controller [134] which tracked the generated power after broadcasting delays and an overshoot.

Nevertheless, to give a good response better than the $FOPID$ controller, several studies tend to hybrid the FLC theory with $FOPID$ to design a new controller called Fractional Fuzzy controller ($FOFPID$) [135, 136]. In comparison to the $FOPID$ controller, the $FOFPID$ might be an excellent alternative because the FLC updates the $FOPID$ errors changes [137].

The proposed work investigates the applicability of $FOFPID$ controller in PMC problem. According to the knowledge, a previous study extended the utilization of $FOFPID$ control to enhance the performance of the PMC problem with different structures of $FOFPID$ [98, 138, 139].

Therefore, the parameters of $FOFPID$ can be solved using various optimization methods. Some of these optimization methods used are as follows: metaheuristic optimization Bat Algorithm (BA) [135], Quasi-Opposition Harmonic Search ($QOHS$) [14], Particle Swarm Optimization (PSO) [98, 138], a Bacterial Foraging Optimization Algorithm ($BFOA$) [136], Imperialist Competitive Algorithm (ICA) -based $FOFPID$ [140], $FFOPI - FOPD$ [139], $FOPI$ with Derivative Filter ($FOPIDF$) [141], Whale Optimization Algorithm (WOA) [142, 143]. As a contribution, some recently developed structures of $FOFPID$ controllers and their corresponding algorithm techniques are well summarized in ref [144].

All previous swarm algorithms were based on a combination of deterministic rules and insufficient randomness [145]. Therefore, the influence of randomness should be increased with the increase of iteration numbers. With the desirable properties, we require another investigated algo-

rithm in this research. To carry that out, optimization techniques such as Spider Social Optimisation (SSO) [146] are applied to calibrate the FO parameters which allow the set of FLC output accurately. Considering the trade-offs between the high randomness conditions and sensitivity to initial conditions; inclusion of the SSO algorithm may provide better performance of the proposed $FOFPD+I$ controller.

4.2 Description and Modeling of the System

The hybrid power system studied in our work contains two renewable energy sources: solar photovoltaic (PV), Wind turbine generator (WTG) and Battery energy storage system ($BESS$). The schematic depiction of the $HRES$ system with different components is shown in Figure 4.1, with the nominal values and ratings of its various elements shown in Table 4.1. In the $HRES$, a centralized PMC controller is used since there are less control variables. Despite its many benefits, the centralized control system may cause a few performance criteria to deteriorate as a result of a single control signal. Nonetheless, it results in adequate time domain performance in our study.

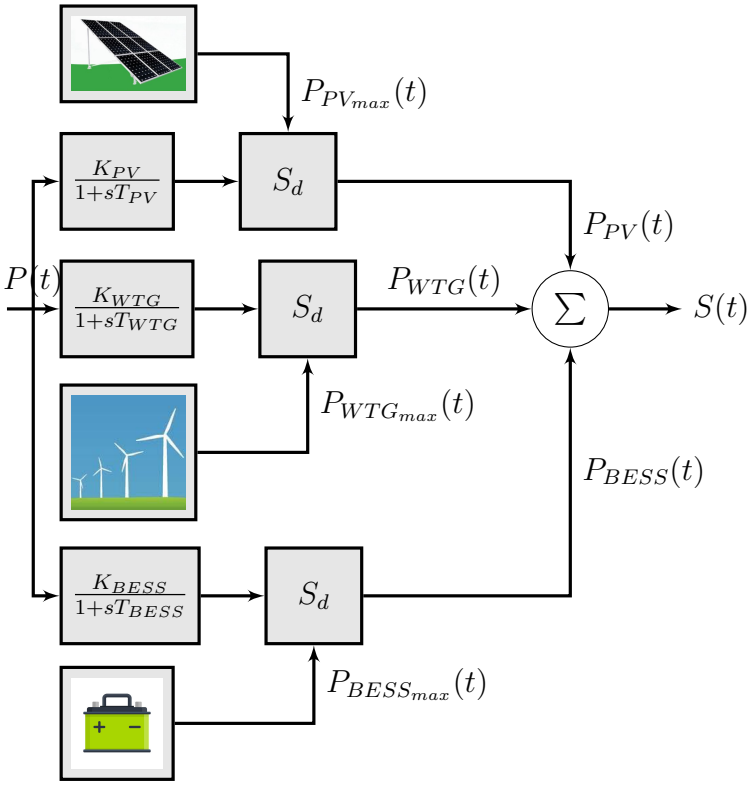

Figure 4.1: Hybrid PV/WIND/BATTERY power system.

A transfer function is used to simulate the dynamics of any energy source [147]. The transfer functions of the PV, WTG and $BESS$ may be modeled using first-order transfer functions with the appropriate gain and time constants listed in Table 4.1 for small signal analysis. The power generated by various generating subsystems is represented by the transfer functions of each unit. For $HRES$ (see Figure 4.1), the total output $S(t)$ may be expressed as;

$$S(t) = P_{PV}(t) + P_{WTG}(t) + P_{BESS}(t) \tag{4.1}$$

The demand–supply imbalance can be expressed in terms of a mathematical model defined by the error state (e) as follows;

$$e(t) = D(t) - S(t) \tag{4.2}$$

A closed-loop optimal price control system provides a consistent approximation of balance error to zero $e(t) = 0$. When $e(t) > 0 (e(t) < 0)$, supply is less (greater) than the demand, and supply should increase (decrease) to achieve the balance state $e(t) = 0$. In this approach, controlling energy balance may be accomplished using economic theoretic tools in this manner. From the expression 4.2, the continual enforcement of the state through price regulation enables real-time, dynamic control of the Hybrid PV/Wind/Battery energy system.

An analytical model to represent suppliers was built, with their energy generating capacity approximated by a polynomial of energy prices, in order to run a simulation of closed-loop control. Based on s-domain models of energy production volume varying with energy costs, the following transfer function based on production delay from energy suppliers may be used;

$$S = S_d(p)\frac{1}{\tau s + 1} \tag{4.3}$$

where,the polynomial $S_d(p) = \sum_{i=0}^{d} a_i P^i$ represents the price responses of energy suppliers with a_i coefficients and d degree of the polynomial. The time constant τ introduces a capacitive delay to the energy production model defined by the transfer function $1/(\tau s + 1)$. This model predicts that when the price increases, the energy generation volume assigned by energy suppliers to sell to grid users will increase dramatically as a result of the increased profit potential. Here, the function

for generating prices was supposed to be as $S_d(p) = 0,001p^2 + 1,7p$.

4.2.1 Model of photovoltaic system

For small signal analysis, the transfer functions of the PV may also be represented as [148],

$$G_{PV} = \frac{K_{PV}}{1 + sT_{PV}} \tag{4.4}$$

where K_{PV} and T_{PV} are the gain and time constants carried by the PV system, respectively.

4.2.2 Model of wind generator

The first order transfer function may alternatively be expressed as a lag compensator as follows [148],

$$G_{WTG} = \frac{K_{WTG}}{1 + sT_{WTG}} \tag{4.5}$$

where K_{WTG} and T_{WTG} are the gain and time constants of WTG, respectively. For synchronizing the two units, PV and WTG, the PV system needs an inverter DC/AC.

4.2.3 Model of battery energy storage system

A resourceful tool must be present in order to quickly correct for power and load fluctuations in order to maintain a constant balance between generation and demand. Thus, the utilization of $BESS$ units can be easily integrated by knowing the number of batteries and the total power that release or absorb power. $BESS$ can be modeled by first order transfer functions with the associated gain and time constants as [138],

$$G_{BESS} = \frac{K_{BESS}}{1 + sT_{BESS}} \tag{4.6}$$

where K_{BESS} and T_{BESS} are the gain and time of the $BESS$ system, respectively.

Table 4.1: Hybrid Power System Parameters.

HRES	Parameters	Values
PV	K_{PV}	1
	T_{PV}	0.3
WIND	K_{WTG}	1
	T_{WTG}	1.5
BATTERY	K_{BESS}	0.003
	T_{BESS}	0.1

The principle of the PMC control theory is to satisfy and monitor the power, regardless of the variations of solar irradiance and wind speed. The PMC controls the difference between instantaneous demand and generation power. To satisfy these significant features of PMC, the next sections offer an explanation of its overall structure of the controller.

4.3 Design of the Fuzzy Logic Controller System

A Fuzzy Logic Controller (FLC) is proposed to power management of the hybrid system. The main purpose is to control the power mismatch between supply and demand. The FLC process is based on empirical rules created by a human operator that are conducted on a non-linear system [149]. Each rule is manipulated directly by the $IF-THEN$ format. A list of rules constitutes a rule set, or rule base. An important characteristic in the development of FLC is the partitioning of the control scheme into operating regions collecting input-output.

The basic structure of a fuzzy controller consists of three components: fuzzy rules, membership functions, and an inference mechanism. There are two major types of fuzzy systems: the Mamdani [150] and the Sugeno [151]. A comparison of two fuzzy logic systems (Mamdani and Sugeno) is reported in various works.

Despite offering numerous architectures of $FLCs$ in the literature, the Fractional Fuzzy $PD^{\alpha}+I$ ($FOFPD+I$) was chosen since it has remarkable robustness and stability characteristics [147]. The configuration of the $FOFPD+I$ controller is shown in Figure 4.2. Under this configuration,

the output of the fractional fuzzy PD^{α} controller ($FOFPD$) is summed to an integral action to give the total controller output. But in the present case the integer order rate of the error at the input to eliminate the step response steady state error. However,we use this topology, but there are other structures comparable to their integer order counterparts.

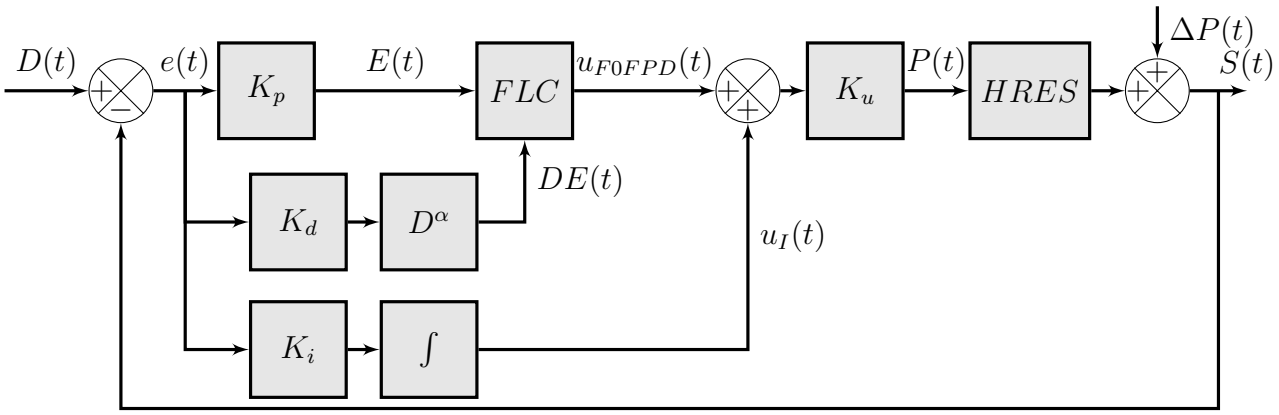

Figure 4.2: Block diagram of FOFPD+I controller

It has three gains K_p, K_d, K_i and α along with K_u are the optimization variables in the SSO algorithm to be calibrated. The above scheme can be expressed by the following model:

$$\begin{aligned} P(t) &= \left[u_{FOFPD}(t) + u_I(t)\right] K_u \\ &= \left[f(K_p e(t) + K_d D^{\alpha} e(t)) + K_i \int e(t)dt\right] k_u \\ &= \left[f(E(t) + DE(t)) + K_i I e(t)\right] K_u \end{aligned} \tag{4.7}$$

The inputs of the fuzzy system are the error signal multiplied by a constant (proportional gain) denoted by E ($E(t) = K_p e(t)$) and the fractional derivative of error multiplied by a constant (integral gain) denoted by DE ($DE(t) = K_d D^{\alpha} e(t)$), respectively; and the defuzzified output signal is $u_{FOFPD}(t)$. The output/input of the system have been denoted by $S(t)/D(t)$.

Suppose that each input and output are described by 7 linguistic variable, (NL, NM, NS, ZR, PS, PM, PL) denote "Negative Large", "Negative Medium", "Negative Small", "Zero", "Positive Small", "Positive Medium" and "Positive Large", respectively. Consequently, the control strategy is modeled by a set of fuzzy rules that can be made within the $IF - THEN$ rule. The selected rule base of fuzzy system to be calibrated has been given in Table 4.2. Consequently, $u_{FOFPD}(t)$

consists of 7 linguistic variables, or equivalently 7 membership functions, there are 49 different combinations or membership functions forms (see Figure 4.3. The Figure 4.4 shows the surface plane of the selected membership functions that model the premises of every rule.

Table 4.2: Rule base of E,DE inputs and the FLC controller outputs.

DE \ E	NL	NM	NS	ZR	PS	PM	PL
NL	NL	NL	NL	NL	NM	NS	ZR
NM	NL	NL	NL	NM	NS	ZR	PS
NS	NL	NL	NM	NS	ZR	PS	PM
ZR	NL	NM	NS	ZR	PS	PM	PL
PS	NM	NS	ZR	PS	PM	PL	PL
PM	NS	ZR	PS	PM	PL	PL	PL
PL	ZR	PS	PM	PL	PL	PL	PL

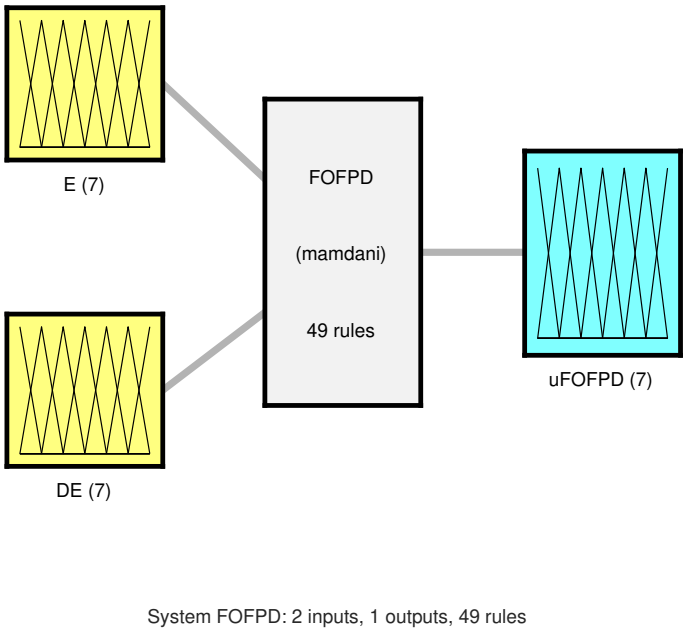

Figure 4.3: Structure of the fuzzy inference system.

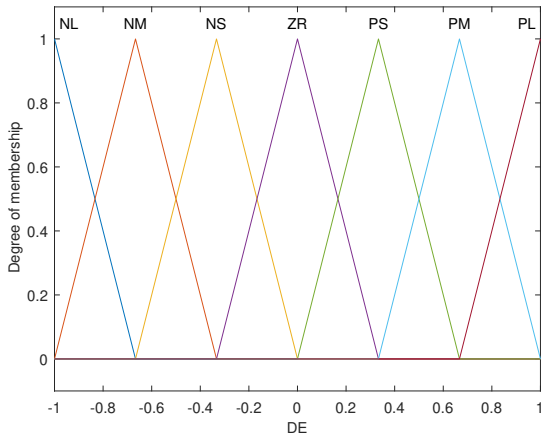

(a) Input E(t)

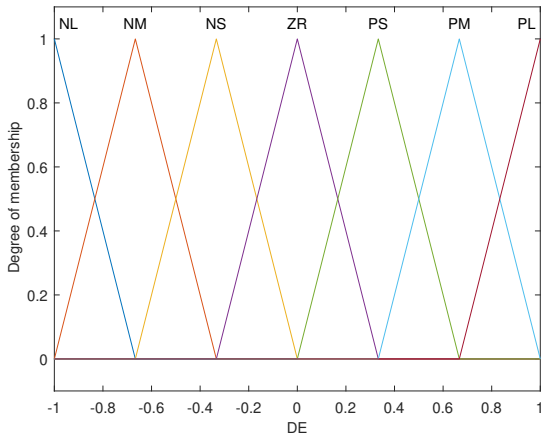

(b) Input DE(t)

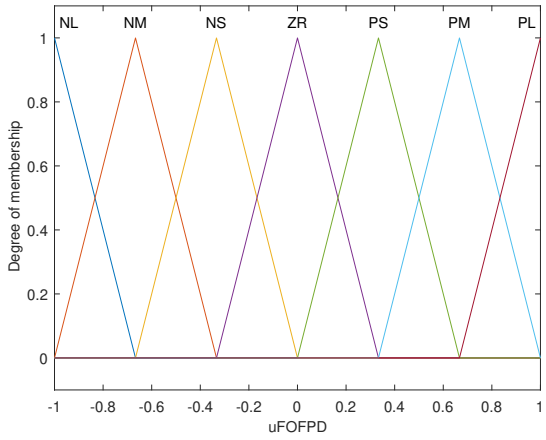

(c) Output u(t)

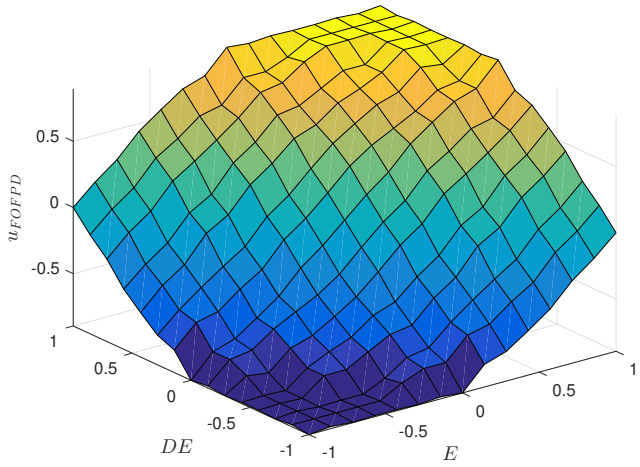

(d) Control Surface

Figure 4.4: FOFPD fuzzy controller with two inputs: (a) membership functions for error input; (b) membership functions for integral error input; (c) membership functions for output; (d) control surface.

4.4 Social Spider Optimization Algorithm

Cuevas et al [146] proposed the Social Spider Optimization (SSO) method, which is a population-based swarm intelligence system. The SSO algorithm was inspired by the ideas of the social behavior of the social spider colony, which comprises social individuals and a communal web. Because of its efficiency, the SSO has been applied in a variety of applications, particularly when it is applied to solve global optimization complications [152].

The basic concepts of the SSO algorithm are planned to solve the global nonlinear optimization

problem with constraints that can be defined as follows:

$$\begin{cases} Minimize \;\; f(x) \;\; where \qquad x = (x^1, ..., x^d) \in \mathbb{R}^d \\ Subjectto \qquad x \in X \end{cases} \tag{4.8}$$

where $f : R^d \rightarrow R$ the nonlinear function. $X = \{x \in \mathbb{R}^d | l_h \leqslant x^h \leqslant u_h, h = 1, ..., d\}$ is the search space, limited by the lower (l_h) and upper (u_h) constraints.

SSO use N candidate solutions from S population to solve the matter 4.8.Where S is divided into two groups: males (M) and females (F). The number N_f of females F is selected $(65 - 90)\%$ from S, whilst the remaining N_m is treated as male individuals ($N_m = N - N_f$).Then,the set of female members $F = \{f_1, f_2, ..., f_{Nf}\}$,male individuals $M = \{m_1, m_2, ..., m_{Nm}\}$ and groups of population $S = \{s_1, s_2, ..., s_N\}$,where $S = \{F \cup M\}$ corresponding to $S = \{s_1 = f_1, s_2 = f_2, ..., s_{Nf} = f_{Nf}, s_{Nf+1} = m_1, s_{Nf+2} = m_2, ..., s_N = m_{Nm}\}$.

The weight w_i of $i^{th}(i \in 1, ..., N)$ spider's position evaluated by the fitness value $fitness_i$ is formulated as,

$$w_i = \frac{fitness_i - wrost}{best - wrost} \tag{4.9}$$

where the $best$ and $wrost$ fitness values of the S.

In the SSO optimization mechanism, the information transmission between spiders is simulated trough vibrations. A spider i perceives from a spider j according to the following expression:

$$V_{i,j} = w_j e^{d^2_{i,j}} \tag{4.10}$$

where $d^2_{i,j}$ is the spacing between the two spiders. Any spider i can perceive only three types of vibrations:

1. The vibration exchanged by the nearest individual c with a better weight with assumption ($w_c > w_i$) and symbolized by $V_{i,c}$.

2. The vibration transmitted by best element b of the entire population S symbolized by $V_{i,b}$.

3. If i is a male individual, the vibration emitted by the nearest female spider is $V_{i,f}$.

In the SSO algorithm, the operation of population N of spiders begins with $k = 0$ to $k = gen$ deterministic iterations. Every individual in the SSO has various movement characteristics based on the sex of a spider in order to avoid being easily caught in the local optimal solution.Individuals are guided by a variety of evolutionary operators. Therefore, female spiders are affected by the new position f_i^{k+1} by modifying the current spider location f_i^k. These changes are randomly controlled through a probability factor PF. By using this respect, each spider should move according their vibrations in relation to other spiders, which are transmitted through the search space by the following model:

$$f_i^{k+1} = \begin{cases} f_i^k + \alpha.V_{i,c}.(s_c - f_i^k) + \beta.V_{i,b}.(s_b - f_i^k) + \delta.(rand - \frac{1}{2}) & \text{with probability PF} \\ f_i^k - \alpha.V_{i,c}.(s_c - f_i^k) - \beta.V_{i,b}.(s_b - f_i^k) + \delta.(rand - \frac{1}{2}) & \text{with probability (1-PF)} \end{cases} \tag{4.11}$$

The values α, β, δ and $rand$ symbolize random quantities between $[0, 1]$. For the iteration number k,in the entire population S the individuals s_c denote the nearest member to i that conserves a higher weight and s_b represent the best one.

On the opposite side, the male sub-populations spiders are classified into two types: dominant members(D) and non-dominant members(ND). The dominated population D is formed by 50% of the male members whose having higher fitness levels than the complete male set. Consequently, the remaining non-dominant (ND) category regroups the rest of the male population. In the SSO optimization mechanism, male spiders move according to the following model:

$$m_i^{k+1} = \begin{cases} m_i^k + \alpha.V_{i,f}.(s_f - m_i^k) + \delta.(rand - \frac{1}{2}) & \text{if } \mathrm{m}_i^k \in D \\ m_i^k + \alpha.(\frac{\sum\limits_{h \in ND} m_h^k.w_h}{\sum\limits_{h \in ND} w_h} - m_i^k) & \text{if } \mathrm{m}_i^k \in ND \end{cases} \tag{4.12}$$

where s_f denotes the closest female element to the male spider i.

Finally, the mating operation is a couple between D and the female individuals who produce a new individual s_{new} as a result of the combination of a dominant male m_g and other female members within a particular range r. The weight of any generated element defines the probability of influence of each individual into s_{new} and compared with the rest of the population. The wrost

spider is replaced by s_{new} with the best fitness. More details of the complete optimization process are illustrated in [146].

4.5 Objective Function of Control

For the assessment control of the demand–supply imbalance, the calibration process is mentioned in Figure 4.5. In the design stage of $FFOPD + I$ controller, the parameter calibration process is transformed into a multidimensional optimization problem where fractional orders PD^{α}, as well as controller parameters of the fuzzy system, are both considered as decision variables. Under this approach, the complexity of the optimization problem tends to produce multimodal error surfaces whose cost functions are significantly difficult to minimize.To determine the parameters, the proposed method uses the SSO method.

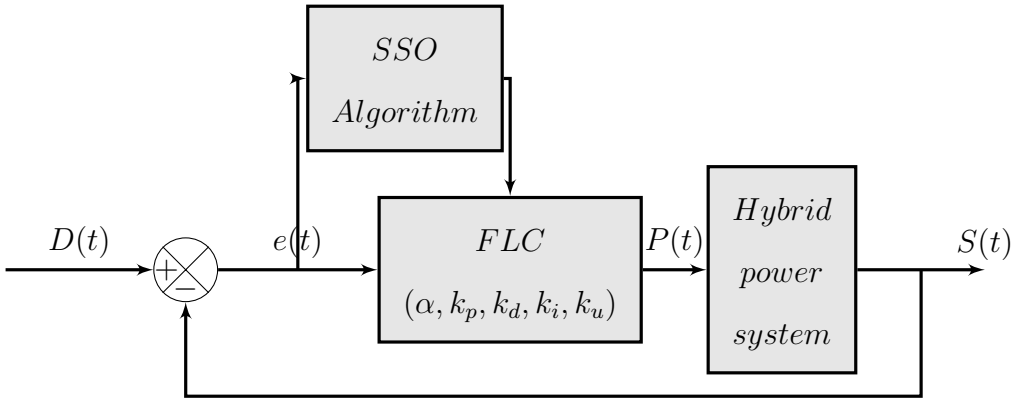

Figure 4.5: Proposed SSO parameters calibration process

Under such conditions, the fractional fuzzy controller parameters can be defined as a variable vector $x = [\,\alpha, K_p, K_d, K_i, K_u]$, represent the spider position for the calibration problem. To evaluate the performance of the $(FOFPD + I)$ controller; the Integral Time Absolute Error $(ITAE)$ criterion has been considered. The $ITAE$ objective function J calculates the difference between the output power $S(t)$ produced by a determined parameter of the vector x and the demand $D(t)$. Therefore, considering the formalism 4.2 to achieve the best quality solution, each step is evaluated

according to the following model:

$$J(x) = \int_0^{+\infty} t|D(t) - S(t)|dt \tag{4.13}$$

where, each parameter of calibration is constrained by limits. Thereby, we can describe the final SSO optimization expression as,

$$\begin{cases} \text{Minimize} \quad J(x) & x = [\,\alpha, K_p, K_d, K_i, K_u] \in \mathbb{R}^5 \\ \text{Subject to} & K_{(p,i,d,u)_{min}} \leq K_{(p,i,d,u)} \leq K_{(p,i,d,u)_{max}} \\ & \alpha_{min} \leq \alpha \leq \alpha_{max} \end{cases} \tag{4.14}$$

min and max indicate the minimum and maximum values of the parameters in the calibration problem.

4.6 Simulation Results and Discussion

The energy is generated by three different resources with the maximum power generation capabilities of the PV system ($P_{PV_{max}}$), the wind system ($P_{WTG_{max}}$) and the battery system ($P_{BESS_{max}}$) being characterized as variable based on hours or days. The maximum installed power generation capacity is,

$$P_{Total_{max}} = P_{PV_{max}} + P_{WTG_{max}} + P_{BEES_{max}} \tag{4.15}$$

Figure 4.6 depicts the total power provided by a hybrid system, as well as the energy conversion from various components over the simulation period of $T = 24Hours$. The total power generated by the generators is larger than the power required except at the moment $16Hours$, where the demand load exceeds the generation. To avoid the problem of a sharp peak at $T = 16Hours$, installing a new source or boosting the capacity of some or all generators will increase total generation. As a matter of fact, it is considered to determine the controller's sensing against short external disturbances. The scenario for the requested power is also included in the figure in which she has oscillations rated to the total generation but it has sharp fluctuation at $t = 21$ Hours. Depending

on the weather conditions, the power generated by the wind drops to significantly different levels from the first hour to the midpoint of the whole simulation period, then rises to the same beginning level at the end of the duration. On the other hand, the converted power from the photovoltaic cells begins to increase from the sixth hour achieving the max value in half of total period and decreases similarly to the zero value. $P_{BESS_{max}}$ denotes the corresponding energy-storing component of the $HRES$ system; as energy conversion from wind decreases, the state of conversion increases to compensate the resource degradation until conversion from solar cells increases.

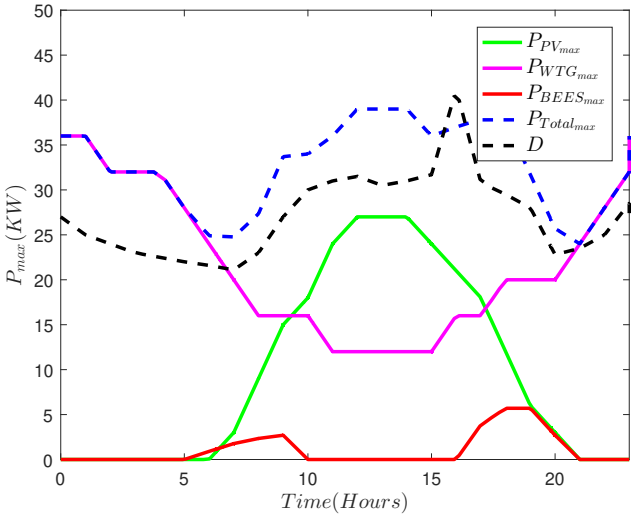

Figure 4.6: Hourly power generation capacities.

For the Closed-loop system performance specifications,we select the search space for $FOFPID$ controller parameters as follow,

$$0 \leq \alpha, K_{(p,i,d,u)} \leq 5 \tag{4.16}$$

where the parameters of the algorithms are set as follows:

- SSO parameters: PF = 0.7, Number of spiders = 30, Maximum iterations = 100, Lower and upper percentages of females are 65 and 90 %.
- GA parameters: Population size = 30, Maximum iterations = 100, Crossover rate = 0.85, Mutation rate = 0.08.
- PSO parameters: Nombre of particles = 30, Nombre of iterations = 100, Inertia weight (w) = 0.529, Congitive factor (c1) = 1.5, Social factor (c2)= 1.5.

To demonstrate the effectiveness of the overall power management strategy, a simulation was performed in MATLAB/Simulink environment using the initial conditions $x_0 = [1, 1, 1, 1, 1]$.

Table 4.3: Calibrated parameters of FOFPD control.

	α	k_p	k_d	k_i	k_u	ITAE
PSO	0.5749	4.4062	1.6112	2.2194	4.5131	1977.644398
GA	0.8537	2.8381	0.9048	2.7402	1.4133	1618.836832
SSO	0.7549	1.3087	0.5883	0.5808	4.9991	977.044969

Table 4.3 shows the best controller parameters obtained through the three algorithms, considering 100 iterations. According to the produced $ITAE$ reported values, the proposed SSO method provides better performance than PSO and GA. The SSO is averaged over 26 executions obtaining the calibrated parameters despite the nonlinear relationship between fuzzy logic memory and fractional calculus. Also, the calibrated parameters are better and the objective function is reached. Based on the aforementioned desired properties, the assisted version of the SSO algorithm is a preferable choice in the instance of the $FOFPD + I$ controller.

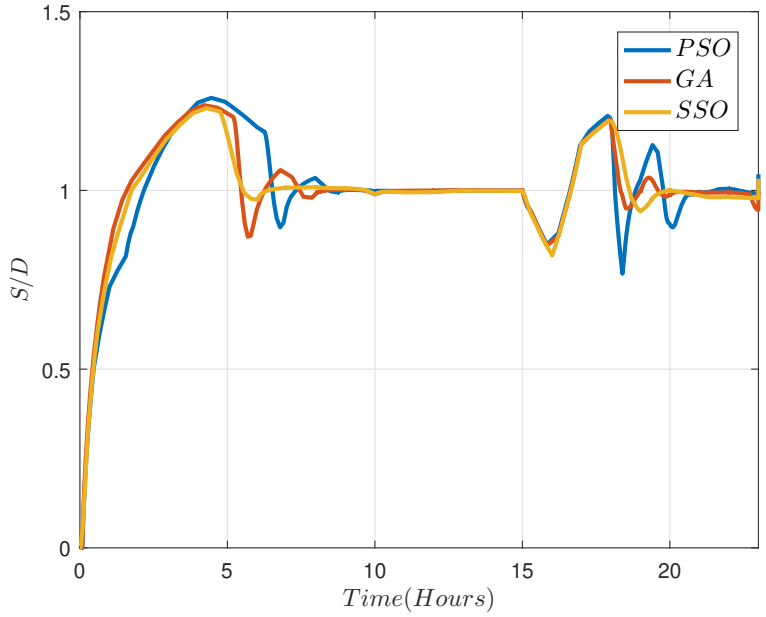

Figure 4.7: Step response plot of HRES applying the calibrated parameters

Figure 4.7 presents the step demand responses of the designed closed loop control system of with the setting of previous parameters. In terms of settling time, the SSO settles very quickly

after a short transient gives the smallest average error between needed and generated power values. Furthermore, the PSO and GA configurations settles after very high peaks corresponding to high daily average volatility energy. In this case, the system become unstable under peak demand, but the $FOFPD + I$ controller under SSO sets can cover the errors coming from this problem and converge more rapidly than the PSO and GA respectively. The selection of SSO algorithm exhibits good performance in terms of rapidity, robustness, average energy shortage error and energy peak.

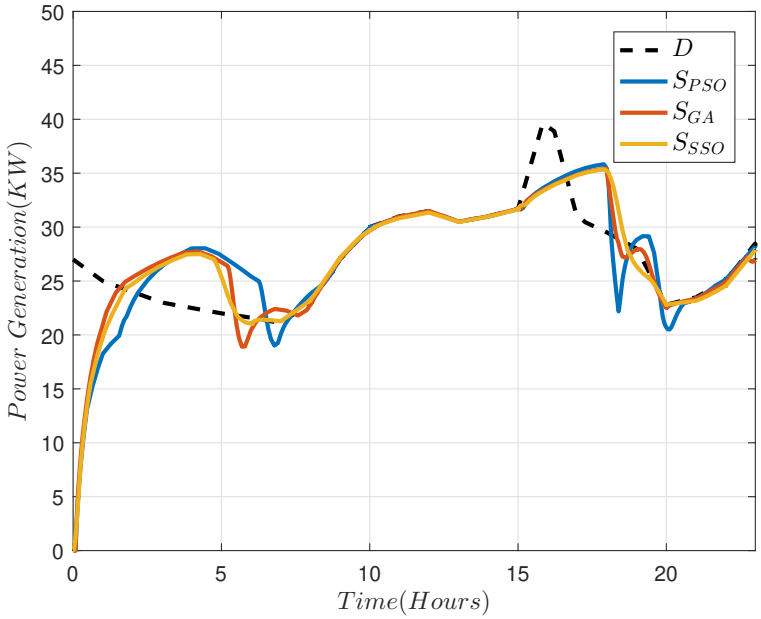

Figure 4.8: HRES power generation

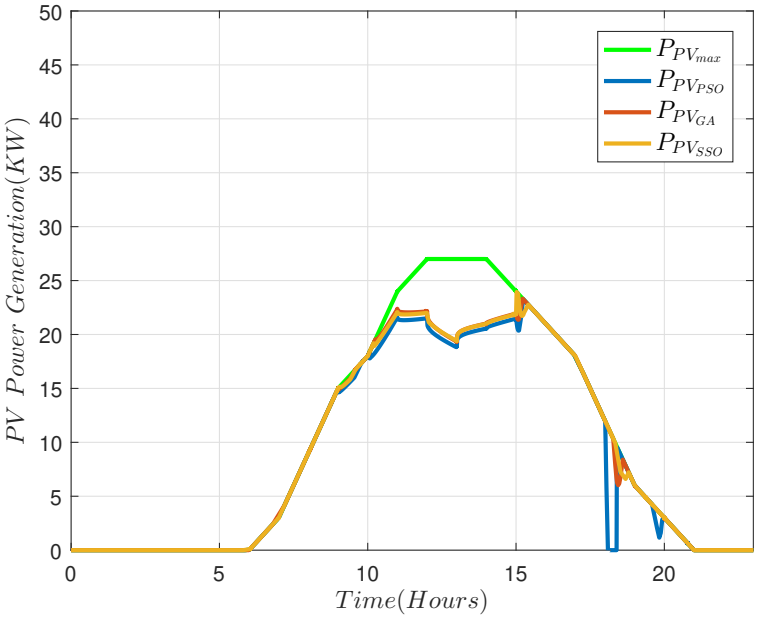

Figure 4.9: PV power generation

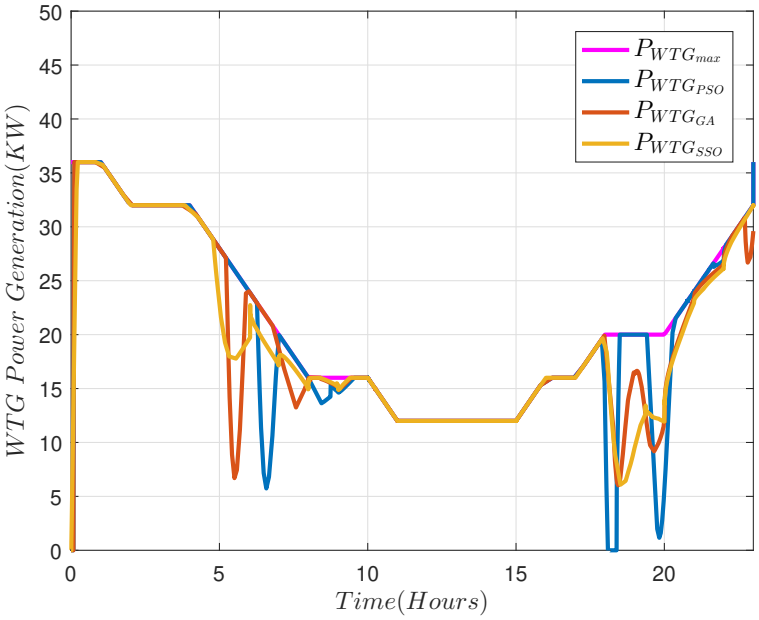

Figure 4.10: WIND power generation

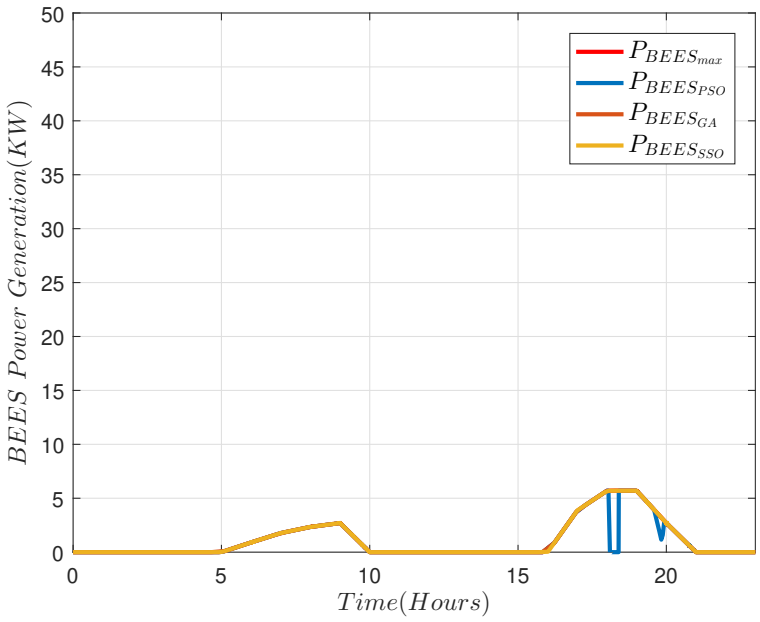

Figure 4.11: BATTERY power generation

Figures 4.8,4.9,4.10,4.11 shows the characteristics of the actual power generation of all $HRES$ components involved in energy compensation in order to supply power to consumers. Meanwhile, the energy-providing processes use the proposed control system, which collects data and identifies the element from which energy is taken to compensate for the shortfall in total energy needed to meet the demand variables.

The suggested control has a direct impact on all $HRES$ system components. Firstly, the wind energy conversion system (Figure 4.10) provides abundant, densely aggregated, high-energy at a fast set-up time. During this period, the excess of the intermittent energy can be stored in the battery. Then the PV panels (Figure 4.9) and battery (at alternating intervals) begin immediately to supply the system to make up for the wind generating shortage enough to supply the entire demand. Under the critical sharp peak, the robustness of the proposed control was characterized by finitegain stability. When compared to the controller with PSO and GA parameters, numerical results demonstrate that the $FOFPD + I$ controller performs better with the SSO algorithm.

The optimised energy value for the $HRES$ system can be stored in the battery as static energy. An important portion of the power available at the beginning of the day results from the effective influence of the proposed controller on the $HRES$ system components, which is a first-order function on the opposite side of the overall $HRES$ system characterized by a nonlinear function. Such

a situation of great benefit of power can affect the battery or charging system elements.

As a result, there is a significant performance difference between the controllers. The suggested SSO algorithm improves system performance and it outperforms the PSO and GA configurations in terms of steady state error, power variations and settling time. To ensure the minimum energy compensation, the control scheme proposed has high robustness properties by anticipating its impact by reducing fluctuations in power generation. Thus, it may be concluded that the best system response may be gained with the SSO algorithm tuned to the $FOFPD + I$ controller.

Change in load is a noteworthy source of perturbation in $HRES$ power systems. Although we previously added a sharp peak demand, for better monitoring the performance of the calibrated parameters generated by the SSO algorithm, the $HRES$ model was subjected to significant load perturbation $\Delta P(t) = 0.05D(t)$. As depicted in Figure 4.12 there is no significant mismatch between load and generation. We can accept the excellent fulfillment between the internal and external disturbances in terms of rejection using the same control parameters. Also, The performance of the entire system are improved in both static and dynamic regimes.

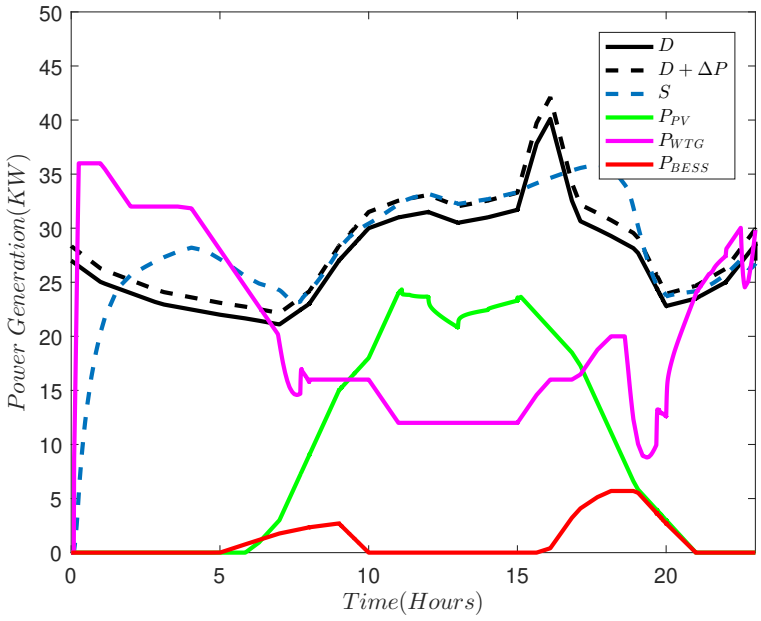

Figure 4.12: HRES power generation with disturbance

4.7 Conclusion

This work proposes an intelligent control technique for power management PMC in a hybrid renewable energy system ($HRES$) using a fractional fuzzy $FOFPD + I$ controller. Under the suggested scheme, the parameters of the controller are considered as decision variables and their required task is the calibration of the fuzzy system. In the calibration process, the relevant parameters of the controller are transformed into a restricted optimization problem. We define only one objective function based on the absolute value of the balance between supply and demand in the $HRES$ power system. The objective function solution is then allocated using an adapted SSO algorithm through the $ITAE$ criterion. Once the SSO has converged on the nominal system, the estimated parameters have been evaluated considering the dynamical system. To assess the performance of the SSO algorithm, it has been compared to conventional PSO and GA algorithms.The results demonstrate that the proposed algorithm outperforms the conventional in terms of robustness properties and is able to handle internal and external disturbances. Finally, the aims were attained by an intelligent optimization algorithm that enhanced the dynamic performance of the PMC controller with low power consumption and overall $HRES$ high power conversion efficiency. In future research, several algorithms that are based on evolutionary computation principles to calibrate the parameters of a fuzzy system should be investigated, with a focus on enhancing power management.

Conclusions and Further Work

Conclusions and Further Work

The current research focused on energy saving in hybrid systems, which is an important topic in electrical engineering applications. In today's renewable energy systems, the growing interaction of technological, economic, and environmental restrictions necessitates enhanced design and control approaches. Our objectives were to study control laws in hybrid systems based on several renewable energy sources that constitute an interesting alternative for the better exploitation of energy in electrical systems.

In the first Chapter, we presented the future prospects of renewable energy in Algeria, where we focused on the importance of microgrids in the energy transition. Then, the state of the art concerning the production of electrical energy from the two wind and solar generation systems was presented. The two energy sources' modes of operation have been described in detail. There's also a reminder of the key concepts that go into integrating a hybrid renewable energy system. Because the microgrid is being considered in this study, multiple topologies were built based on the literature review to combine the essential components that make up microgrid systems (the panels, wind, battery, and inverters, as well as the loads). We discovered that the hybrid microgrid with three-stage designs and fewer converters is the preferable choice after analyzing various topologies and control layers. The study of energy management in a hybrid microgrid system architecture provides an idea for energy conservation through efficient control of power quality and management.

The second Chapter was divided into two parts, the first of which was specifically designed to ensure the power balance in the PV system. After modeling the PV array based on the manufacturer's data sheet, the $MPPT$ technique based on perturb and observe optimisation was used in PV systems to maximize the output power. Furthermore, as a last resort, in view of the PV system analysis, a robust and stable control strategy control of the boost inverter plays a central

role in maintaining the voltage stability of the DC bus. In the second part, the regulated voltage is supposed to be used as an input in modeling a three-phase DC/AC inverter with an output power filter for the application. The space vector PWM technology has been considered, and it is well presented and discussed. Furthermore, the state space representation of an inverter power system in the continuous and discrete-time domains is illustrated. Furthermore, a control approach should be proposed for designing the robust voltage regulation of a DC/AC inverter system.

In the Chapter 3, the power quality problem was addressed for better energy-saving through a new proposed controller. Within the study, we designed conventional servomechanism control for the voltage of a three-phase PWM inverter. In addition, this was followed by designing a new voltage controller employing the optimised structure of the $FOPID$ controller with $AFWs$ approaches. The comparison of results in the frequency and temporal domains shows improvement in the robust performance and THD reduction in the second one. Thus, the intended power quality control objective has been met, and the load efficiency has been increased.

In Chapter 4, the power management problem was addressed by a newly developed and implemented control method for the automatic operation of the microgrid. The fractional order controller was created to control the FLC output through different optimisation tools. The results were compared based on the variation in power output of the microgrid system, where the social spider algorithm provided better performance in noise rejection and better power management.

In terms of future work in the field of energy-saving control, it will be interesting to see if new techniques in the PV system's $MPPT$ control model can be used to assure stable and optimum DC bus voltage regulation. Furthermore, given the difficulty of optimum asset scheduling in systems with a variety of uncertainties, it is critical to apply more fundamental or hybrid methods to get better parameter values for controllers. Experimental validation of the idea to validate the suggested control techniques in real time is another way to progress.

Appendix

Appendix A

Basic Concepts of Fractional Order Calculus

A.1 Fractional Order Calculus

Fractional order dynamic systems are modeled using differential equations, involving non-integer and/or derivative integral operators. Since these operators produce continuous irrational transfer functions, or discrete transfer functions of infinite dimension, fractional models are normally studied using simulation tools instead of analytical methods. This section provides an overview of the fundamental aspects of Fractional Calculus and the discrete integer/derivative-order approximations of the fractional order operators.

The differential-integral operator, represented by ${}_aD_t^\alpha$, combines the fractional derivative and integral into a single expression, which is defined as:

$$ {}_aD_t^\alpha = \begin{cases} \frac{d^\alpha}{dt^\alpha} & \alpha > 1 \\ 1 & \alpha = 0 \\ \int_\alpha^t (d\tau)^\alpha & \alpha < 1 \end{cases} \tag{A.1} $$

where $\alpha \in \mathbb{R}$,and a,t are the operation bounds. The most widely used approximation models of the fractional derivatives are the Grunwald-Letnikov, Riemann-Liouville and Caputo [153].

Let f be a continuous function defined on $\mathbb{R}$, then the Grunwald-Letnikov approximation of fractional derivative of the function is defined as,

$$D_t^{\alpha} f(t) = \lim_{h \to 0} \frac{1}{h^{\alpha}} \sum_{j=0}^{\infty} (-1)^j \binom{\alpha}{j} f(t - jh) \tag{A.2}$$

In the numerical calculation, the approximation of the $\alpha - th$ derivative at the points $kh, (k = 1, 2, ...)$ is expressed as follow,

$${}_{(k-\frac{M_m}{h})}D_{t_k}^{\alpha} f(t) \approx h^{-\alpha} \sum_{j=0}^{k} (-1)^j \binom{\alpha}{j} f(t_k - j) \tag{A.3}$$

where M_m denotes the memory length, h is the time step ($t_k = kh$). For the calculation of the binomial coefficients $(-1)^j \binom{\alpha}{j}$, we can use the following form with initial condition,

$$c_0^{(\alpha)} = 1, \qquad c_j^{(\alpha)} = (1 - \frac{1 + \alpha}{j}) \tag{A.4}$$

After some rearrangement we can obtain the general numerical solution of the fractional differential equation,

$$y(t_k) = f(y(t_k), t_k) h^{\alpha} - \sum_{j=1}^{k} c_j^{(\alpha)} y(t_{k-j}) \tag{A.5}$$

A.2 Numerical discrete approximation of fractional operators

In the Laplace domain, the fractional operator is defined as $L({}_aD_t^{\alpha} f(t)) = s^{\alpha} F(s)$, with zero initial conditions. Several methods for creating discrete versions of continuous operators of type s^{α} have been presented [154]. The Grunwald-Letnikov approximation was employed in this research because of its significant properties for creating discrete data [155]. Considering this approach, the

discredited model of the continuous fractional operators is given by,

$$\begin{aligned} D^{\alpha}(z^{-1}) &= (\frac{1-z^{-1}}{T_c}) \\ &= \sum_{k=0}^{\infty} (\frac{1}{T_c})^{\alpha}(-1) \binom{\alpha}{k} z^{-k} \\ &= \sum_{k=0}^{\infty} h^{\alpha}(k) z^{-k} \end{aligned} \tag{A.6}$$

where $h^{\alpha}(k)$ is the impulse response function, T_c is the sampling frequency. In the previous literature works, it has been demonstrated that the rational model converge considerably faster than polynomial method. Consequently, the most notably Padé approximation method has been employed to solve a fractional model by using the following expression,

$$\begin{aligned} H(z^{-1}) &= \frac{b_0 + b_1 z^{-1} + ... + b_m z^{-m}}{a_0 + a_1 z^{-1} + ... + a_n z^{-n}} \\ &= \sum_{k=0}^{\infty} h(k) z^{-k}, \qquad m \leqslant n \end{aligned} \tag{A.7}$$

where the values m,n and the modifiable parameters a_i and b_i are calculated by replacing the first $m + n + 1$ coefficients of $h^{\alpha}(k)$.

Appendix B

Datasheet BP MSX120

bp solar

BP MSX 120

120-Watt Multicrystalline
Photovoltaic Module

BP Solar's MSX series is a premium line of PV modules with a 25-year performance warranty, tightly controlled electrical parameters, and labeling showing each module's tested electrical characteristics. Providing 120 watts of nominal maximum power, the MSX 120 is used primarily in large battery-equipped PV systems or—through an inverter—to provide AC power directly to a load. Typical applications include grid-supplemental residential and commercial systems, telecommunications, remote villages and clinics, pumping, and land-based navigation aids. Its attractive bronze-anodized frame also suits it well for architectural applications.

This product is available as a framed module or an unframed laminate, in 12V or 24V nominal configurations, with either:

- Dual high-volume junction boxes which allow on-site 12V/24V selection by rewiring (MSX 120);
- Installation-speeding DC-rated polarized connectors (MSX 120MC).

Proven Materials and Construction

BP Solar's quarter-century of field experience shows in every aspect of these module's construction and materials:

- 72 multicrystalline silicon solar cells configured as one series string or two 36-cell series strings (bypass diodes are included);
- Cells are laminated between sheets of ethylene vinyl acetate (EVA) and high-transmissivity low-iron 3mm tempered glass;
- Frame strength exceeds requirements of certifying agencies.

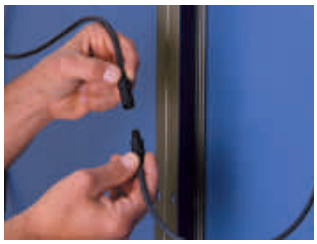

Weatherproof Connectors

MSX 120MC output is via heavy-duty (4mm²/AWG #12) output cables with polarized weatherproof DC-rated connectors which provide reliable low-resistance connections, eliminate wiring errors, and speed installation. Asymmetrical cables enable side-by-side or end-to-end module placement in arrays.

High-Capacity Versatile Junction Box

The junction boxes of the MSX 120 are raintight (IP54 rated) and accept PG13.5 or 1/2" nominal conduit or cable fittings. Their volume (411cc, 25 cubic inches) and 6-terminal

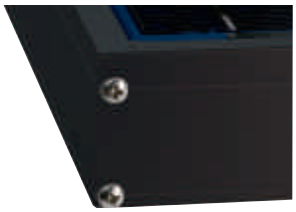

Bronze Anodized Universal Frame

connection blocks enable most system array connections (putting modules in series or parallel) to be made right in the boxes. Options include:

- an oversize terminal block which accepts conductors up to 25mm² (AWG #4); standard terminals accept up to 6mm² (AWG #10);
- a Solarstate™ charge regulator.

Products with junction boxes may be rewired to provide 12V or 24V output.

Limited Warranties

- Power output for 25 years;
- Freedom from defects in materials and workmanship for 5 years.

See our website or your local representative for full terms of these warranties.

Individually Tested and Labeled

Each module tested and labeled with its actual output—voltage, current, and power at maximum power point (P_{max})—at Standard Test Conditions and Standard Operating Conditions.

BP MSX 120

MSX 120 laminates also qualify for the above listings and certifications; MSX 120MC laminates are UL-recognized. MSX 120 modules and laminates with junction boxes are also certified by PowerMark Corporation and approved by Factory Mutual Research for application in NEC Class 1, Division 2, Groups C & D hazardous locations.

Quality and Safety

MSX 120 and MSX 120MC modules are manufactured in our ISO 9001-certified factories, listed by Underwriter's Laboratories for electrical and fire safety (Class C fire rating), certified by TÜV Rheinland as Class II equipment, and comply with the requirements of IEC 61215 including:

- repetitive cycling between -40°C and 85°C at 85% relative humidity;
- simulated impact of 25mm (one-inch) hail at terminal velocity;
- a "damp heat" test, consisting of 1000 hours of exposure to 85°C and 85% relative humidity;
- a "hot-spot" test, which determines a module's ability to tolerate localized shadowing (which can cause reverse-biased operation and localized heating);
- static loading, front and back, of 2400 pascals (50 psf); front loading (e.g. snow) of 5400 pascals (113 psf).

Electrical Characteristics[1]

	MSX 120	MSX 110[4]
Maximum power (P_{max})[2]	120W	110W
Voltage at P_{max} (V_{mp})	33.7V	33.6V
Current at P_{max} (I_{mp})	3.56A	3.3A
Minimum P_{max}	114W	105W
Short-circuit current (I_{sc})	3.87A	3.6A
Open-circuit voltage (V_{oc})	42.1V	41.6V
Temperature coefficient of I_{sc}	(0.065±0.015)%/°C	
Temperature coefficient of V_{oc}	-(80±10)mV/°C	
Temperature coefficient of power	-(0.5±0.05)%/°C	
NOCT[3]	47±2°C	
Maximum system voltage	600V (U.S. NEC rating) 1000V (TÜV Rheinland rating)	
Maximum series fuse rating	20A	

Notes

1. These data represent the performance of typical MSX 110 and MSX 120 products in 24V configuration. The data are based on measurements made in accordance with ASTM E1036 corrected to SRC (Standard Reporting Conditions, also known as STC or Standard Test Conditions), which are:
   - illumination of 1 kW/m² (1 sun) at spectral distribution of AM 1.5 (ASTM E892 global spectral irradiance);
   - cell temperature of 25°C.
2. During the stabilization process which occurs during the first few months of deployment, module power may decrease approximately 3% from typical P_{max}.
3. The cells in an illuminated module operate hotter than the ambient temperature. NOCT (Nominal Operating Cell Temperature) is an indicator of this temperature differential, and is the cell temperature under Standard Operating Conditions: ambient temperature of 20°C, solar irradiation of 0.8 kW/m², and wind speed of 1 m/s.
4. The power of solar cells varies in the normal course of production; the MSX 110 is assembled using cells of slightly lower power than the MSX 120.

MSX 120 I-V Curves

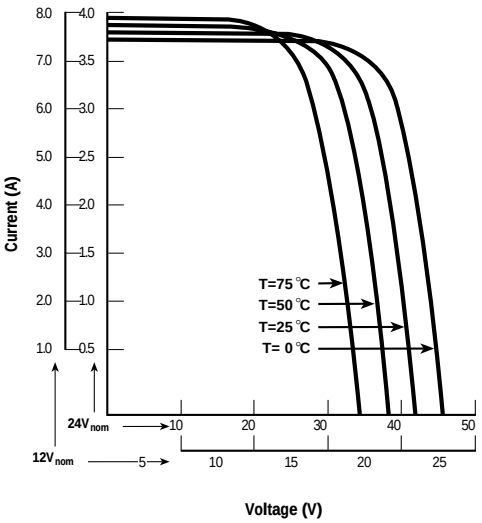

Bibliography

[1] Ernst Worrell, Nathan Martin, and Lynn Price. Potentials for energy efficiency improvement in the us cement industry. *Energy*, 25(12):1189–1214, 2000.

[2] A Boudghene Stambouli, Z Khiat, S Flazi, and Y Kitamura. A review on the renewable energy development in algeria: Current perspective, energy scenario and sustainability issues. *Renewable and sustainable energy reviews*, 16(7):4445–4460, 2012.

[3] Ministry of Energy Transition and Renewable Energy. Actions engagées dans le cadre de la feuille de route de la transition énergétique. https://mteer.gov.dz/bilan07/mobile/index.html.

[4] Houdayfa Ounis and Nawel Aries. On the wind resource in algeria: Probability distributions evaluation. *Proceedings of the Institution of Mechanical Engineers, Part A: Journal of Power and Energy*, 235(5):1187–1204, 2021.

[5] Sustainable Transformation of Algeria's Energy System. http://library.fes.de/pdf-files/bueros/algerien/18343.pdf.

[6] Hatem Ghandir and Ahmed Ramzi Siagh. Algerian energy policy after 2020. *Roa Iktissadia Review*, 10(2):121–131, 2020.

[7] Henrik Lund. Renewable energy strategies for sustainable development. *Energy*, 32(6):912–919, 2007.

[8] Kai Heussen, Stephan Koch, Andreas Ulbig, and Göran Andersson. Unified system-level modeling of intermittent renewable energy sources and energy storage for power system operation. *IEEE Systems Journal*, 6(1):140–151, 2011.

[9] Jin Woo Jung. *Modeling and control of fuel cell based distributed generation systems*. The Ohio State University, 2005.

[10] Omar Ellabban, Haitham Abu-Rub, and Frede Blaabjerg. Renewable energy resources: Current status, future prospects and their enabling technology. *Renewable and sustainable energy reviews*, 39:748–764, 2014.

[11] R Chedid, H Akiki, and Saifur Rahman. A decision support technique for the design of hybrid solar-wind power systems. *IEEE transactions on Energy conversion*, 13(1):76–83, 1998.

[12] Mark Z Jacobson. Review of solutions to global warming, air pollution, and energy security. *Energy & Environmental Science*, 2(2):148–173, 2009.

[13] David Barlev, Ruxandra Vidu, and Pieter Stroeve. Innovation in concentrated solar power. *Solar energy materials and solar cells*, 95(10):2703–2725, 2011.

[14] Tarkeshwar Mahto and Vivekananda Mukherjee. Fractional order fuzzy pid controller for wind energy-based hybrid power system using quasi-oppositional harmony search algorithm. *IET Generation, Transmission & Distribution*, 11(13):3299–3309, 2017.

[15] Gary L Johnson. *Wind energy systems*. Citeseer, 1985.

[16] Md E Haque, Michael Negnevitsky, and Kashem M Muttaqi. A novel control strategy for a variable speed wind turbine with a permanent magnet synchronous generator. In *2008 IEEE industry applications society annual meeting*, pages 1–8. IEEE, 2008.

[17] Frederikus Wenehenubun, Andy Saputra, and Hadi Sutanto. An experimental study on the performance of savonius wind turbines related with the number of blades. *Energy procedia*, 68:297–304, 2015.

[18] Nikos Hatziargyriou. *Microgrids: architectures and control*. John Wiley & Sons, 2014.

[19] M Boussetta, S Motahhir, R El Bachtiri, A Allouhi, M Khanfara, and Y Chaibi. Design and embedded implementation of a power management controller for wind-pv-diesel microgrid system. *International Journal of Photoenergy*, 2019, 2019.

[20] Mahdieh Najafzadeh, Roya Ahmadiahangar, Oleksandr Husev, Indrek Roasto, Tanel Jalakas, and Andrei Blinov. Recent contributions, future prospects and limitations of interlinking converter control in hybrid ac/dc microgrids. *IEEE Access*, 9:7960–7984, 2021.

[21] Eneko Unamuno and Jon Andoni Barrena. Hybrid ac/dc microgrids—part ii: Review and classification of control strategies. *Renewable and Sustainable Energy Reviews*, 52:1123–1134, 2015.

[22] Indrek Roasto, Tanel Jalakas, and Argo Rosin. Bidirectional operation of the power electronic interface for nearly-zero energy buildings. In *2018 20th European Conference on Power Electronics and Applications (EPE'18 ECCE Europe)*, pages P–1. IEEE, 2018.

[23] Buddhadeva Sahoo, Sangram Keshari Routray, and Pravat Kumar Rout. Ac, dc, and hybrid control strategies for smart microgrid application: A review. *International Transactions on Electrical Energy Systems*, 31(1):e12683, 2021.

[24] Linus Orokpo Idoko. *Enhanced PV module efficiency to boost hybrid microgrid power and microgrid ancillary services market*. PhD thesis, University of Strathclyde Glasgow, 2018.

[25] Mei Su, Zhangjie Liu, Yao Sun, Hua Han, and Xiaochao Hou. Stability analysis and stabilization methods of dc microgrid with multiple parallel-connected dc–dc converters loaded by cpls. *IEEE Transactions on Smart Grid*, 9(1):132–142, 2016.

[26] Xiong Liu, Peng Wang, and Poh Chiang Loh. A hybrid ac/dc microgrid and its coordination control. *IEEE Transactions on smart grid*, 2(2):278–286, 2011.

[27] Jackson John Justo, Francis Mwasilu, Ju Lee, and Jin-Woo Jung. Ac-microgrids versus dc-microgrids with distributed energy resources: A review. *Renewable and sustainable energy reviews*, 24:387–405, 2013.

[28] Hossein Lotfi and Amin Khodaei. Ac versus dc microgrid planning. *IEEE Transactions on Smart Grid*, 8(1):296–304, 2015.

[29] Farid Katiraei and Mohammad Reza Iravani. Power management strategies for a microgrid with multiple distributed generation units. *IEEE transactions on power systems*, 21(4):1821–1831, 2006.

[30] Peng Wang, Xiong Liu, Chi Jin, Pohchiang Loh, and Fookhoong Choo. A hybrid ac/dc micro-grid architecture, operation and control. In *2011 IEEE Power and Energy Society General Meeting*, pages 1–8. IEEE, 2011.

[31] Navid Eghtedarpour and Ebrahim Farjah. Power control and management in a hybrid ac/dc microgrid. *IEEE transactions on smart grid*, 5(3):1494–1505, 2014.

[32] Hossein Lotfi and Amin Khodaei. Hybrid ac/dc microgrid planning. *Energy*, 118:37–46, 2017.

[33] Anurag Chauhan and RP Saini. A review on integrated renewable energy system based power generation for stand-alone applications: Configurations, storage options, sizing methodologies and control. *Renewable and Sustainable Energy Reviews*, 38:99–120, 2014.

[34] Pervez Hameed Shaikh, Nursyarizal Bin Mohd Nor, Perumal Nallagownden, Irraivan Elamvazuthi, and Taib Ibrahim. Intelligent multi-objective control and management for smart energy efficient buildings. *International Journal of Electrical Power & Energy Systems*, 74:403–409, 2016.

[35] Peigen Tian, Xi Xiao, Kui Wang, and Ruoxing Ding. A hierarchical energy management system based on hierarchical optimization for microgrid community economic operation. *IEEE Transactions on Smart Grid*, 7(5):2230–2241, 2015.

[36] Mohammad Raeispour, Hajar Atrianfar, Hamid Reza Baghaee, and Gevork B Gharehpetian. Robust sliding mode and mixed h_2/h_∞ output feedback primary control of ac microgrids. *IEEE Systems Journal*, 2020.

[37] Lexuan Meng, Eleonora Riva Sanseverino, Adriana Luna, Tomislav Dragicevic, Juan C Vasquez, and Josep M Guerrero. Microgrid supervisory controllers and energy management systems: A literature review. *Renewable and Sustainable Energy Reviews*, 60:1263–1273, 2016.

[38] Ali Bidram and Ali Davoudi. Hierarchical structure of microgrids control system. *IEEE Transactions on Smart Grid*, 3(4):1963–1976, 2012.

[39] XIE Ye, Al Savvarisal, Antonios Tsourdos, Dan Zhang, and GU Jason. Review of hybrid electric powered aircraft, its conceptual design and energy management methodologies. *Chinese Journal of Aeronautics*, 34(4):432–450, 2021.

[40] Yunjie Gu, Yitong Li, Hyeong-Jun Yoo, Thai-Thanh Nguyen, Xin Xiang, Hak-Man Kim, Adria Junyent-Ferre, and Timothy C Green. Transfverter: Imbuing transformer-like properties in an interlink converter for robust control of a hybrid ac–dc microgrid. *IEEE Transactions on Power Electronics*, 34(11):11332–11341, 2019.

[41] Farzam Nejabatkhah and Yun Wei Li. Overview of power management strategies of hybrid ac/dc microgrid. *IEEE Transactions on power electronics*, 30(12):7072–7089, 2014.

[42] Remus Teodorescu, Marco Liserre, and Pedro Rodriguez. *Grid converters for photovoltaic and wind power systems*. John Wiley & Sons, 2011.

[43] John Doyle, Keith Glover, Pramod Khargonekar, and Bruce Francis. State-space solutions to standard h_2 and h_∞ control problems. In *1988 American Control Conference*, pages 1691–1696. IEEE, 1988.

[44] Toufik Amieur, Abdelaziz Younsi, Mohammed Aidoud, Moussa Sedraoui, and Oualid Amieur. Design of robust fractional order PID controller using fractional weights in the mixed sensitivity problem. In *2017 14th International Multi-Conference on Systems, Signals & Devices (SSD)*. IEEE, mar 2017.

[45] T Amieur, M Sedraoui, O Amieur, A Djeddi, and Y Houam. Adaptive fuzzy sliding mode control for uncertain nonlinear siso systems. In *2014 15th International Conference on Sciences and Techniques of Automatic Control and Computer Engineering (STA)*, pages 142–147. IEEE, 2014.

[46] Abdelaziz Younsi, Toufik Amieur, Oualid Amieur, Moussa Sedraoui, and Djamel Taibi. Adaptive fuzzy sliding mode control based on linear matrix inequalities for nonlinear systems. In *2017 14th International Multi-Conference on Systems, Signals & Devices (SSD)*, pages 287–292. IEEE, 2017.

[47] Sami Kahla, Mohcene Bechouat, Toufik Amieur, Moussa Sedraoui, Badreddine Babes, and Noureddine Hamouda. Maximum power extraction framework using robust fractional-order feedback linearization control and gm-cpso for pmsg-based wecs. *Wind Engineering*, 45(4):1040–1054, 2021.

[48] Toufik Amieur, Moussa Sedraoui, and Oualid Amieur. Design of robust fractional-order PID controller for DC motor using the adjustable performance weights in the weighted-mixed sensitivity problem. *IAES International Journal of Robotics and Automation (IJRA)*, 7(2):108, jun 2018.

[49] R Ramaprabha and BL Mathur. A comprehensive review and analysis of solar photovoltaic array configurations under partial shaded conditions. *International Journal of Photoenergy*, 2012, 2012.

[50] Hans S Rauschenbach. *Solar cell array design handbook: the principles and technology of photovoltaic energy conversion*. Springer Science & Business Media, 2012.

[51] Marcelo Gradella Villalva, Jonas Rafael Gazoli, and Ernesto Ruppert Filho. Comprehensive approach to modeling and simulation of photovoltaic arrays. *IEEE Transactions on power electronics*, 24(5):1198–1208, 2009.

[52] BP Solar. Bp msx 120 datasheet. http://www.soltec-solar.com/html/cms/bp/product$_msx_120.pdf$.

[53] Wafa Hayder, Emanuele Ogliari, Alberto Dolara, Aycha Abid, Mouna Ben Hamed, and Lasaad Sbita. Improved pso: a comparative study in mppt algorithm for pv system control under partial shading conditions. *Energies*, 13(8):2035, 2020.

[54] Xiao Li, Yaoyu Li, John E Seem, and Peng Lei. Maximum power point tracking for photovoltaic systems using adaptive extremum seeking control. In *Dynamic Systems and Control Conference*, volume 54754, pages 803–810, 2011.

[55] Trishan Esram and Patrick L Chapman. Comparison of photovoltaic array maximum power point tracking techniques. *IEEE Transactions on energy conversion*, 22(2):439–449, 2007.

[56] Nicola Femia, Giovanni Petrone, Giovanni Spagnuolo, and Massimo Vitelli. Optimization of perturb and observe maximum power point tracking method. *IEEE transactions on power electronics*, 20(4):963–973, 2005.

[57] Eftichios Koutroulis, Kostas Kalaitzakis, and Nicholas C Voulgaris. Development of a microcontroller-based, photovoltaic maximum power point tracking control system. *IEEE Transactions on power electronics*, 16(1):46–54, 2001.

[58] KH Hussein, Itsuya Muta, Tsutomu Hoshino, and Ml Osakada. Maximum photovoltaic power tracking: an algorithm for rapidly changing atmospheric conditions. *IEE Proceedings-Generation, Transmission and Distribution*, 142(1):59–64, 1995.

[59] Dezso Sera, Tamas Kerekes, Remus Teodorescu, and Frede Blaabjerg. Improved mppt method for rapidly changing environmental conditions. In *2006 IEEE International Symposium on Industrial Electronics*, volume 2, pages 1420–1425. IEEE, 2006.

[60] Mohammad N Marwali and Ali Keyhani. Control of distributed generation systems-part i: Voltages and currents control. *IEEE Transactions on power electronics*, 19(6):1541–1550, 2004.

[61] Min Dai, Mohammad Nanda Marwali, Jin-Woo Jung, and Ali Keyhani. A three-phase four-wire inverter control technique for a single distributed generation unit in island mode. *IEEE Transactions on power electronics*, 23(1):322–331, 2008.

[62] Mohammad N Marwali, Min Dai, and Ali Keyhani. Robust stability analysis of voltage and current control for distributed generation systems. *IEEE Transactions on Energy Conversion*, 21(2):516–526, 2006.

[63] Vivek Kumar and Ikbal Ali. Fractional order sliding mode approach for chattering free direct power control of dc/ac converter. *IET Power Electronics*, 12(13):3600–3610, 2019.

[64] Fei Ding, Peng Li, Bibin Huang, Fei Gao, Chengdi Ding, and Chengshan Wang. Modeling and simulation of grid-connected hybrid photovoltaic/battery distributed generation system. In *CICED 2010 Proceedings*, pages 1–10. IEEE, 2010.

[65] Amieur Oualid and Zidani Fatiha. A robust voltage h_∞ controller in DG-connected inverter based on auto-calibration of adjustable fractional weights. *PRZEGLĄD ELEKTROTECHNICZNY*, 1(2):23–29, 02 2022.

[66] Zoubir Chelli, Abdelaziz Lakehal, Tarek Khoualdia, and Yacine Djeghader. Study on shunt active power filter control strategies of three-phase grid-connected photovoltaic systems. *Periodica Polytechnica Electrical Engineering and Computer Science*, 63(3), 2019.

[67] Maniza Armin, Mizanur Rahman, Md Mukidur Rahman, Subrata K Sarker, Sajal K Das, Md Rabiul Islam, Abbas Z Kouzani, and MA Parvez Mahmud. Robust extended h_∞ control strategy using linear matrix inequality approach for islanded microgrid. *IEEE Access*, 8:135883–135896, 2020.

[68] Hamid Reza Baghaee, Mojtaba Mirsalim, Gevork B Gharehpetian, and Heidar Ali Talebi. A generalized descriptor-system robust h_∞ control of autonomous microgrids to improve small and large signal stability considering communication delays and load nonlinearities. *International Journal of Electrical Power & Energy Systems*, 92:63–82, 2017.

[69] Tomas Hornik and Qing-Chang Zhong. A current-control strategy for voltage-source inverters in microgrids based on h_∞ and repetitive control. *IEEE Transactions on Power Electronics*, 26(3):943–952, 2010.

[70] L Sedghi and Ahmad Fakharian. Robust voltage regulation in islanded microgrids: A lmi based mixed h_2/h_∞ control approach. In *2016 24th Mediterranean Conference on Control and Automation (MED)*, pages 431–436. IEEE, 2016.

[71] Hilton Abilio Grundling, Emerson Giovani Carati, and Jose Renes Pinheiro. Analysis and implementation of a modified robust model reference adaptive control with repetitive controller for ups applications. In *IECON'98. Proceedings of the 24th Annual Conference of the IEEE Industrial Electronics Society (Cat. No. 98CH36200)*, volume 1, pages 391–395. IEEE, 1998.

[72] A Sheela, S Vijayachitra, and S Revathi. H-infinity controller for frequency and voltage regulation in grid-connected and islanded microgrid. *IEEJ Transactions on Electrical and Electronic Engineering*, 10(5):503–511, 2015.

[73] TS Lee, KS Tzeng, and MS Chong. Robust controller design for a single-phase ups inverter using μ-synthesis. *IEE Proceedings-Electric Power Applications*, 151(3):334–340, 2004.

[74] Abdelfatah M Mohamed. Modern robust control of a csi-fed induction motor drive system. In *Proceedings of the 1998 American Control Conference. ACC (IEEE Cat. No. 98CH36207)*, volume 6, pages 3803–3808. IEEE, 1998.

[75] Quang Linh Lam, Antoneta Iuliana Bratcu, and Delphine Riu. Robustness analysis of primary frequency h_∞ control in stand-alone microgrids with storage units. *IFAC-PapersOnLine*, 49(27):123–128, 2016.

[76] Jian Zhao and Chao Li Wang. Frequency stability of microgrids based on h_∞ methods. In *2016 35th Chinese Control Conference (CCC)*, pages 10079–10084. IEEE, 2016.

[77] ZM Pe, PK Jain, and PC Sen. Robust controller design for high frequency resonant inverter system with voltage mode control. In *30th Annual Conference of IEEE Industrial Electronics Society, 2004. IECON 2004*, volume 1, pages 41–46. IEEE, 2004.

[78] Hassan Bevrani, Mohammad Ramin Feizi, and Sirwan Ataee. Robust frequency control in an islanded microgrid: h_∞ and μ-synthesis approaches. *IEEE transactions on smart grid*, 7(2):706–717, 2015.

[79] Mohsen Hamzeh, Sepehr Emamian, Houshang Karimi, and Jean Mahseredjian. Robust control of an islanded microgrid under unbalanced and nonlinear load conditions. *IEEE Journal of Emerging and Selected Topics in Power Electronics*, 4(2):512–520, 2015.

[80] Sasan Gholami, Sajeeb Saha, and Mohammad Aldeen. Robust multiobjective control method for power sharing among distributed energy resources in islanded microgrids with unbalanced and nonlinear loads. *International Journal of Electrical Power & Energy Systems*, 94:321–338, 2018.

[81] Malek Ramezani, Shuhui Li, and Saeed Golestan. Analysis and controller design for stand-alone vsis in synchronous reference frame. *IET Power Electronics*, 10(9):1003–1012, 2017.

[82] JW Jung, VQ Leu, DQ Dang, TD Do, F Mwasilu, and HH Choi. Intelligent voltage control strategy for three-phase ups inverters with output lc filter. *International Journal of Electronics*, 102(8):1267–1288, 2015.

[83] T Amieur, M Bechouat, M Sedraoui, S Kahla, and H Guessoum. A new robust tilt-pid controller based upon an automatic selection of adjustable fractional weights for permanent magnet synchronous motor drive control. *Electrical Engineering*, 103(3):1881–1898, 2021.

[84] Toufik Amieur, Moussa Sedraoui, and Oualid Amieur. Design of robust fractional-order pid controller for dc motor using the adjustable performance weights in the weighted-mixed sensitivity problem. *IAES International Journal of Robotics and Automation*, 7(2):108, 2018.

[85] Toufik Amieur. Design of robust fractional-order pid controller for dc motor using the adjustable performance weights. *Journal of Electrical Engineering*, 20(5):8–8, 2020.

[86] Toufik Amieur, Abdelaziz Younsi, Mohammed Aidoud, Moussa Sedraoui, and Oualid Amieur. Design of robust fractional order pid controller using fractional weights in the mixed sensitivity problem. In *2017 14th International Multi-Conference on Systems, Signals & Devices (SSD)*, pages 549–553. IEEE, 2017.

[87] M Sedraoui, T Amieur, R Bachir Bouiadjra, and M Sahnoune. Robustified fractional-order controller based on adjustable fractional weights for a doubly fed induction generator. *Transactions of the Institute of Measurement and Control*, 39(5):660–674, 2017.

[88] Jiankun Hu, Christian Bohn, and HR Wu. Systematic h_∞ weighting function selection and its application to the real-time control of a vertical take-off aircraft. *Control Engineering Practice*, 8(3):241–252, 2000.

[89] Gary Balas, Richard Chiang, Andy Packard, and Michael Safonov. Robust control toolbox™ getting started guide. *The MathWorks, Incorporations. 3 Apple Hill Drive, Natick, MA 01760*, 2098, 2011.

[90] MG Ortega and FR Rubio. Systematic design of weighting matrices for the h_∞ mixed sensitivity problem. *Journal of Process Control*, 14(1):89–98, 2004.

[91] H Oloomi and B Shafai. Weight selection in mixed sensitivity robust control for improving the sinusoidal tracking performance. In *42nd IEEE International Conference on Decision and Control (IEEE Cat. No. 03CH37475)*, volume 1, pages 300–305. IEEE, 2003.

[92] Ning Zhang, Wei Gu, Haojun Yu, and Wei Liu. Application of coordinated sofc and smes robust control for stabilizing tie-line power. *Energies*, 6(4):1902–1917, 2013.

[93] Sigurd Skogestad. *Multivariable feedback control: analysis and design*, volume 2. Citeseer, 2007.

[94] Mohammed Aidoud, Vicente Feliu-Batlle, Abdennour Sebbagh, and Moussa Sedraoui. Small signal model designing and robust decentralized tilt integral derivative tid controller synthesizing for twin rotor mimo system. *International Journal of Dynamics and Control*, pages 1–17, 2022.

[95] Qing-Chang Zhong and Tomas Hornik. *Control of power inverters in renewable energy and smart grid integration*, volume 97. John Wiley & Sons, 2012.

[96] Boualam Benlahbib, Noureddine Bouarroudj, Saad Mekhilef, Dahbi Abdeldjalil, Thameur Abdelkrim, Farid Bouchafaa, et al. Experimental investigation of power management and control of a pv/wind/fuel cell/battery hybrid energy system microgrid. *International Journal of Hydrogen Energy*, 45(53):29110–29122, 2020.

[97] B Baykant Alagoz and Asim Kaygusuz. Dynamic energy pricing by closed-loop fractional-order pi control system and energy balancing in smart grid energy markets. *Transactions of the Institute of Measurement and Control*, 38(5):565–578, 2016.

[98] Milad Moafi, Mousa Marzband, Mehdi Savaghebi, and Josep M Guerrero. Energy management system based on fuzzy fractional order pid controller for transient stability improvement in microgrids with energy storage. *International Transactions on Electrical Energy Systems*, 26(10):2087–2106, 2016.

[99] Mousa Marzband, Ebrahim Yousefnejad, Andreas Sumper, and José Luis Domínguez-García. Real time experimental implementation of optimum energy management system in standalone microgrid by using multi-layer ant colony optimization. *International Journal of Electrical Power & Energy Systems*, 75:265–274, 2016.

[100] Onur Ozdal Mengi and Ismail Hakki Altas. A new energy management technique for pv/wind/grid renewable energy system. *International Journal of Photoenergy*, 2015, 2015.

[101] Zoubir Roumila, Djamila Rekioua, and Toufik Rekioua. Energy management based fuzzy logic controller of hybrid system wind/photovoltaic/diesel with storage battery. *International Journal of Hydrogen Energy*, 42(30):19525–19535, 2017.

[102] Vijay P Singh, Soumya R Mohanty, Nand Kishor, and Prakash K Ray. Robust h-infinity load frequency control in hybrid distributed generation system. *International journal of electrical power & energy systems*, 46:294–305, 2013.

[103] G Mallesham, S Mishra, and AN Jha. Ziegler-nichols based controller parameters tuning for load frequency control in a microgrid. In *2011 International conference on energy, automation and signal*, pages 1–8. IEEE, 2011.

[104] Nerea Ruiz, Iñigo Cobelo, and José Oyarzabal. A direct load control model for virtual power plant management. *IEEE Transactions on Power Systems*, 24(2):959–966, 2009.

[105] André Malheiro, Pedro M Castro, Ricardo M Lima, and Ana Estanqueiro. Integrated sizing and scheduling of wind/pv/diesel/battery isolated systems. *Renewable Energy*, 83:646–657, 2015.

[106] Bruno Belvedere, Michele Bianchi, Alberto Borghetti, Carlo Alberto Nucci, Mario Paolone, and Antonio Peretto. A microcontroller-based power management system for standalone microgrids with hybrid power supply. *IEEE Transactions on Sustainable Energy*, 3(3):422–431, 2012.

[107] Tine L Vandoorn, Brecht Zwaenepoel, Jeroen DM De Kooning, Bart Meersman, and Lieven Vandevelde. Smart microgrids and virtual power plants in a hierarchical control structure. In *2011 2nd IEEE PES International Conference and Exhibition on Innovative Smart Grid Technologies*, pages 1–7. IEEE, 2011.

[108] Ranjay Singh, Ramesh C Bansal, Arvind R Singh, and Raj Naidoo. Multi-objective optimization of hybrid renewable energy system using reformed electric system cascade analysis for islanding and grid connected modes of operation. *IEEE Access*, 6:47332–47354, 2018.

[109] U Boonbumroong, N Pratinthong, S Thepa, C Jivacate, and W Pridasawas. Particle swarm optimization for ac-coupling stand alone hybrid power systems. *Solar Energy*, 85(3):560–569, 2011.

[110] Alireza Askarzadeh and Leandro dos Santos Coelho. A novel framework for optimization of a grid independent hybrid renewable energy system: A case study of iran. *Solar Energy*, 112:383–396, 2015.

[111] Rodolfo Dufo-Lopez, José L Bernal-Agustín, and Javier Contreras. Optimization of control strategies for stand-alone renewable energy systems with hydrogen storage. *Renewable energy*, 32(7):1102–1126, 2007.

[112] Bahman Bahmani-Firouzi and Rasoul Azizipanah-Abarghooee. Optimal sizing of battery energy storage for micro-grid operation management using a new improved bat algorithm. *International Journal of Electrical Power & Energy Systems*, 56:42–54, 2014.

[113] Alireza Askarzadeh. Electrical power generation by an optimised autonomous pv/wind/tidal/battery system. *IET Renewable Power Generation*, 11(1):152–164, 2017.

[114] Sina Makhdoomi and Alireza Askarzadeh. Optimizing operation of a photovoltaic/diesel generator hybrid energy system with pumped hydro storage by a modified crow search algorithm. *Journal of Energy Storage*, 27:101040, 2020.

[115] Sarangthem Sanajaoba and Eugene Fernandez. Maiden application of cuckoo search algorithm for optimal sizing of a remote hybrid renewable energy system. *Renewable energy*, 96:1–10, 2016.

[116] Sudhanshu Ranjan, Dulal Chandra Das, Soumyashree Behera, and Nidul Sinha. Parabolic trough solar–thermal–wind–diesel isolated hybrid power system: active power/frequency control analysis. *IET Renewable Power Generation*, 12(16):1893–1903, 2018.

[117] Attia A El-Fergany and Mohammed A El-Hameed. Efficient frequency controllers for autonomous two-area hybrid microgrid system using social-spider optimiser. *IET Generation, Transmission & Distribution*, 11(3):637–648, 2017.

[118] Partha Pratim Dey, Dulal Chandra Das, Abdul Latif, SM Hussain, and Taha Selim Ustun. Active power management of virtual power plant under penetration of central receiver solar thermal-wind using butterfly optimization technique. *Sustainability*, 12(17):6979, 2020.

[119] Pablo Garcia, Juan P Torreglosa, Luis M Fernandez, and Francisco Jurado. Optimal energy management system for stand-alone wind turbine/photovoltaic/hydrogen/battery hybrid system with supervisory control based on fuzzy logic. *International Journal of Hydrogen Energy*, 38(33):14146–14158, 2013.

[120] Mohammad Jafari, Zahra Malekjamshidi, Jianguo Zhu, and Mohammad-Hassan Khooban. A novel predictive fuzzy logic-based energy management system for grid-connected and off-grid operation of residential smart microgrids. *IEEE Journal of Emerging and Selected Topics in Power Electronics*, 8(2):1391–1404, 2018.

[121] Mustafa E Sahin and Halil İ Okumus. Fuzzy logic controlled buck-boost dc-dc converter for solar energy-battery system. In *2011 International Symposium on Innovations in Intelligent Systems and Applications*, pages 394–397. IEEE, 2011.

[122] Yu-Shan Cheng, Holger Hesse, Nam Truong, Andreas Jossen, and Yi-Hua Liu. Charging strategy for a residential battery storage system using fuzzy logic controller. In *NEIS Conference 2016*, pages 182–189. Springer, 2017.

[123] Yu-Shan Cheng, Yi-Hua Liu, Holger C Hesse, Maik Naumann, Cong Nam Truong, and Andreas Jossen. A pso-optimized fuzzy logic control-based charging method for individual household battery storage systems within a community. *Energies*, 11(2):469, 2018.

[124] V Indragandhi, R Logesh, V Subramaniyaswamy, V Vijayakumar, Patrick Siarry, and Lorna Uden. Multi-objective optimization and energy management in renewable based ac/dc microgrid. *Computers & Electrical Engineering*, 70:179–198, 2018.

[125] Akhtar Hussain, Van-Hai Bui, and Hak-Man Kim. Fuzzy logic-based operation of battery energy storage systems (besss) for enhancing the resiliency of hybrid microgrids. *Energies*, 10(3):271, 2017.

[126] Tohid Khalili, Sayyad Nojavan, and Kazem Zare. Optimal performance of microgrid in the presence of demand response exchange: A stochastic multi-objective model. *Computers & Electrical Engineering*, 74:429–450, 2019.

[127] Washima Tasnin and Lalit Chandra Saikia. Performance comparison of several energy storage devices in deregulated agc of a multi-area system incorporating geothermal power plant. *IET Renewable Power Generation*, 12(7):761–772, 2018.

[128] Amir Hajiloo and Wen-Fang Xie. Multi-objective optimal fuzzy fractional-order pid controller design. *Journal of Advanced Computational Intelligence and Intelligent Informatics*, 18(3):262–270, 2014.

[129] Arindita Saha and Lalit Chandra Saikia. Utilisation of ultra-capacitor in load frequency control under restructured stpp-thermal power systems using woa optimised pidn-fopd controller. *IET Generation, Transmission & Distribution*, 11(13):3318–3331, 2017.

[130] MR Sathya and M Mohamed Thameem Ansari. Design of biogeography optimization based dual mode gain scheduling of fractional order pi load frequency controllers for multi source interconnected power systems. *International Journal of Electrical Power & Energy Systems*, 83:364–381, 2016.

[131] Billel Meghni, Djalel Dib, Ahmad Taher Azar, Sihem Ghoudelbourk, and A Saadoun. Robust adaptive supervisory fractional order controller for optimal energy management in wind turbine with battery storage. In *Fractional Order Control and Synchronization of Chaotic Systems*, pages 165–202. Springer, 2017.

[132] Bo Yang, Tao Yu, Hongchun Shu, Yiming Han, Pulin Cao, and Lin Jiang. Adaptive fractional-order pid control of pmsg-based wind energy conversion system for mppt using linear observers. *International Transactions on Electrical Energy Systems*, 29(1):e2697, 2019.

[133] Abdelmoumène Delassi, Salem Arif, and Lakhdar Mokrani. Load frequency control problem in interconnected power systems using robust fractional piλd controller. *Ain Shams Engineering Journal*, 9(1):77–88, 2018.

[134] Asim Kaygusuz. Closed loop elastic demand control by dynamic energy pricing in smart grids. *Energy*, 176:596–603, 2019.

[135] Oussama Maroufi, Abdelghani Choucha, and Lakhdar Chaib. Hybrid fractional fuzzy pid design for mppt-pitch control of wind turbine-based bat algorithm. *Electrical Engineering*, 102:2149–2160, 2020.

[136] Yogendra Arya and Narendra Kumar. Bfoa-scaled fractional order fuzzy pid controller applied to agc of multi-area multi-source electric power generating systems. *Swarm and Evolutionary Computation*, 32:202–218, 2017.

[137] Badreddine Babes, Fahad Albalawi, Noureddine Hamouda, Sami Kahla, and Sherif SM Ghoneim. Fractional-fuzzy pid control approach of photovoltaic-wire feeder system (pv-wfs): Simulation and hil-based experimental investigation. *IEEE Access*, 2021.

[138] Indranil Pan and Saptarshi Das. Fractional order fuzzy control of hybrid power system with renewable generation using chaotic pso. *ISA transactions*, 62:19–29, 2016.

[139] Yogendra Arya. A new optimized fuzzy fopi-fopd controller for automatic generation control of electric power systems. *Journal of the Franklin Institute*, 356(11):5611–5629, 2019.

[140] Yogendra Arya. Agc performance enrichment of multi-source hydrothermal gas power systems using new optimized fofpid controller and redox flow batteries. *Energy*, 127:704–715, 2017.

[141] Meysam Gheisarnejad and Mohammad Hassan Khooban. Design an optimal fuzzy fractional proportional integral derivative controller with derivative filter for load frequency control in power systems. *Transactions of the Institute of Measurement and Control*, 41(9):2563–2581, 2019.

[142] Jayanti Singh, Vijander Singh, Asha Rani, Jyoti Yadav, and Vijay Mohan. Performance analysis of fractional order fuzzy pid controller for hybrid power system using woa. In *2018 2nd International Conference on Trends in Electronics and Informatics (ICOEI)*, pages 976–983. IEEE, 2018.

[143] Hany M Hasanien. Whale optimisation algorithm for automatic generation control of interconnected modern power systems including renewable energy sources. *IET Generation, Transmission & Distribution*, 12(3):607–614, 2018.

[144] Abdul Latif, SM Suhail Hussain, Dulal Chandra Das, Taha Selim Ustun, and Atif Iqbal. A review on fractional order (fo) controllers' optimization for load frequency stabilization in power networks. *Energy Reports*, 7:4009–4021, 2021.

[145] Erik Cuevas and Miguel Cienfuegos. A new algorithm inspired in the behavior of the social-spider for constrained optimization. *Expert Systems with Applications*, 41(2):412–425, 2014.

[146] Erik Cuevas, Miguel Cienfuegos, Daniel Zaldívar, and Marco Pérez-Cisneros. A swarm optimization algorithm inspired in the behavior of the social-spider. *Expert Systems with Applications*, 40(16):6374–6384, 2013.

[147] Indranil Pan and Saptarshi Das. *Intelligent fractional order systems and control: an introduction*, volume 438. Springer, 2012.

[148] Hassan Bevrani, Farshid Habibi, Pouya Babahajyani, Masayuki Watanabe, and Yasunori Mitani. Intelligent frequency control in an ac microgrid: Online pso-based fuzzy tuning approach. *IEEE transactions on smart grid*, 3(4):1935–1944, 2012.

[149] Chuen-Chien Lee. Fuzzy logic in control systems: fuzzy logic controller. i. *IEEE Transactions on systems, man, and cybernetics*, 20(2):404–418, 1990.

[150] Ebrahim H Mamdani and Sedrak Assilian. An experiment in linguistic synthesis with a fuzzy logic controller. *International journal of man-machine studies*, 7(1):1–13, 1975.

[151] Tomohiro Takagi and Michio Sugeno. Fuzzy identification of systems and its applications to modeling and control. *IEEE transactions on systems, man, and cybernetics*, (1):116–132, 1985.

[152] JQ James and Victor OK Li. A social spider algorithm for global optimization. *Applied soft computing*, 30:614–627, 2015.

[153] Manuel D Ortigueira and JA Tenreiro Machado. What is a fractional derivative? *Journal of computational Physics*, 293:4–13, 2015.

[154] Shantanu Das. *Functional fractional calculus*. Springer Science & Business Media, 2011.

[155] Rudolf Scherer, Shyam L Kalla, Yifa Tang, and Jianfei Huang. The grünwald–letnikov method for fractional differential equations. *Computers & Mathematics with Applications*, 62(3):902–917, 2011.

Summary

Summary

A Contribution to Energy Saving in Electrical Control Systems

In many cases, geographical and economic factors prevent energy companies from electrifying remote areas. But these remote areas are developing standalone microgeneration systems based on renewable energy sources, which are called microgrids.The developed standalone microgrid suffers from the intermittent nature of renewable energy sources. It therefore seems essential to adopt energy-saving controls that allow effective energy management. This thesis presents whole system modelling and control of hybrid microgrids, including photovoltaic generator and wind turbine system sources as well as battery energy storage systems. The main aim of this thesis was to save energy by focusing generally on the energy management system, with particular attention given to power quality and management, assuming that there are robust available control techniques for the specified energy management features. The work was then discussed and evaluated using the MATLAB/SIMULINK program. The simulation results illustrate the effectiveness of each suggested control on the energy-saving rate.

Keywords:

Energy-saving, microgrid power system, hybrid renewable energy system, power converter, PV generator, wind turbine generator.

Résumé

Contribution à L'économie de L'énergie dans les Systèmes de Commande Electrique

Dans des nombreuses régions éloignées, des obstacles géographiques et économiques empêchent les sociétés énergétiques d'électrifier. Mais ces régions éloignées développent des systèmes de micro-génération autonomes basés sur des sources d'énergie renouvelables, appelés micro-réseaux. Le micro-réseau autonome développé souffre du caractère intermittent des sources d'énergie renouvelables. Il apparaît donc indispensable d'adopter une politique d'optimisation énergétique permettant une maîtrise efficace de l'énergie. Cette thèse présente la modélisation et la commande de systèmes complets de micro−réseaux hybrides, y compris les sources de générateurs photovoltaïques et de systèmes d'éoliennes ainsi que les systèmes de stockage d'énergie par batterie. L'objectif principal de cette thèse était d'économiser de l'énergie en se concentrant généralement sur le système de gestion de l'énergie, avec une attention particulière accordée à la qualité et à la gestion de puissance, en supposant qu'il existe des techniques de commande robustes disponibles pour les fonctionnalités de gestion de l'énergie spécifiées. Le travail a ensuite été discuté et évalué à l'aide du programme MATLAB/SIMULINK. Les résultats de la simulation illustrent l'efficacité de chaque commande proposée sur le taux d'économie d'énergie.

Mots clés:

Economie d'énergie, système micro-réseau électrique, système d'énergie renouvelable hybride, convertisseur de puissance, générateur PV, éolienne.

ملخص الأطروحـــة

مساهمة انظمة التحكم الكهربائي في اقتصاد الطاقة

في كثير من الحالات تمنع العوامل الجغرافية والاقتصادية شركات الطاقة من كهربة المناطق النائية مما أدى بهذه المناطق للعمل على تطوير أنظمة إنتاج للطاقة دقيقة قائمة بذاتها تعتمد على مصادر الطاقة المتجددة والتي تسمى الشبكات الصغيرة. تعاني الشبكة الصغيرة المستقلة المطورة من الطبيعة المتقطعة لمصادر الطاقة المتجددة لذلك يبدو من الضروري إعتماد انظمة تحكم موفرة تسمح بإدارة فعالة للطاقة. تقدم هذه الأطروحة نمذجة النظام بالكامل والتحكم في الشبكات الصغيرة الهجينة، بما في ذلك المولدات الكهروضوئية ومصادر نظام توربينات الرياح وكذلك أنظمة تخزين طاقة البطاريات. كان الهدف الرئيسي من هذه الأطروحة هو توفير الطاقة من خلال التركيز بشكل عام على نظام إدارة الطاقة مع إيلاء اهتمام خاص لجودة الطاقة وإدارتها، بافتراض وجود تقنيات تحكم قوية متاحة لخصائص إدارة الطاقة المحددة. تمت مناقشة العمل وتقييمه باستخدام برنامج ماتلاب حيث توضح نتائج المحاكاة فعالية كل عنصر تحكم مقترح على معدل توفير الطاقة.

الكلمات المفتاحية:

اقتصاد الطاقة، نظام الشبكات الصغيرة، نظام الطاقةالمتجددة الهجين، محول للطاقة، مولد الضوئية، مولد توربينات الرياح.